Investigating the Formation of Metal-Superoxides: Iron and Nickel Complexes Based on a 2,6-Pyridinedicarboxamide Ligand System

A report submitted to the School of Chemistry for completion of a master's degree

by

Daniel Nelis

Under the supervision of Prof. A. R. McDonald

2020 Trinity College Dublin

I declare that this report details entirely my own work. Due acknowledgements and references are given to the work of others where appropriate.

…………………………………………

Daniel Nelis

Table of Contents

Acknowledgements

I would like to extend my sincere gratitude to Prof. Aidan McDonald who allowed me to work in his lab as an undergraduate and who provided me the opportunity of pursuing my postgraduate studies upon completion. I would of course like to extend a huge thank you to every present and past member of the BIC group, all of whom have helped me through my postgraduate experiences in their various ways; Andy, Paolo, Ciara, Adriana, Peppe, Marta, Philip, Lorna, Ankita, Bertrand, Prasenjit, Duenpen and Robert. Special thanks also to Andy for his advice when writing my successful grant application as well as to Adriana for her support and most of all patience in my two years within the group. Thank you to Peppe for our great trips to California while learning and carrying out XAS experiments as well as his help in dealing with the data and thank you to Marta for EPR and Robert for carrying out X-ray diffraction on a number of my samples (as well as for correcting this thesis!).

I would like to express my gratitude to Erik Farquhar for his time and patience in detailing the theory and practical learnings of XAS, while Dr. Gary Hessman and Dr. Martin Feeney have been very helpful for Mass spectrometry analysis in Trinity College. Also, a thank you to Dr. John O'Brien for his help with NMR, Dr. Brendan Twamley for his assistance with X-ray diffraction as well as all other members of the Trinity technical staff.

I want to thank Philip, Daniel (the Italian one), Rory and Dan (the Irish one) for the fun times we all had living together, Oisin for our countless late-night talks, the entire Rozas group as well as Simon for their friendship, support and guidance in organic chemistry. Greg and Michael, I want to thank for their "encouragement". Finally, I want to thank all my family and friends for their support and most of all to my girlfriend Nikolina who has listened to me far too often as I have written this thesis.

Summary

Metal-superoxide intermediates have been proposed to be key active intermediates in the catalytic cycles of a wealth of oxygen-activating enzymes in biology. Synthetically, many examples of such intermediates have been spectroscopically characterised of which Fe and Cu containing superoxide complexes have been most studied. However, there exists only a small number of reported Ni-superoxide complexes. This work details the synthesis of two Fe^{II} complexes based on the N,N-bis(2,6-diisopropylphenyl)-2,6-pyridinedicarboxamide ligand framework of which one of these complexes, with an $Fe_2(OH)_2$ core, has been structurally characterised. The structure of this complex showed it to be a dinuclear complex wherein the ligand was bound to the metal via its oxygen atoms, rather through the more conventional amidic nitrogen atoms. The reactivity of a previously reported nickel complex, of the same ligand system, with potassium superoxide has also been investigated and lead to the formation of two Ni^{II} complexes, a Ni^{II}-hydroxide complex, as well as a Ni^{II} complex wherein the coordinated ligand has undergone insertion of an oxygen atom into one of its C-H bonds. The latter has been proposed to form through a homolytic electrophilic hydrogen atom abstraction reaction of a Ni^{II}-superoxide intermediate followed by rebound of a hydroxyl radical to form the hydroxylated ligand. Following post-reaction acidified workup, the position of hydroxylation was determined to be at the methine iPr position. This reactivity has been proposed to follow a similar route as the initial steps of the catalytic cycle of the enzyme Isopenicillin N Synthase, a non-heme iron enzyme used in the synthesis of penicillin.

The isolation of metal-oxygen adducts both in biology and in synthetic systems has most often required the use of cryogenic temperatures. Many of these species decay within seconds or minutes of their formation. Thus, X-ray Absorption Spectroscopy is a spectroscopic technique which has been used to give electronic and structural information of frozen solutions of these unstable intermediates. This thesis concludes with the study of three such intermediates by X-ray absorption near-edge spectroscopy and extended X-ray absorption fine structure analysis. This allowed the oxidation state of each metal site to be identified as well as gave insights into the electronic symmetry surrounding each metal site and the metal-ligand bond distances.

Abbreviations

18-C-6	18-crown-6-ether
6-Me$_3$-TPA	tris(6-methyl-2-pyridylmethyl)-amine)
ACV	δ-(L-α-aminoadipoyl)-L-cysteinyl-D-valine
Asp	aspartic acid
BA	N-benzyl-6-((bis(pyridin-2- ylmethyl)amino)methyl)pyridin-2-amine
BDDP	2,6-bis (((*S*)-2- (diphenylhydroxymethyl)-1-pyrrolidinyl) methyl)pyridine
BDE	bond dissociation energy
Bi^{iPr2}	diisopropylphenyl biuret
CAS	clavaminic acid synthase
CCA	cyclohexanecarboxaldehyde
ClO$_4$	perchlorate
CV	cyclic voltammetry
DBM	dopamine beta-monooxygenase
DCM	dichloromethane
DFT	density functional theory
DHA	dihydroanthracene
^{DMA}N$_3$S	2-((((4-(dimethylamino)pyridin-2-yl)methyl)(2-((2 methylbenzyl)thio)ethyl)amino)methyl)-N,N-dimethylpyridin-4-amine
DMSO	dimethyl sulfoxide
DTBP	2,6-di-tert-butylphenol
DTQ	di-tert-butylquinone
E. coli	escherichia coli
EPR	electron paramagnetic resonance
ESI-MS	electrospray ionisation mass spectrometry
EtA	acetaldehyde
EXAFS	X-ray absorption fine structure
F$_5$TMPA	6-((bis(pyridin-2-ylmethyl)amino)methyl)-N-((perfluorophenyl)methyl)pyridin-2-amine

FTIR	fourier transform infrared
Gln	glutamine
HAT	hydrogen atom transfer
His	histidine
IPN	isopenicillin
IPNS	isopenicillin N synthase
IR	infrared
keV	kilo electron volts
KIE	kinetic isotope effect
KO_2	potassium superoxide
LMCT	ligand-to-metal charger-transfer
MeOH	methanol
Me-THF	2-methyl-THF
MP	2-methoxyphenol
MPPA	bis(pyrid-2-ylmethyl){[6-(pivalamido)pyrid-2-yl]methyl}amine
nacnac	β-diketiminato
NCMe	acetonitrile
Ni SOD	nickel superoxide dismutase
NMe_2-TMPA	tris(4-dimethylaminopyrid-2-ylmethyl)amine
OAT	oxygen atom transfer
PHM	peptidyl-glycine alpha-amidating monooxygenase
$PhTt^{Ad}$	phenyltris((1-adamantylthio)methyl)borate
pmac	dioxopentaazamacrocycle
pMMO	particulate methane monooxygenase
PPA	2-phenylpropionaldehyde
PPh_3	triphenylphosphine
PrA	proponal
RDS	rate determining step
ROS	reactive oxygen species
rR	resonance raman

SCE	saturated calomel electrode
$SOCl_2$	thionyl chloride
SOD	superoxide dismutase
SQUID	superconducting quantum interference device
TAML	tetraamido macrocyclic ligand
Tau D	taurine dioxygenase
tet-b	5,7,7,12,14,14-hexamethyl-1,4,8,11-tetraazacyclotetradecane
TFE	trifluoroethanol
THF	tetrahydrofuran
TLC	thin layer chromatograph
TMA	trimethylacetaldehye
TMC	1,4,8,11-tetramethyl-1,4,8,11-tetraazacyclotetradecane
TMG_3-tren	1,1,1-tris{2-[N-(1,1,3,3-tetramethylguanidino)]ethyl}amine))
TPA	tris(pyridyl)amine
Tp^{iPr2}	hydrotris(3-tert-butyl-5-isopropylpyrazol-l-yl)borate
TTBP	2,4,6-tri-tert-butylphenol
XAS	X-ray absorption spectroscopy
αKG	α-ketoglutaric acid

Figure List

Table List

Scheme list

1. Introduction

1.1 Oxygen Activating Metalloproteins and Superoxide

Throughout the past number of decades, synthetic chemists have looked to biological systems for inspiration in order to design and synthesise a variety of powerful oxidants. This endeavour has been made possible due to the wealth of spectroscopic and structural knowledge which has become available in recent decades regarding the active sites of oxygen-activating metalloproteins. Metalloproteins are proteins which incorporate a metal centre within their structures, most commonly iron and copper, two of the most abundant transition metals found in the earth's crust.[1] However, metals such as manganese, nickel, cobalt and zinc are also known. These oxygen activating metalloproteins are involved in a wealth of biological processes including biomolecule synthesis, oxygen transportation and the regulation and breakdown of biological toxins and cell inhibitors.[2]

The reaction of an oxygen-activating metalloprotein in its ground state (Scheme 1 (a)) with dioxygen in most cases leads to the formation of a metal-superoxide complex, wherein the metal has transferred one electron to the oxygen moiety (Scheme 1 (b)). Superoxide ($O_2^{\bullet -}$) is the one-electron reduced form of dioxygen and is a monoanionic radical.[3,4] This metal-superoxide complex can effect oxidation reactions, or it can be further reduced by one-electron by a cofactor to yield a metal-hydroperoxide species (Scheme 1 (c)). Subsequent reaction of this hydroperoxide moiety and/or further electron reduction with concomitant O-O bond scission can yield a high valent metal-oxo complex (Scheme 1 (d)), the strongest biological oxidants known, which are capable of breaking very inert C-H bonds of various biomolecules.[2,5–8] Although not isolated in all metalloproteins, the metal-superoxide state is necessarily formed in any one-electron redox reaction involving a metal and oxygen. Thus, the chemistry of these superoxide species is integral to the ability of the metalloenzymes to carry out their function.

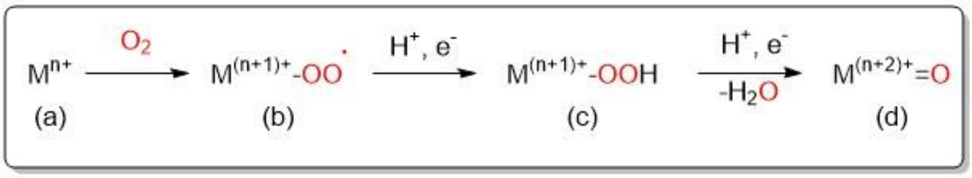

$$\underset{(a)}{M^{n+}} \xrightarrow{O_2} \underset{(b)}{M^{(n+1)+}\text{-}OO^{\bullet}} \xrightarrow{H^+,\ e^-} \underset{(c)}{M^{(n+1)+}\text{-}OOH} \xrightarrow[-H_2O]{H^+,\ e^-} \underset{(d)}{M^{(n+2)+}{=}O}$$

Scheme 1. Typical reaction profile for dioxygen activating metalloproteins

1.2 Reactivity of Biological Metal Superoxide Intermediates

Metal-superoxide intermediates formed in the reduction of oxygen by a metal active site react primarily in one of two ways; (i) as electrophilic oxidants in the cleavage of C-H or O-H bonds, or in oxygen atom transfer (OAT) reactions or (ii) as nucleophilic oxidants in the attack of electrophilic carbonyl groups.[2,5,6,9] In the former, the reaction cycle follows a radical mechanism which forms a carbon or oxygen based radical. This can then undergo a radical rebound reaction with the formed hydroperoxide (Figure 1(c)) or can undergo intermolecular or intramolecular radical reactions with another substrate or itself to form the final product. In the latter, a more conventional 2-electron nucleophilic attack onto the electron deficient carbonyl carbon atom occurs, followed by the loss of a leaving group.

In non-heme Fe^{III}-superoxide systems, such as that proposed to be present in the catalytic cycle of IPNS, a C-H bond is cleaved in an electrophilic oxidation reaction.[2,6,10] This C-H bond is positioned next to a heteroatom which has been postulated to lower the bond dissociation energy (BDE) of the C-H bond sufficiently so as to allow it to be cleaved by the Fe^{III}-superoxide intermediate (discussed in section 1.2.1 below). This is a unique feature of non-heme Fe^{III}-superoxide based systems. Dopamine beta-monooxygenase (DBM) involves cleavage of a single C-H bond by a proposed Cu^{II}-superoxide. DBM does not require the C-H bond which is to be cleaved to be positioned next to a heteroatom, suggesting that the oxidising equivalent formed in this case is stronger than that for non-heme iron systems, as the BDE of the C-H bond is much higher.[11,12] The α-ketoglutarate dependent oxygenases are a diverse family of enzymes which have been proposed to form Fe^{III}-superoxide intermediates in their catalytic cycles which undergo nucleophilic attack on the carbonyl group of a bound α-keto acid, leading to decarboxylation and the formation of a high valent Fe^{IV}=O intermediate.[2] In order to provide substance for the synthesis and reactivity of synthetic metal-superoxide complexes, the catalytic cycles of IPNS, DBM and Taurine dioxygenase (TauD), an α-ketoglutarate dependent oxygenase, will be discussed below and the activity of the proposed metal-superoxide intermediates highlighted. In the previous decades, study of metalloenzymes such as these, has allowed the elucidation of the oxidative potential of metal-superoxide intermediates to be better understood, providing inspiration to synthetic chemists aiming to replicate these biological mechanisms.

1.2.1 Isopenicillin N Synthase

IPNS is a nonheme microbial iron enzyme found in *Cephalosporium*, *Penicillium* and some *Streptomyces* strains that catalyses the formation of isopenicillin N (IPN) from δ-(L-α-aminoadipoyl)-L-cysteinyl-D-valine (ACV).[2,6,10] Baldwin and co-workers showed by kinetic and structural studies that the catalytic cycle of IPNS involved the 4-electron oxidation of ACV using one equivalent of O_2, yielding IPN and two equivalents of H_2O.[10] During the course of the catalysis, 2 C-H bonds, 1 S-H bond and 1 N-H bond are cleaved by a variety of intermediates in the course of the formation of, first the 4-membered β-lactam ring, followed by a C-S bond yielding the 5-membered thiazolidine ring (Fig. 1).[10]

The first X-ray crystallographically characterised structure of IPNS in the absence of the ACV substrate was done with a Mn^{II} substituted analogue from *Aspergillus nidulans*.[13] The structure showed an octahedral metal active site with 2 histidine (His), 1 aspartic acid (Asp) and 1 glutamine (Gln) side chain coordinated, along with 2 H_2O molecules coordinated in a cis position (Fig. 1 (a)). The crystal structure of the Fe^{II}-IPNS-ACV complex showed a 5-coordinate iron core wherein the glutamine side chain was replaced with the ACV substrate along with the loss of one H_2O moiety (Fig. 1 (b)).[14] Binding of the ACV substrate occurred through its deprotonated thiolate sulphur atom, which had been previously assigned by X-ray absorption fine structure (EXAFS) analysis.[15] It has been proposed that the binding of the ACV substrate shifts the redox couple of the Fe^{II}/Fe^{III} to a more negative value allowing O_2 binding at this point only.[2] No structure of the formed oxygen adduct has been characterised to date, however, structural analysis of the Fe^{II}-IPNS-ACV-NO analogue has been carried out, the assumption being that NO acted as a structural surrogate for O_2.[16] The distal oxygen of the NO moiety was observed to be equidistant between the valine N-H group and the cysteinyl β-carbon, suggesting that the initial C-H cleavage reaction occurred in this region.[16]

Density functional theory (DFT) studies have postulated that the β-cysteine C-H bond is the first to be cleaved and that the active oxidant is an Fe^{III}-superoxide complex (Fig. 1 (c)).[17] Cleavage of the β-cysteine C-H bond yields an Fe^{III}-hydroperoxide species (Fig. 1 (d) and (e)) which undergoes O-O bond scission by obtaining an electron and proton from ACV during the formation of the β-lactam ring. This forms an Fe^{IV}=O complex (Fig. 1 (f)) which then can abstract hydrogen from the valine C-H bond (Fig. 1 (g)), effecting the formation of the thiazolidine ring of IPN (Fig. 1 (h)).[17]

The first spectroscopic evidence for the Fe^{III}-superoxide intermediate was obtained in 2016 when stopped-flow absorption spectroscopy and rapid freeze-quench Mössbauer studies were carried out on a Fe^{II}-IPNS-A[d_2-C]V (deuterated β-cysteine) complex and its reaction with O_2 at millisecond timescales.[18] Kinetic isotope effect studies, the ratio of the rate of the reaction with the native substrate and the rate of the reaction with the deuterated substrate analogue, showed the effect of substituting the ACV substrate with the deuterated analogue led to a reduction in the reaction rate by 95%. This implicated the cleavage of the deuterated β-cysteine residue of ACV as the rate determining step (RDS) of the reaction mechanism. The retarding of the reaction using the deuterated analogue allowed the Fe^{III}-superoxide intermediate to accumulate sufficiently as to be measured by Mössbauer spectroscopy prior to its reaction with bound ACV. The species had Mössbauer parameters of $\delta = 0.53$ mm/s, $\Delta E_Q = 11.02$ mm/s and $\Gamma = 0.29$ mm/s, which were similar to other previously characterised high spin Fe^{III}-superoxide species.[18]

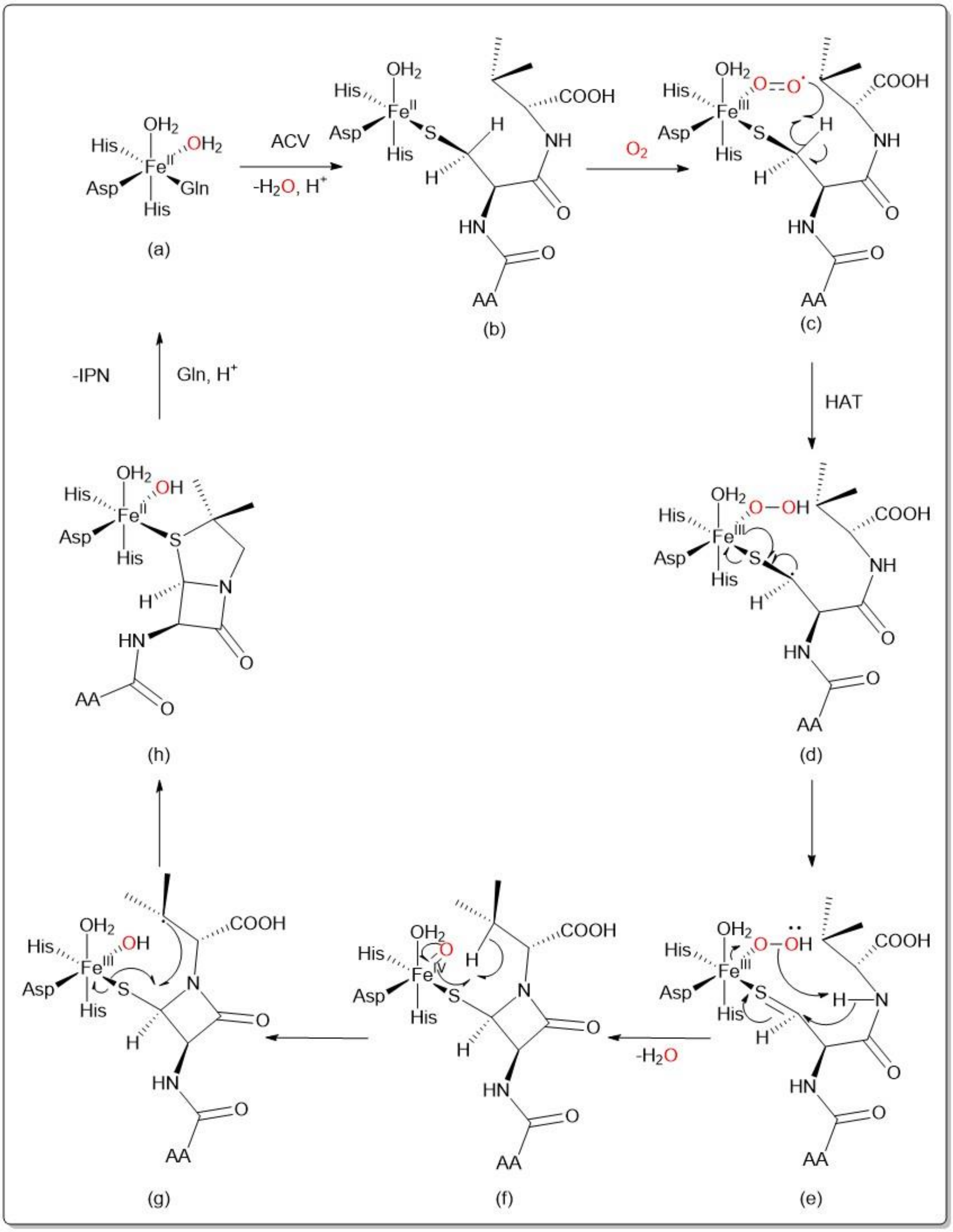

Figure 1. Proposed catalytic cycle of IPNS[2,6]

Thus, IPNS had been shown to directly use a Fe^{III}-superoxide moiety to effect C-H bond cleavage in ACV. This was implicated through the crystal structure of the Fe^{II}-IPNS-ACV-NO species, a structural mimic of an Fe^{III}-superoxide adduct, which showed the distal oxygen to be positioned next to the cleaved C-H bond of ACV. The KIE of ~20 when the deuterated analogue was used suggested that this was the RDS of the reaction and the retardation of the reaction allowed a sample of the proposed Fe^{III}-superoxide to be examined by Mössbauer spectroscopy which characterised it as a high spin Fe^{III} species. However, no structural information was obtained of this intermediate and the properties which defined its reactivity as an electrophilic oxidant are still not well understood.

1.2.2 The Uncoupled Dicopper Centres

Peptidyl-glycine alpha-amidating monooxygenase (PHM) and DBM are metalloproteins found exclusively in higher eukaryotes which oxidise C-terminal glycine-extended peptides to their α-hydroxylated products and dopamine to norepinephrine respectively.[11,19] Although being specific to markedly different substrates, the two enzymes have been historically treated as a pair due to the striking similarities in both their structures and enzymatic cycles. Their active sites contain 2 copper atoms, designated Cu_M (where substrate hydroxylation occurs) and Cu_H (which provides an electron to Cu_M) which are separated by approximately 11 Å.[20]

The resting state of the enzyme is present in a Cu_2^{I} state (Fig. 2 (a)), which is formed by the reduction of the oxidised Cu_2^{II} state (Fig. 2 (e)) by ascorbate. Low temperature electron paramagnetic resonance (EPR) studies have shown that in the oxidised state these copper atoms have uncoupled spin (each with $S = ½$) and are present as Cu^{II} ions.[19] Kinetic studies for the reaction of PHM with N-benzoylglycine as a substrate in the presence of oxygen proceeded with a H/D KIE of 10.6 which was suggestive of a hydrogen atom transfer (HAT) mechanism. This involves a radical reaction wherein the C-H bond is cleaved by the Cu^{II}-superoxide moiety, generating a Cu^{II}-hydroperoxide and organic radical (Fig. 2 (c)).[21] The overall effect is the transfer of a H atom ($H^{\bullet}$) to the Cu^{II}-superoxide. Control reactions where a surrogate substrate has been used (C-H bond has been replaced by stronger C-F bond) have shown that the oxidation of the Cu^{I}_2 centres does not proceed.[19] This suggested that the oxidation of the copper centres was intrinsically linked to binding of the substrate. The increased electrophilicity at the C-F bond was proposed to inhibit substrate binding.

Evidence for the HAT reaction occurring prior to O-O bond cleavage with ^{18}O heavy isotope labelling studies removed the feasibility of a Cu^{II}-hydroperoxide active oxidant.[21] Theoretical models instead proposed that the reactive intermediate which effected the oxidation of the substrate was a mononuclear Cu^{II}-superoxide species (Fig. 2 (b)).[22] Solomon and co-workers have modelled this intermediate as an end-on Cu^{II}-superoxide with an electronic ground state having a very low lying, unoccupied π^* orbital with high oxygen character (49%) on the distal oxygen, lowering the barrier to HAT.[23]

Following HAT, a Cu^{II}-hydroperoxide and substrate radical (Fig. 2 (c)) form which react to form the hydroxylated product and a Cu^{II}-$O^{\bullet}$ intermediate (Fig. 2 (d)). The large reduction potential of this species causes the long-range electron transfer from Cu^{I} to the Cu^{II}-$O^{\bullet}$ site (Fig. 2 (e)), it acts as the driving force for the electrochemical transfer of an electron between the uncoupled, 11 Å-separated, Cu ions.[22] Importantly, uncoupling of the two Cu ions ensures that, upon binding of O_2, the 2-electron reduction to peroxide does not occur, which would inhibit the electrophilic oxidation of the substrate C-H bond, as peroxides are known nucleophilic oxidants, in contrast to the electrophilic nature of the superoxide moieties.[24,25]

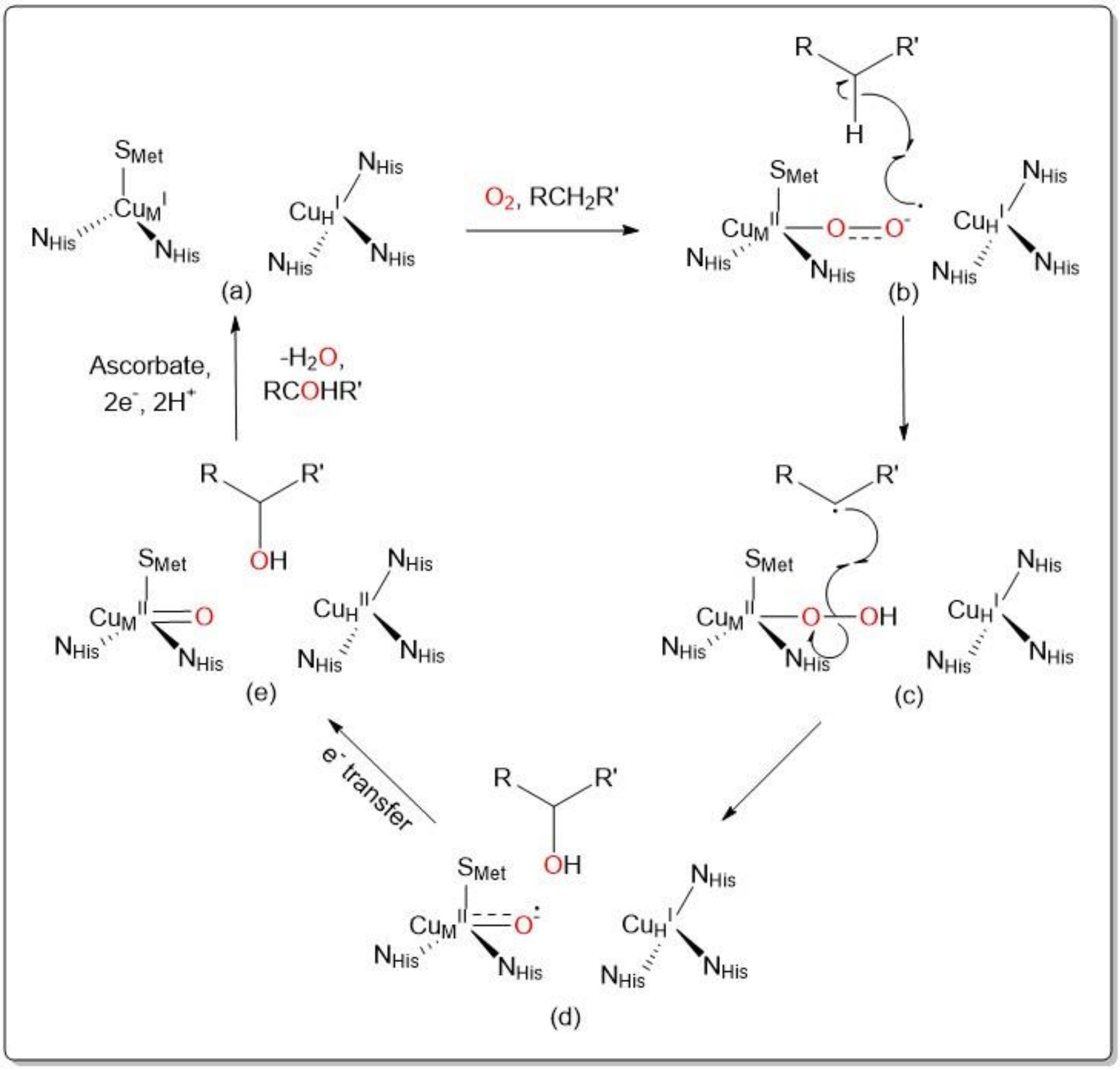

Figure 2. Proposed catalytic cycle of DBM and PHM[19,20]

Overall, the di-copper sites of DBM and PHM have been proposed to react with oxygen to yield a Cu^{II}-superoxide intermediates which then effects substrate oxidation via abstraction of a proton, followed by hydroxyl rebound. This is evidenced by the effect of deuterium substitution which reduces the rate of oxidation by an order of magnitude and which is supported by theoretical studies which proposed the reactive intermediate to be an end-on bound Cu^{II}-superoxide. However, as for the case of IPNS discussed previously, the properties which define the reactivity of the superoxide intermediate to act as an electrophilic oxidant are not well understood. The oxidative reactivity of IPNS, PHM and DBM are in direct contrast to those of the α-ketoglutarate dependent dioxygenases discussed below. However, bioinorganic chemists have struggled to detail a clear answer to these differences.

1.2.3 α-Ketoglutarate Dependent Oxygenases

Metal superoxide intermediates capable of nucleophilic oxidation reactions have also been postulated in a wide variety of enzymes, the best studied of which are the α-ketoglutarate dependent oxygenases.[2,26,27] This class of enzymes require an α-keto acid, such as α-ketoglutaric acid (αKG) as a co-substrate which is postulated to be attacked by a superoxide intermediate, effecting the formation of a high-valent $Fe^{IV}=O$ species, the oxidant required to cleave C-H bonds in the main substrate of the enzyme.[2,26,27] TauD, a metalloprotein found in microbes such as *Escherichia coli* (*E.coli*) and which catalyses the hydroxylation of taurine(2-aminoethanesulfonic acid), is the most well studied of this class of enzymes, however, data accumulated from the entire class of enzymes has been used to propose a mechanism (Fig. 3).[2,28]

The resting state of the enzyme is composed of two histidine residues and one of either Glu or Asp, along with three H_2O molecules bound in a distorted octahedron around an Fe^{II} metal centre (Fig. 3 (a)).[29–31] The αKG displaces two equatorial H_2O molecules, followed by substrate binding in a pocket near the active site, which also leads to a conformational change in the α-keto acid and loss of the final water residue (Fig. 3 (b)).[2] Subsequent reactions with O_2 are too rapid to allow isolation and spectroscopic characterisation of many of the proposed intermediates in Figure 3, however, using NO as a surrogate for O_2 allowed the structural characterisation of the Fe^{II}-αKG-NO species in clavaminic acid synthase (CAS).[32] The distal oxygen atom of NO was pointed towards the αKG group, providing the rationale for nucleophilic attack onto the electrophilic carbonyl group (Fig. 3 (c)). This was in contrast to the NO surrogate seen in IPNS (Fig. 1(c)) wherein the distal oxygen was instead positioned next to a C-H bond, primed for abstraction of a proton.[16] The contrasting reactivities of these Fe^{III}-superoxide intermediates suggest that the geometry of the superoxide moiety plays a significant role in their reactivity.

In the proposed mechanism, binding of O_2 causes the formation of a Fe^{III}-superoxide moiety which, after nucleophilic attack onto the carbonyl group of the αKG, leads to a Fe^{IV}-peroxyalkyl unit (Fig. 3 (d)). Subsequent C-C bond cleavage leads to loss of CO_2

and formation of the high valent Fe^{IV}=O oxidant (Fig. 3 (e)).[2] The Fe^{IV}=O species then abstracts a hydrogen atom from taurine (RH) (Fig. 3 (e)), followed by hydroxyl rebound (Fig. 3 (f)) to yield the hydroxylated product.[33] Use of $^{18}O_2$ has shown that the atoms of oxygen are incorporated into both the alcohol and carboxylate groups of the products, providing support for the nucleophilic attack onto αKG.[2] However, although the high valent Fe^{IV}=O has been characterised for TauD by Mössbauer spectroscopy and by kinetic studies,[27] in no enzyme has either the superoxide or peroxyalkyl intermediate been either trapped or spectroscopically characterised to date, thus why the synthesis of such intermediates have been so sought after in the recent years.[34]

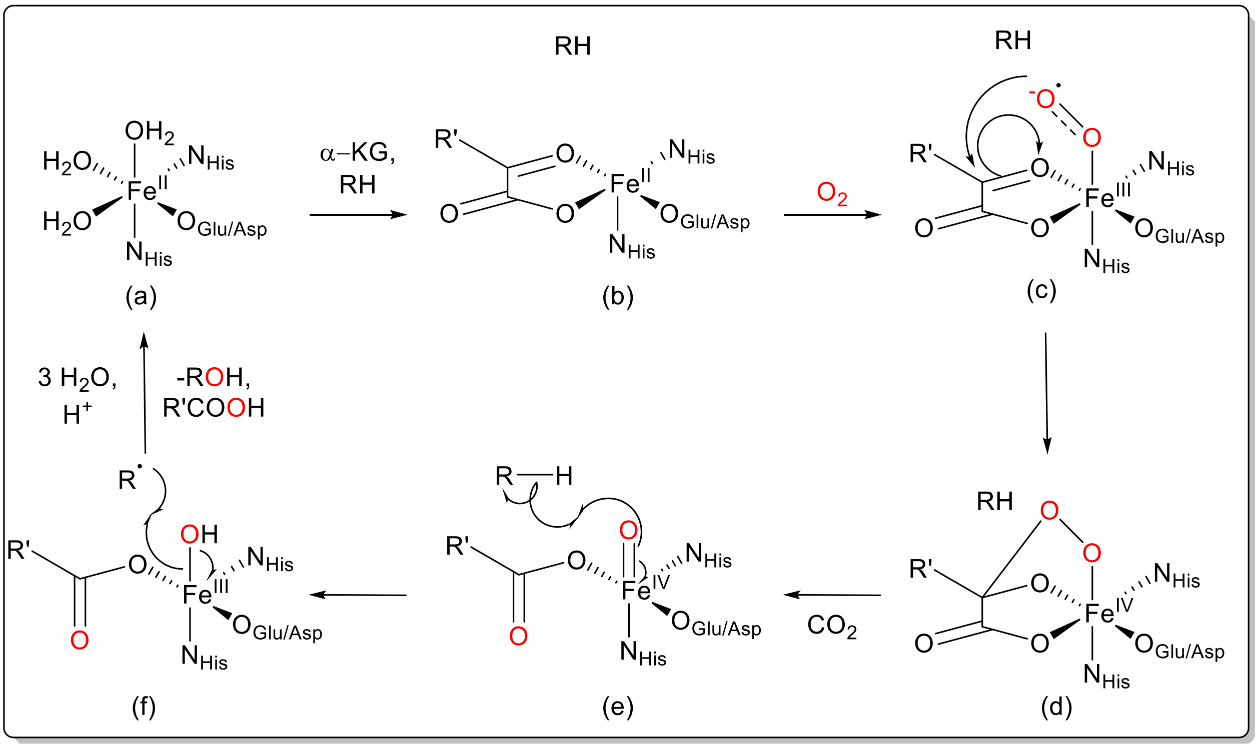

Figure 3. Proposed catalytic cycle of α-ketoglutarate dependent enzymes[34]

Evidence for the formation of a non-heme Fe^{III}-superoxide in α-ketoglutarate dependent enzymes is not directly supported by spectroscopic characterisation, instead its formation has been inferred. Structural studies of the NO surrogate complex showed the distal oxygen to be pointing to the carbonyl group of αKG, providing the rationale for nucleophilic attack of the Fe^{III}-superoxide, which leads to loss of CO_2 and formation of a high valent Fe^{IV}=O intermediate, which has been characterised. It is then this species which undergoes electrophilic oxidation of a nearby substrate. This reaction mechanism is in stark contrast to that of IPNS, wherein electrophilic oxidation occurs by both a superoxide intermediate and a high valent $Fe^{IV}=O$ species, formed further in the reaction cycle.

In all the above mentioned enzymatic catalytic cycles, there exists a dearth of structural information of the proposed superoxide intermediates, as well as little direct spectroscopic characterisation. Thus, it has been the goal of synthetic chemists to isolate such species and probe them spectroscopically in order to gain a better understanding of the properties which define their enzymatic reactivities.

1.3 Biomimetic Complexes of Metal Superoxide Intermediates

Characterisation of enzymatic processes and the intermediates thereof have historically been supported by, and in many cases given precedent by, synthetic mimics. Examination of the spectroscopic properties of a variety of metal superoxide complexes in the last number of decades has advanced understanding of the enzymatic processes discussed above. Due to their inherent instability and high reactivity, metal superoxide complexes are most commonly synthesised at low concentrations and at cryogenic temperatures in order to increase their half-life and thus allow their spectroscopic characterisation as well as to allow kinetic studies to be carried out.[24,25] A limited number of structural characterisations have been carried out on metal-superoxide complexes which are unusually thermally stable.[35–38]

1.3.1 Synthesis and Characterisation of Metal-Superoxide Complexes

In general, metal superoxide complexes can be formed by direct interaction of a metal and dioxygen (Equation (1)) or by reaction with potassium superoxide (KO_2) in a polar aprotic solvent (Equation (2)). In the majority of cases, these syntheses are carried out at sub-millimolar concentrations at cryogenic temperatures with the use of a low temperature UV-vis spectrophotometer. In this way, changes in the electronic spectrum can be used to assign the formation of new products and can be used to elucidate kinetic data from these processes.[24]

$$M^{n+} + O_2 \rightarrow M^{(n+1)+}\text{-}O_2^{\bullet-} \qquad (1)$$

$$M^{n+} + O_2^{\bullet-} \rightarrow M^{n+}\text{-}O_2^{\bullet-} \qquad (2)$$

One of the major difficulties in the identification and characterisation of metal-superoxide complexes is their similarity to metal-peroxide complexes, as well as their potential transformation into such species. Superoxide is the one-electron reduced form of oxygen, while peroxide is the two-electron reduced equivalent. Electrons are added to the π* orbital of oxygen leading to a reduction in the bond strength and thus vibrational frequency (ν(O-O)) as well as an increase in bond length.[24] Both species have been found to coordinate in either end-on, η^1, or side-on, η^2, modes.[25] Resonance Raman (rR) and/or infrared (IR) spectroscopies and structural analysis, along with complimentary theoretical studies, offer the best insight into the identification of a superoxide/peroxide complex and their differentiation.[24] The general vibrational and structural features of metal peroxide and superoxide bonds are summarised in Table 1.[24]

Table 1. General O-O bond features of metal superoxide and peroxide complexes[24]

O-O type	O-O bond length (Å)	ν(O-O) cm^{-1}
Superoxide	1.2 – 1.3	1050 – 1200
Peroxide	1.4 – 1.5	800 – 930

It must be noted that these are generalities and a number of metal-oxygen adducts exist with intermediary values. Therefore, spectroscopic techniques such as electronic spectroscopy (UV-vis), X-ray absorption spectroscopy (XAS), Mössbauer spectroscopy and EPR have historically been used in conjunction with vibrational and structural studies to give an adequate assessment of the electronic state of the oxygen adduct. Reactivity studies also provide a means of oxygen-adduct assignment due to the preference of peroxide complexes to act as nucleophilic oxidants,[25] while superoxide complexes primarily react as electrophilic oxidants, however, as will be discussed below, three examples of nucleophilic metal superoxide complexes have been reported in recent years.[39–41]

In terms of their prevalence, synthetic Cu^{II}- and Fe^{III}-superoxide complexes have historically been best studied and characterised However, there exists a variety of other transition metal superoxide complexes of which Ni^{II}-superoxide complexes will be discussed.

1.3.2 Copper Superoxide Complexes

Copper is one of the most prevalent transition metals found in biological systems, and as mentioned in the study of DBM and DHM, Cu^{II}-superoxide intermediates have been biologically implicated.[19,22] Synthetically, copper-oxygen adducts have been extensively analysed with the thermodynamic sink for copper-oxygen adducts being a trans-μ-1,2-peroxodicopper(II) system. Hence, most systems wherein a Cu^{II}-superoxide has been trapped employ relatively bulky ligand frameworks to inhibit this self-decay to the trans-μ-1,2-peroxodicopper(II) form.

The first example of a Cu^{II}-superoxide complex was reported in 1979 by Valentine and co-workers.[42] The reaction of $[Cu^{II}(\text{tet-b})](ClO_4)_2$, (tet-b = 5,7,7,12,14,14-hexamethyl-1,4,8,11-tetraazacyclotetradecane, Fig. 4) with KO_2 and 18 crown 6 ether (18-C-6) in dimethyl sulfoxide (DMSO) at room temperature yielded an intensely dark green coloured solution with an absorption feature at λ_{max} = 672 nm, which was stable for a number of days. This intense feature had been assigned as a ligand-to-metal charger-transfer (LMCT) band of a 5-coordinate $[Cu^{II}(\text{tet-b})(O_2)]^+$ species on the basis of previously characterised $[Cu^{II}(\text{tet-b})X)]^+$ ($X = OH^-$, F^-) having similar absorption features (λ_{max} = 670 and 690 nm respectively). EPR studies showed the loss of a signal on going from $[Cu^{II}(\text{tet-b})](ClO_4)_2$ to $[Cu^{II}(\text{tet-b})(O_2)]^+$, suggestive of antiferromagnetically coupling of a Cu^{II} ion with $O_2^{\bullet-}$. Furthermore, other $[Cu^{II}(\text{tet-b})X]^+$ type species were EPR active, $X = OH^-$, F^-.[42] No other spectroscopic characterisations for the formation of a Cu^{II}-superoxide species such as vibrational or structural studies were carried out, which would have provided significant evidence, however, this was the first meaningful attempt at Cu^{II}-superoxide characterisation.

Kitajima and co-workers reported the first structurally characterised Cu^{II}-superoxide complex in 1994.[43] The reaction of $[Cu^{I}(Tp^{iPr2})_3(DMF)]$ (Tp^{iPr2} = hydrotris(3-tert-butyl-5-isopropylpyrazol-l-yl)borate, Fig. 4) with 0.9 eq. O_2 in dichloromethane (DCM) yielded a red coloured solution at -50 °C, with UV-vis features at λ_{max} = 352 (2330 $M^{-1}cm^{-1}$), 510 (230 $M^{-1}cm^{-1}$), 660 (sh) nm. A solid bulk material was obtained upon recrystallisation of a saturated DCM solution of the formed intermediate at -20 °C. IR data yielded a ν(O-O) = 1112 cm^{-1} which shifted to 1062 cm^{-1}, upon substitution with $^{18}O_2$, which fell within the expected range of a metal superoxide complex (Table 1).[24] ^1H NMR spectroscopy and superconducting quantum interference device (SQUID) measurements confirmed the diamagnetic nature of the species, most likely through antiferromagnetic coupling of the Cu^{II} ion with the $O_2^{\bullet-}$ radical. Single crystal X-ray diffraction identified the copper intermediate as $[Cu^{II}(O_2)(Tp^{iPr2})]$, with the superoxide moiety bound in a side-on mode, having O-O = 1.22(3) Å, and of which the structure was highly similar to that of an analogous cobalt-superoxide complex.[43,44] A further two side-on Cu^{II}-superoxide complexes were structurally characterised[36,45–47] prior to the first end-on species in 2006 by Schindler and co-workers.[35]

Stopped-flow studies of the reaction of $[Cu^{I}(TMG_3\text{-tren})]^+$, ($TMG_3$-tren = 1,1,1-tris{2-[N(2)-(1,1,3,3-tetramethylguanidino)]ethyl}amine), Fig. 4) with O_2 at low temperatures in acetone yielded a dark-green solution with UV-vis features at λ_{max} = 442 and 690 nm. This reaction could be reversed via application of a vacuum to reform the Cu^{I} starting complex. rR studies identified the ν(O-O) stretch at 1117 cm^{-1}, which shifted to 1059 cm^{-1} upon substitution with $^{18}O_2$.[48] This was later measured by low temperature IR studies with the ν(O-O) stretch similarly at 1122 cm^{-1}, in close agreement with the rR studies.[35] Upon substitution with a mixed $^{16}O^{18}O$ sample, one new feature appeared in the rR spectrum, at 1089 cm^{-1}. This initially lead to the assignment of the complex as a side-on Cu^{II}-superoxide complex, as for an end-on species, two new features would be required to be present in the mixed isotope vibrational studies.[48] However, DFT studies showed that the end-on isomer did in fact have two highly similar resonances at 1083.1 and 1082.9 cm^{-1}, hence why only one new feature appeared in the rR studies, of which the $^{18}O^{16}O$ peak was spread over ~5 cm^{-1}. Single crystal XRD studies gave definitive proof of the end-on structure of the compound, with an O-O bond length of 1.280(3) Å, within the range expected for a metal-superoxide moiety (Table 1).[24,35]

In more recent years, Karlin, Solomon and co-workers have characterised a variety of Cu^{II}-superoxide complexes based on the TPA (TPA = Tris(2-pyridylmethyl)amine) framework.[49–54] In this work, they carried out a thorough analysis into what factors determine the stability of the superoxide intermediates.[51–53] They showed that there were a number of ways of minimising formation of the trans-μ-1,2-peroxodicopper(II) species; increasing electron donation to Cu, steric effects to prevent the approach of a second equivalent of Cu^{I}, changing the coordination number, use of cryogenic conditions and through both intermolecular and intramolecular H-bonding stabilisation.

Initial studies involved the formation of $[Cu^{II}(TPA)(O_2^{\bullet -})]^+$ (Fig. 4) from its Cu^I precursor and dioxygen with corresponding UV-vis features at λ_{max} = 410 (4000 $M^{-1}cm^{-1}$), 747 (1000 $M^{-1}cm^{-1}$). However, this species decayed very rapidly to the thermodynamically favoured trans-μ-1,2-peroxodicopper(II) species $[Cu^{II}(TPA)(O_2)]_2^{2+}$ (λ_{max} = 525 (1500 $M^{-1}cm^{-1}$), 440 (sh), 595 (sh), at -90 °C).[49]

The stronger electron donating ligand NMe_2-TPA (NMe_2-TPA = tris-(N,N-dimethylamino-2-ylmethyl)amine) analogue was used, allowing the formation of $[Cu^{II}(NMe_2\text{-}TPA)(O_2)]^+$ (Fig. 4) in THF at -85 °C, while limiting the decay of the complex to the trans-μ-1,2-peroxodicopper(II) species.[51] This species had similar UV-vis features as the TPA analogue, λ_{max} = 418 (4300 $M^{-1}cm^{-1}$), 615 (1100 $M^{-1}cm^{-1}$), 767 (840 $M^{-1}cm^{-1}$), and was characterised further as a Cu^{II}-superoxide by rR, ν(O-O) = 1121 cm^{-1} (ν(^{18}O-^{18}O) = 1058 cm^{-1}). Substitution with a mixture of 1:2:1 $^{16}O_2$:$^{16}O^{18}O$:$^{18}O_2$ gave a 1:2:1 ratio of 1121, 1091 (ν(^{18}O-^{16}O) and 1058 cm^{-1} peaks in rR. The ν(Cu-^{16}O) and ν(Cu-^{18}O) peaks in this mixed gas sample, were present in equal intensities, suggesting the binding mode of the Cu-superoxide unit was end-on. A symmetrical side-on bound Cu^{II}-superoxide unit would only have had a single, averaged ν(Cu-O) peak.[55] The $[Cu^{II}(NMe_2\text{-}TPA)(O_2)]^+$ species was EPR silent due to coupling of the unpaired spin of the Cu^{II} and $O_2^{\bullet -}$.[51]

More recently has been synthesised the first N_3S ligated Cu^{II}-superoxide complex, which more accurately reflected the active site of PHM and DBM.[53] This species was formed from the reaction of $[Cu^I(^{DMA}N_3S)]^+$ ($^{DMA}N_3S$ = 2-((((4-(N,N-dimethylamino)pyridin-2-yl)methyl)(2-((2-methylbenzyl)thio)ethyl)amino)methyl)-N,N-dimethylpyridin-4-amine, Fig. 4) and O_2 in 4:1 trifluoroethanol (TFE) : 2-methyl-THF (Me-THF) at -125 °C, characterised by UV-vis (λ_{max} = 418, 605, 743) and rR (ν(O-O) = 1117 and ν(^{18}O-^{18}O) = 1056 cm^{-1}) .[53] Steric protection by the *o*-methyl benzyl substituent prevented formation of the trans-μ-1,2-peroxodicopper(II) decay product. [53,56–59] It was also proposed that the use of the potential H-donor TFE solvent stabilised the Cu^{II}-superoxide intermediate, as in its absence, decay to the trans-μ-1,2-peroxodicopper(II) occurred in 50 s.[53]

Investigation into H-bonding stabilisation effects on the Cu^{II}-superoxide intermediate were carried out with 4 complexes which had varying degrees of H-bonding, based on their pKa, of the form, $[(L)Cu^{II}(O_2)]^+$, where L = TPA, BA, F_5BA and MPPA, (BA = N-benzyl-6-((bis(2-pyridylmethyl)amino)methyl)pyridin-2-amine, F_5BA = 6-((bis(2-pyridylmethyl)amino)methyl)-N-((perfluorophenyl)methyl)pyridin-2-amine, MPPA = bis(2-pyridylmethyl)((6-(pivalamido)pyrid-2-yl)methyl)amine, Fig. 4). The characteristic UV-vis and rR data of the complexes are presented in Table 2. Of importance was the concentration of observable trans-μ-1,2-peroxodicopper(II) present in the UV-vis spectra of the intermediates. As H-bonding interactions increased, (TPA < BA < F_5BA < MPPA), the concentration of trans-μ-1,2-peroxodicopper(II) decreased, due to stabilisation of the Cu^{II}-superoxide moiety.[52] The UV-vis feature located at ~ 420 nm was a ligand-to-metal charger transfer (LMCT) band from a doubly occupied π^* $O_2^{\bullet -}$ based orbital to the metal. As H-bonding reduced the electron density in the orbital, charge transfer required higher energy, hence the blue shift. This was reflected in an increase in the bond strength and thus an increase in vibrational energy of the O-O bond, as electron density was withdrawn from the antibonding orbital by H-bonding.[52]

Table 2. Summary of the UV-vis and vibrational data of $[Cu^{II}(L)(O_2^{\bullet -})]^+$. Adapted from ref[52]

$[Cu^{II}(L)(O_2^{\bullet -})]^+$	λ_{max} (nm($M^{-1}cm^{-1}$))	ν(O-O) (cm^{-1})	$\Delta^{16}O_2$-$^{18}O_2$ (cm^{-1})
TPA	423(5600) 752	1119	61
BA	418(4100) 750	1123	64
F_5BA	414(4000) 748	1126	64
MPPA	410(3700) 741(1150)	1130	63

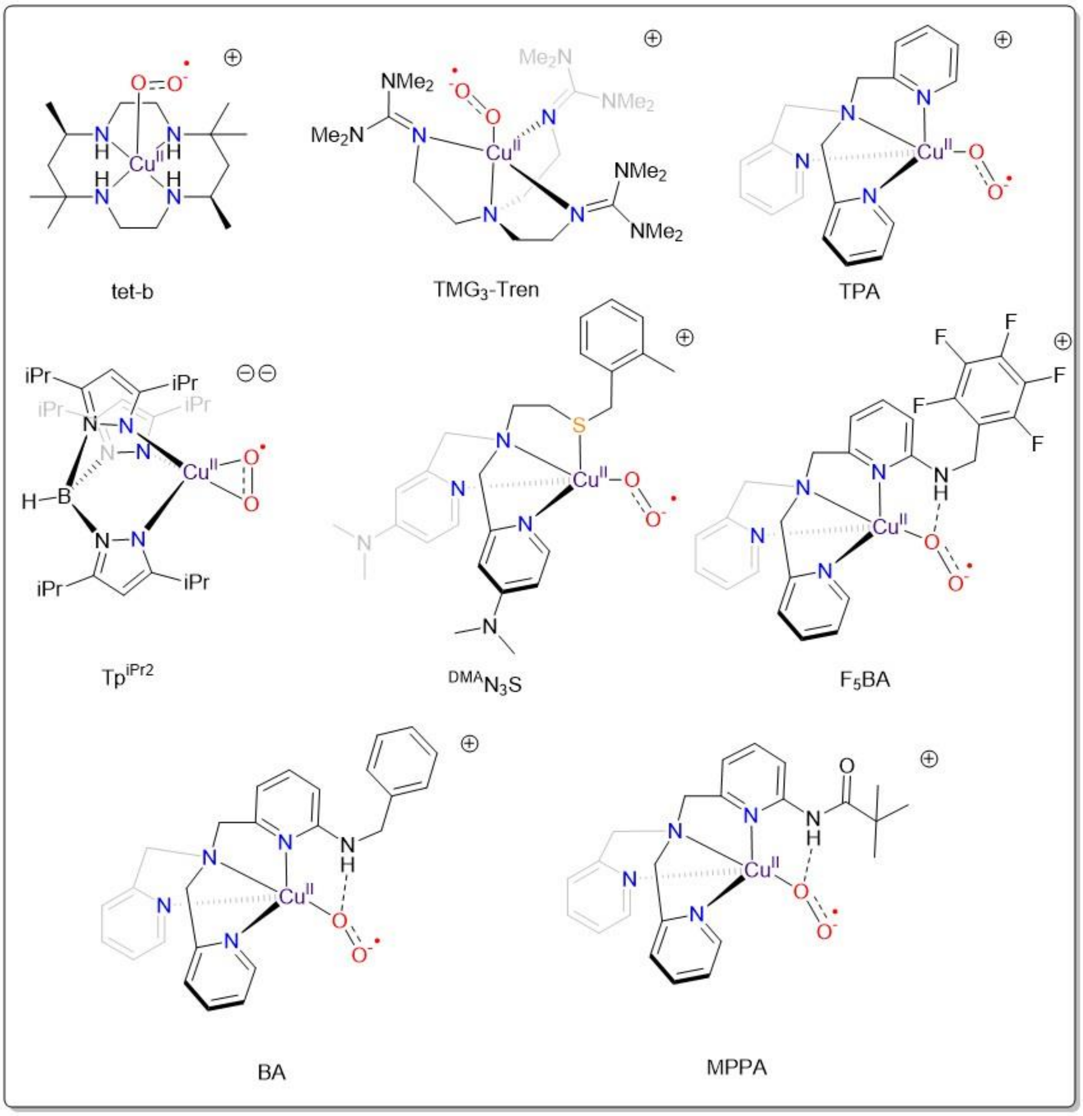

Figure 4. Examples of Cu^{II}-superoxide complexes

Overall, Cu^{II}-superoxide complexes have been extensively spectroscopically and structurally characterised. As has been discussed, systems wherein stabilising factors such as steric bulk or intramolecular interactions have yielded the most success in the isolation of these intermediates due to their ability to inhibit the formation of the trans-μ-1,2-peroxodicopper(II), which acts as the thermodynamic sink for Cu^{II}-oxygen adducts. However, as will be discussed below, all but one example of these species react as electrophilic oxidants and the properties which define this reactivity are still not understood.

1.3.3 Iron Superoxide Complexes

1.3.3.1 Indirect Evidence for transient Iron Superoxide Formation

Iron is the most biologically relevant transition metal in relation to metal superoxide intermediates due to the volume of known αKG dependent enzymes. While several such species have been spectroscopically characterised, and one case of a structural characterisation is known, a number of studies have shown indirect evidence for the formation of Fe^{III}-superoxide intermediates. This was achieved by identification of higher-order oxidation states of Fe-oxygen adducts such as peroxide and hydroperoxide, or by the oxidation reactions which take place preceding their formation.[9,60]

Nam and co-workers provided a rationale for the indirect identification of the superoxide complex, $[Fe^{III}(TMC)(O_2)]^{2+}$ (TMC = 1,4,8,11-tetramethyl-1,4,8,11-tetraazacyclotetradecane, Fig. 5).[61] Reaction of a solution of $[Fe^{II}(TMC)]^{2+}$ with an olefin, such as cyclohexene, in acetonitrile (NCMe) at 25 °C, under atmospheric conditions, yielded the previously characterised $[Fe^{IV}(TMC)(O)]^{2+}$ species and a mixture of oxidation products; 2-cyclohexen-1-ol (26(4) %), 2-cyclohex-1-one (21(3) %), 1,3-cyclohexadiene (9(2) %) and benzene (5(2) %).[60,61] The oxygen atom of the oxidised products were determined to be from O_2 from $^{18}O_2$ labelling experiments, and kinetic measurements showed the rate of the reaction to be linearly correlated to the C-H bond strength of the olefin used (cyclohexene > cycloheptene > cyclooctene). A KIE of 6.5 using cyclohexene-d_{10} implicated C-H bond cleavage as the rate determining step (RDS). Thus, it was proposed that the reaction must have gone through a $[Fe^{III}(TMC)O_2]^{2+}$ intermediate which carried out the HAT on the olefin yielding $[Fe^{III}(TMC)O_2H]^{2+}$ and a carbon-based radical, which were both incapable of being trapped. However, carrying out the reaction in the presence of a base, triethylamine (NEt_3), allowed the trapping and characterisation of the peroxide product $[Fe^{III}(TMC)O_2]^{+}$, formed through the deprotonation of a proposed $[Fe^{III}(TMC)O_2H]^{2+}$, providing further evidence for the postulated transient Fe^{III}-superoxide intermediate.[61]

Que and co-workers gave precedent also for the indirect identification of metal superoxide complexes by the reaction of $[Fe^{II}(Tp^{iPr2})(O_2CCOPh)]$ (Fig. 5) with dioxygen at -40 °C in NCMe.[9] This yielded a species with UV-vis features at λ_{max} = 680 nm (1600 $M^{-1}cm^{-1}$) which was additionally characterised by rR (ν(O-O) = 889, ν(Fe-O) = 424, ν(^{18}O-^{18}O) = 842, ν(Fe-^{18}O) = 408 cm^{-1}) and Mössbauer spectroscopy (ΔE_Q = 1.32(3) mm/s, δ= 0.65(2) mm/s). The vibrational data for the O-O bond matched that expected for a peroxide complex (Table 1), while the Mössbauer parameters matched well with a simulation of a diiron(III) peroxide which was diamagnetically coupled. Thus, the intermediate was concluded to be a diiron(III) peroxide adduct.[9] This dinuclear peroxide complex was not formed in the presence of 2,4,6-tri-tert-butylphenol, instead the absorption spectrum showed three UV-vis features at λ_{max} = 373, 400 and 620 nm which were characteristic of the corresponding phenoxyl radical formed, implicating the formation of a putative Fe^{III}-superoxide species which then cleaved the O-H bond of the phenol.[9]

Thus, in the above two cases, although direct spectroscopic evidence was lacking, sufficient indirect evidence existed to postulate the role of Fe^{III}-superoxide in each study.

1.3.3.2 Spectroscopic Characterisation of Iron Superoxide Complexes

Que and Shan synthesised the first nonheme Fe^{III}-superoxide complex which was spectroscopically characterised in 2005.[62] The intermediate was formed from the reaction of $[Fe^{II}_2(\mu\text{-}OH)_2(6\text{-}Me_3\text{-}TPA)_2](OTf)_2$ ($6\text{-}Me_3$-TPA = Tris(6-methyl-2-pyridylmethyl)amine, Fig. 5) with O_2 at -80 °C in DCM over 1 h and was characterised by UV-vis features at λ_{max} = 325 (10300 $M^{-1}cm^{-1}$), 500 (1400 $M^{-1}cm^{-1}$) and 620 nm (1200 $M^{-1}cm^{-1}$), formed with a second order rate constant of $8 \pm 0.1*10^{-2}$ $M^{1}s^{-1}$ and activation parameters of $\Delta H = 16 \pm 2$ $KJmol^{-1}$ and $\Delta S = -167 \pm 10$ $Jmol^{-1}s^{-1}$. rR studies exhibited a ν(O-O) peak at 1310 cm^{-1} which shifted by 71 cm^{-1} upon substitution with $^{18}O_2$. Synthesis of the intermediate with a 50 % ^{18}O-enriched O_2 sample yielded a doublet at 1262 and 1282 cm^{-1} which were used to assign the Fe^{III}-superoxide species as an end-on unit (two values expected for $^{18}O^{16}O$).[62] The rR value of 1310 cm^{-1} was one of the highest known vibrational bands of any superoxide moiety and was indicative of strong superoxide character. This was likely due to the steric hindering of the 6-methyl groups of the ligand which lengthened the Fe-N bond and in doing so increased the Lewis acidity of the metal, reducing the donation of electron density onto the oxygen unit, which was reflected in the reaction entropy.[62]

Way-Zen Lee and co-workers synthesized and spectroscopically characterised the first example of a mononuclear nonheme Fe^{III}-superoxide complex in 2014.[63] The reaction of the 5-coordinate Fe^{II}(BDDP) (BDDP = 2,6-bis ((2-(diphenylhydroxymethyl)-1-

pyrrolidinyl) methyl)pyridine, Fig. 5) with O_2 in tetrahydrofuran (THF) at -80 °C yielded a yellow solution with a UV-vis feature at λ_{max} = 330 nm (ε = 9400 $M^{-1}cm^{-1}$). This was highly similar to that of the O_2 adduct of $[Fe^{II}_2(\mu\text{-}OH)_2(6\text{-}Me_3\text{-}TPA)_2]^{2+}$ in DCM which had an absorption feature at 335 nm, assigned as a superoxide-to-metal charge transfer band.[62] The O_2 adduct of Fe^{II}(BDDP) could reversibly form the starting material by bubbling with N_2 at -80 °C. rR showed an O_2 sensitive band at 1125 cm^{-1} which shifted to 1062 cm^{-1} upon substitution with $^{18}O_2$, within the range expected for a superoxide adduct (Table 1). Mössbauer spectroscopy was used to obtain an isotope shift of δ = 0.58(3) mm/s which matched values of other high spin Fe^{III} complexes providing further evidence for the nature of the O_2 adduct to be assigned as a high spin Fe^{III}-superoxide complex, most likely coordinated in an end-fashion due to the 5-coordinate precursor having only a single vacant site for binding to occur.[63]

The first structurally characterised nonheme Fe^{III}-superoxide complex was characterised by Nam and co-workers.[39] $Na[Fe^{III}(TAML)]$ (TAML = tetraamido macrocyclic ligand) was reacted with KO_2 and 2.2.2-cryptand in NCMe at 5 °C which immediately caused the formation of a red solution with a UV-vis feature at λ_{max} = 490 nm (2600 $M^{-1}s^{-1}$). Electrospray ionisation mass spectrometry (ESI-MS) gave an isotope sensitive peak (m/z = 873.1 $[K(2.2.2\text{-cryptand})Fe^{III}(TAML)(O_2)]^-$, m/z = 877.1 $[K(2.2.2\text{-cryptand})Fe^{III}(TAML)(^{18}O_2)]^-$). This species was EPR silent at 4.2 K with a magnetic moment of 3.26 μ_B at -20 °C, obtained via the Evans method, which suggested an S = 1 electronic ground state. Low temperature IR measurements in NCMe at -40 °C revealed an ν(O-O) band at 1260 cm^{-1} which shifted to 1183 cm^{-1} upon substitution with $^{18}O_2$ (Δ = 77 cm^{-1}).[39] Mössbauer yielded parameters of δ = 0.10 mm/s and ΔE_Q = 2.66 mm/s, which matched those of other TAML complexes with S = 3/2 Fe^{III} centres.[64] Theoretical studies matched those of the experimental Mössbauer values. From the above data, the intermediate was predicted to be a $[Fe^{III}(TAML)(O_2)]^{2-}$ (Fig. 5) type species with an S = 3/2 ground electronic state Fe^{III} atom coupled to an S = 1/2 $O_2^{\bullet-}$. Single crystal XRD analysis yielded a crystallographic unit with 2 independent crystallographic molecules, one of which was disordered over two positions. The Fe^{III}-superoxide complex was found in a pseudo-square pyramidal structure with a side-on bound oxygen adduct with O-O = 1.323(3) Å, 1.306(7)/1.315(12) Å and with average Fe-O = 1.927 Å for the two crystallographically independent units, much shorter than those of characterised Fe^{III}-

peroxide intermediates in enzymes, but relatively very similar to the that of the Fe^{III}-superoxide unit found in homoprotocatechuate (1.34 Å).[65]

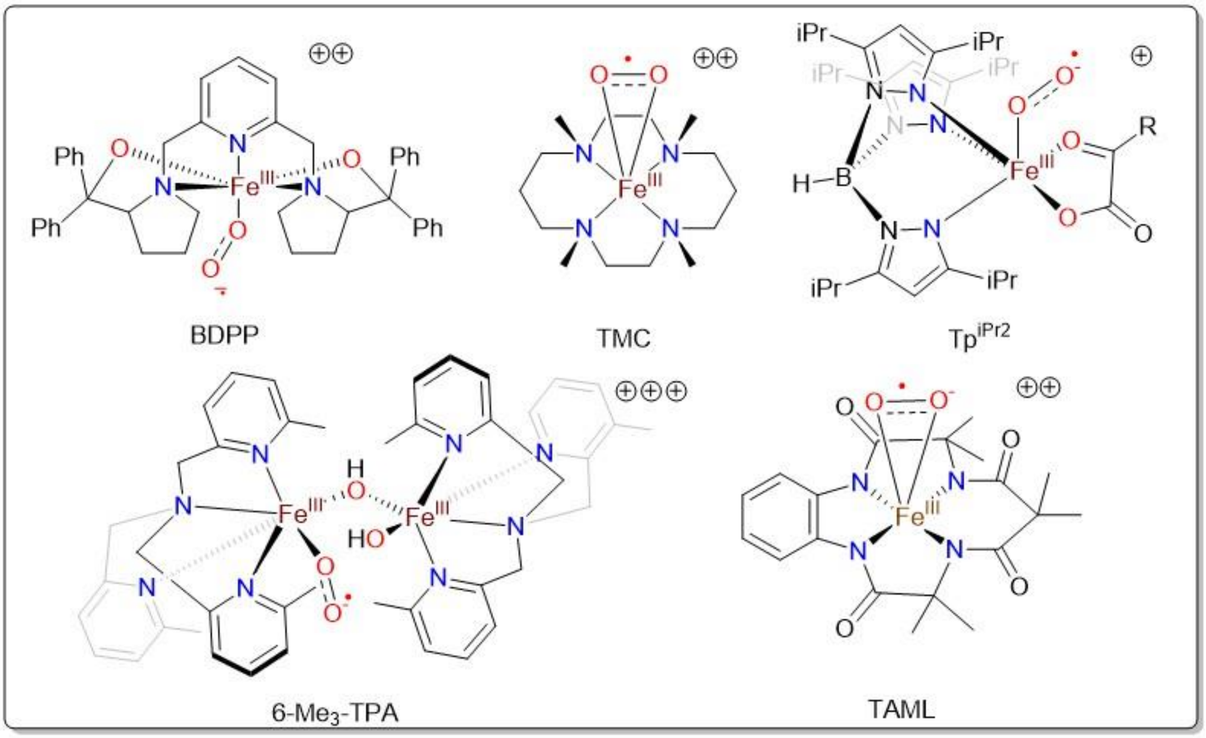

Figure 5. Examples of Fe^{III}-superoxide complexes

Thus, from the discussion of Fe^{III}-superoxide complexes above, structural characterisation of such complexes have proven much more difficult than their Cu^{II}-superoxide equivalents. The factors detailing the stabilisation of Cu^{II}-superoxide complexes are better understood than for their Fe^{III}-superoxide counterparts. Thus, further studies into the thermal stabilisation of Fe^{III}-superoxide complexes is needed to compliment the library of available spectroscopic characterisation data. However, as for the Cu^{II}-superoxide complexes mentioned previously, the properties defining the reactivity mode of these species are still not understood and the ability to tune a complex to react as an electrophile or nucleophile has not been accomplished.

1.3.4 Nickel Superoxide Complexes

The number of Ni^{II}-superoxide complexes which have been spectroscopically characterised are markedly less than for Cu^{II} and Fe^{III}. Most methods involve either the reaction of Ni^I precursors with O_2,[38,66–68] or by direct reaction of Ni^{II} complexes with excess H_2O_2 and a base.[41,69,70]

The first reported such species was $[Ni^{II}_2(\mu\text{-}O_2)_2(6\text{-}Me_3\text{-}TPA)_2]^{2+}$ (Fig. 6), formed from the reaction of the previously characterised $[Ni^{II}_2(\mu\text{-}OH)_2(6\text{-}Me_3\text{-}TPA)_2](BF_4)_2$ with concentrated H_2O_2 in the presence of n-Bu_4NOH in MeOH at -60 °C.[69] It was characterised by rR (ν(O-O) = 1096 cm^{-1}, ν(^{18}O-^{18}O) = 1044 cm^{-1}, Δ = 52 cm^{-1}), ESI-MS (m/z = 422 $[Ni(O_2)(6\text{-}Me_3\text{-}TPA)]^+$, m/z = 426 $[Ni(^{18}O_2)(6\text{-}Me_3\text{-}TPA)]^+$ in acetone) and single crystal XRD (O-O = 1.345(6) Å). The vibrational data allowed the assignment of the bound O_2 adduct as a superoxide moiety (Table 1), while the bond length was in between the range of superoxide and peroxide bond lengths. ESI-MS data corresponded to the monomeric Ni^{II}-superoxide unit, suggesting it could form a monomer either in solution or in the highly energising mass spectrometer itself.[69]

The first monomeric Ni^{II}-superoxide complex was characterised in 2004 by Riordan and co-workers as the side-on superoxide complex $[Ni^{II}(PhTt^{Ad})(O_2)]$ (PhTt^{Ad} = phenyltris((1-adamantylthio)methyl)borate, Fig. 6), formed from the reaction of $[Ni^I(PhTt^{Ad})]$ and O_2 in toluene at -70 °C.[67] EPR gave a rhombic signal with values of $g_x = 2.24$, $g_y = 2.19$ and $g_z = 2.0$, with an S = ½ ground state, with the unpaired electron located mainly in the $d_z{}^2$ orbital of Ni^{II}. XAS showed a pre-edge 1s → 3d transition energy centred at 8331.4 eV, within the range expected of Ni^{II}, while EXAFS gave 3 Ni-S$_{av}$ = 2.26 Å and 2 Ni-O$_{av}$ = 1.85 Å.[67] DFT calculations suggested a high spin square pyramidal structure wherein the $d_{x2\text{-}y2}{}^{(1)}$ electron of the S = 1 Ni^{II} was antiferromagnetically coupled to the $\pi^{*(1)}$ electron of the $O_2{}^{\bullet -}$, leaving a single unpaired electron in the $d_{x2}{}^{(1)}$ to account for the S = ½ EPR signal.[67]

Following this work, Riordan and co-workers characterised the first end-on Ni^{II}-superoxide complex, $[Ni^{II}(TMC)(O_2)]^+$ (Fig. 6), which was formed from the reaction of the peroxide species $[(Ni^{II}(TMC))_2(\mu\text{-}O_2)]^{2+}$, which itself was synthesised from the reaction of O_2 and $[Ni^I(TMC)](OTf)$ and excess O_2 in THF at -78 °C, or from reaction of $[Ni^{II}(TMC)](X)_2$ (X = OTf or ClO_4) with H_2O_2 and a base in NCMe/MeOH at 25 °C.[68] It was characterised by UV-vis (λ_{max} = 345 (1500 M^{-1}cm^{-1}), 328 (sh)), rR (ν(O-O) 1131 cm^{-1}, 1067 cm^{-1} ν(^{18}O-^{18}O) (Δ = 64 cm^{-1})), EPR (rhombic, $g_x = 2.29$, $g_y = 2.21$, $g_z = 2.09$ with S = ½ electronic ground state), XANES (pre-edge 1s → 3d transition = 8333.9 eV

(Ni^{II}) and EXAFS, 1 Ni-O/N = 1.98 Å and 4 Ni-N/O = 2.17 Å).[68] rR data was within the expected range of a superoxide complex, while EPR data suggested that the unpaired spin was located primarily on the 5-coordinate Ni^{II}, as in the previously described [Ni^{II}($PhTt^{Ad}$)(O_2)] complex.[67] The DFT optimised structure gave a Ni-O bond length of 1.84 Å, matching that of the EXAFS data, and an O-O bond length of 1.3 Å, which fell into the expected range for a superoxide moiety (Table 1).[68]

The first structurally characterised mononuclear Ni^{II}-superoxide complex was more recently reported by Driess and co-workers as the square planar, side-on superoxide, complex [Ni^{II}(nacnac)(O_2)] (nacnac = β-diketiminato, Fig. 6).[38] The O-O bond length of 1.34 Å was similar to that found in [Ni^{II}_2(μ-O_2)$_2$(6-Me_3-TPA)$_2$](BF_4)$_2$.[69] EPR of the square planar complex yielded a rhombic signal with g_x = 2.138,g_y = 2.116 and g_z = 2.067, an S = ½ ground state centred on the $O_2^{\bullet -}$ moiety. These values differed only slightly and followed the same general pattern as free $O_2^{\bullet -}$ (g = 2.10, 2, 1.98). DFT calculations confirmed the unpaired electron as being present in the π* orbital of $O_2^{\bullet -}$. rR measurements also yielded ν(O-O) values of 971 and 919 cm^{-1} for $^{16}O_2$ and $^{18}O_2$ generated species respectively.[38] To date, this remains the sole structural characterisation of a mononuclear Ni^{II}-superoxide complex, although three other complexes have been spectroscopically characterised[38,41,70] and one other species has tentatively been assigned as being present in equilibrium with a peroxide analogue.[66] A summary of all characterised Ni^{II}-superoxide intermediates is found in Table 3 below.

Table 3. Major spectroscopic data of Ni^{II}-superoxide complexes

N^{II} complex	Binding mode	Ni^{II} coord.	ν (^{16}O-^{16}O) /cm^{-1}	ν (^{18}O-^{18}O) /cm^{-1}	Δν /cm^{-1}	λ$_{max}$ nm (M^{-1}cm^{-1})	Ref
[Ni^{II}(PhTtAd)(O$_2$)]	Side-on	5C					[67]
[Ni^{II}(nacnac)(O$_2$)]	Side-on	4C	971	919	61		[38]
[Ni^{II}(Bi^{iPr2})(O$_2$)]$^-$	Side-on	4C	980	932	48	300(sh) 455(900)	[41]
[Ni^{II}(TMC)(O$_2$)]$^-$	End-on	5C	1131	1067	64	328(sh) 345(1500)	[68]
[Ni^{II}(13-TMC)(O$_2$)]$^+$	End-on	5C	1130	1070	60	339(800) 416(130) 684(60)	[70]
[Ni^{II}(iso-pmbox)(O$_2$)]$^+$	End-on	4C					[66]
[Ni$^{II}_2$(O$_2$)$_2$(6-Me$_3$-TPA)$_2$]$^{2-}$	Bridging (End-on)	6C	1096	1044	52		[69]

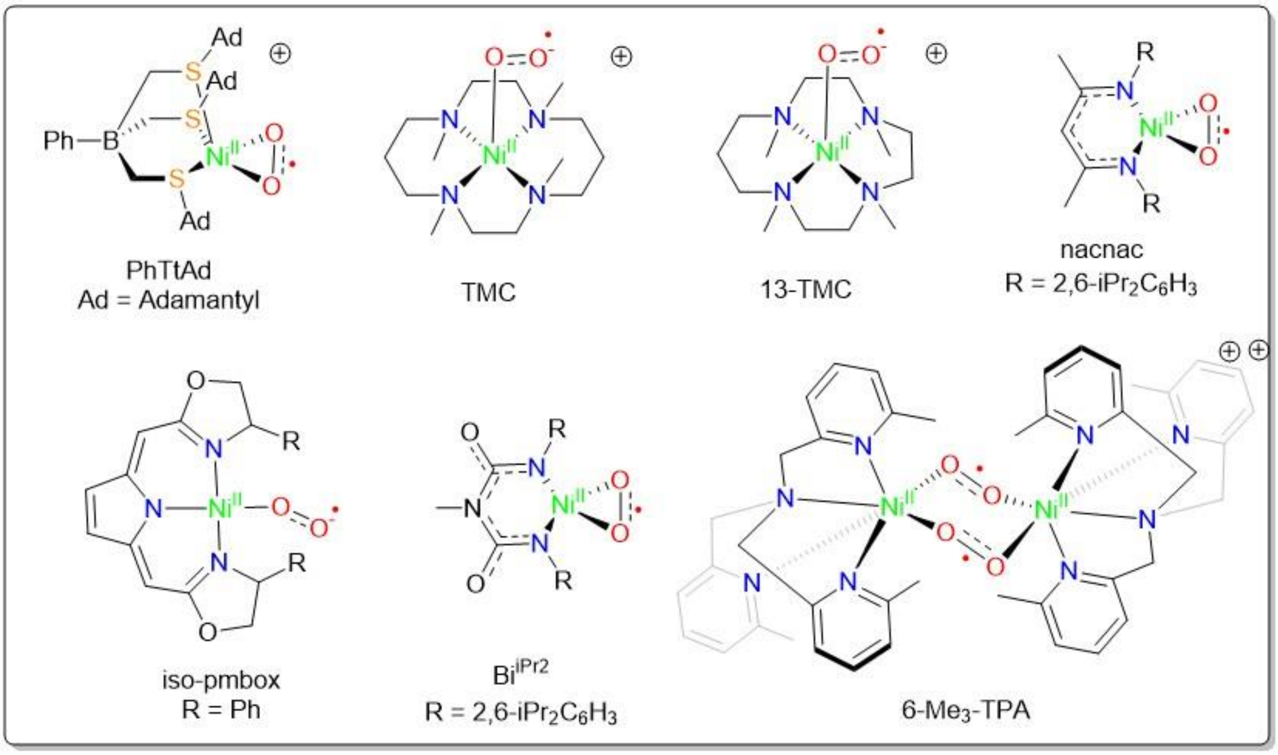

Figure 6. All spectroscopically characterised Ni^{II}-superoxide complexes (PdmBox = 5-phenyl-2-((5-((4-phenyl-4,5-dihydrooxazol-2-yl)methyl)-1,5-dihydro-2-pyrrol-2-ylidene)methyl)-4,5-dihydrooxazole).

Thus, the prevalence of the Ni^{II}-superoxide is much less than those of Cu^{II} and Fe^{III}. Structural studies have only been carried out on one isolated complex, and thus, the factors which allow the thermal stabilisation of such species are as of yet unknown. Further studies of Ni^{II}-superoxide complexes are required in order to understand this class of compounds and to understand how their properties differ from those of the more commonly studied Fe^{III}- and Cu^{II}-superoxide complexes, as well as the properties which define their reactivities.

1.4 Reactivity of Metal superoxide complexes

As already discussed, enzymatic metal superoxide complexes can react primarily in one of two ways; either as electrophilic oxidants,[11] or as nucleophilic oxidants.[2] Strikingly, the vast majority of synthetic metal superoxide complexes react as electrophiles, effecting cleavage of either C-H or O-H bonds of substrates. There are only three examples of metal superoxide complexes which display nucleophilic reactivity, wherein the superoxide actively attacks an electrophilic carbonyl group of a substrate.[39–41] This dearth of nucleophilic metal superoxide complexes is in stark contrast to biology wherein a wealth of such reactions are hypothesised, none more so than in the αKG dependent enzymes.[26,27]

1.4.1 Electrophilic Metal Superoxide complexes

Electrophilic oxidation reactions involved the cleavage of a C-H or O-H bond, HAT, of a hydrocarbon or phenol or can also involve the transfer of an oxygen atom, OAT, to a phosphine or sulphide species. In the studies of the reaction of Nam's $[Fe^{II}(TMC)]^{2+}$ and Que's $[Fe^{II}(Tp^{iPr2})(O_2CCOPh)]$ complexes with O_2, indirect evidence for the formation of putative metal superoxide species was obtained by their reactions with olefins and phenols respectively.[9,60] The reaction of $[Fe^{II}(TMC)]^{2+}$ with O_2 in the presence of cyclohexene led to the formation of 2-cyclohexen-1-ol (26(4)%), 2-cyclohex-1-one (21(3)%), 1,3-cyclohexadiene (9(2)%) and benzene (5(2)%)[60,61]. Importantly, using $^{18}O_2$ led to incorporation of ^{18}O into the allylic products. The reaction proceeded with pseudo-first order kinetics and the first order rate constant, k_1, for the product, $[Fe^{IV}(TMC)(O)]^{2+}$, was linear with respect to C-H bond strength of the olefin used.[60] k_{obs} was obtained by fitting the absorbance at 820 nm (formation of $[Fe^{IV}(TMC)(O)]^{2+}$) against time, and this allowed the second order rate constants, obtained by plotting k_{obs} vs. [substrate], to be determined and which yielded a linear plot, showing formation of $[Fe^{IV}(TMC)(O)]^{2+}$ was fastest with weak C-H bonds. Also, a KIE of 6.3 was obtained by comparison of the rates of cyclohexene and d_{10}-cyclohexene, providing proof for HAT as the RDS of the reaction. Thus, these results provided the rationale for the electrophilic HAT of a C-H bond of cyclohexene in order to form the various products by a number of radical reactions.[60]

Similarly, for the reaction of $[Fe^{II}(Tp^{iPr2})(O_2CCOPh)]$ with O_2 at room temperature yielded an alkoxo-Fe^{III} product which was characterised by ESI-MS with an m/z = 536 which matched well with $[[Fe^{III}(Tp^{iPr2})] + O - H]^+$. A hydrogen atom of the ligand had been replaced by an oxygen atom, providing precedent for the hydroxylation of the ligand, which was also concurred by post-reaction acidified work-up. A ^1H NMR spectrum showed that the three pyrazole rings of the Tp^{iPr2} ligand had become inequivalent, with a ratio of 2:1.[9] As previously mentioned, addition of 2,4,6-tri-tert-butylphenol (TTBP) to the reaction mixture prevented formation of the Fe_2^{III} peroxide product, instead giving the phenoxy radical product. The phenoxy radical formed with a first order rate constant of 2.1(4) $*10^{-2}$ $M^{-1}s^{-1}$ which was unaffected by substrate concentration. This suggested that the RDS of the oxidation of the phenol was not via O-H cleavage, but instead in oxidant formation, which was quite an unusual occurrence.[9]

Solomon and Karlin's study into the H-bonding effects on the stabilisation of Cu^{II}-superoxide intermediates was also reflected in their reactivities as electrophilic oxidants.[52] The superoxide intermediates were reacted with 2,6-di-tert-butylphenol (DTBP) (BDE = 82.0 kcal/mol) and 4-methoxyphenol (MP) (BDE = 87.6 kcal/mol) in Me-THF at -135 °C and the results are summarised in Table 4 below. The products of the reaction with DTBP were the Cu^{II}-O_2H and the corresponding phenoxy radical, demonstrating a net hydrogen atom abstraction from the phenol.[52] As can be seen from the second order rate constants of DTBP, as the H-bonding effects of the ligand increased, so too did the rate, due to the stabilisation of the π^* orbital of the $O_2^{\bullet -}$ moiety which in turn increased the electrophilicity of the intermediate.[52] This trend was broken for MPPA, which had a stronger O-O bond that F_5BA, due to sterics, the bulky nature of the MPPA ligand prevented the approach of the bulky DTBP substrate. Similar results were seen using MP as the substrate.

Table 4. Summary of kinetic data for $[Cu^{II}(L)(O_2^{\bullet -})]^+$

$[Cu^{II}(L)(O_2^{\bullet -})]^+$	$k_{2(DTBP)}$ ($M^{-1}s^{-1}$)	$k_{2(MP)}$ ($M^{-1}s^{-1}$)
TPA	$3.11 * 10^{-1}$	-
BA	$5.73 * 10^{-1}$	Very slow
F_5BA	$11.47 * 10^{-1}$	Much faster
MPPA	$9.88 * 10^{-1}$	$2.33 * 10^{-2}$

$[Ni^{II}(TMC)(O_2)](OTf)$ has been shown to effect OAT reactions, wherein PEt_3 was oxidised to $OPEt_3$.[70] Likewise, $[Ni^{II}(13\text{-}TMC)(O_2)]^+$ and $[Ni^{II}(PhTt_{Ad})(O_2)]$ have been shown to oxidise PPh_3 to $OPPh_3$, while $[Ni^{II}(PhTt_{Ad})(O_2)]$ has also been shown to be an effective oxidiser of NO to NO_3.[67,68]Perhaps surprisingly, Ni^{II}-superoxide complexes, although spectroscopically characterised, have not been widely investigated regarding their reactivity. Indeed, of all of the previously mentioned Ni^{II}-superoxide complexes, only the nacnac complex has been investigated thoroughly regarding its reactivity.[38,71]

An in depth study was performed on $[Ni^{II}(nacnac)(O_2)]$ by Driess and co-workers.[71] $[Ni^{II}(nacnac)(O_2)]$ was found to be unable to perform OAT reactions involving alkenes, sulphides or alkenes, however, it could effect OAT of PPh_3 to $OPPh_3$. It was capable of cleaving the O-H bonds of 1-phenylethanol, DTBP and the N-H bond in 1,2-phenylhydrazine to yield acetophenone (22%), di-tert-butylquinone (50%, DTQ) and azobenzene (28%) respectively. Incorporation of an ^{18}O atom into DTQ was observed when $[Ni^{II}(nacnac)(O_2)]$ was generated with $^{18}O_2$, and so $[Ni^{II}(nacnac)(O_2)]$ was both involved in initial O-H cleavage and also OAT to the formed phenoxy radical. This was reflected in the yield of the DTQ (50 %), requiring two equivalents of the superoxide species, one as an O-H cleaving reagent (Fig. 7(a)), and a second to transfer an oxygen atom (Fig. 7(b)).[71] The formation of the quinone was assumed to form through a H-migration mechanism wherein an intermediate alkyl-peroxo species (Fig. 7(c)) formed and decayed to the quinone and a Ni^{II}-OH complex (Fig. 7(d), Path 1).

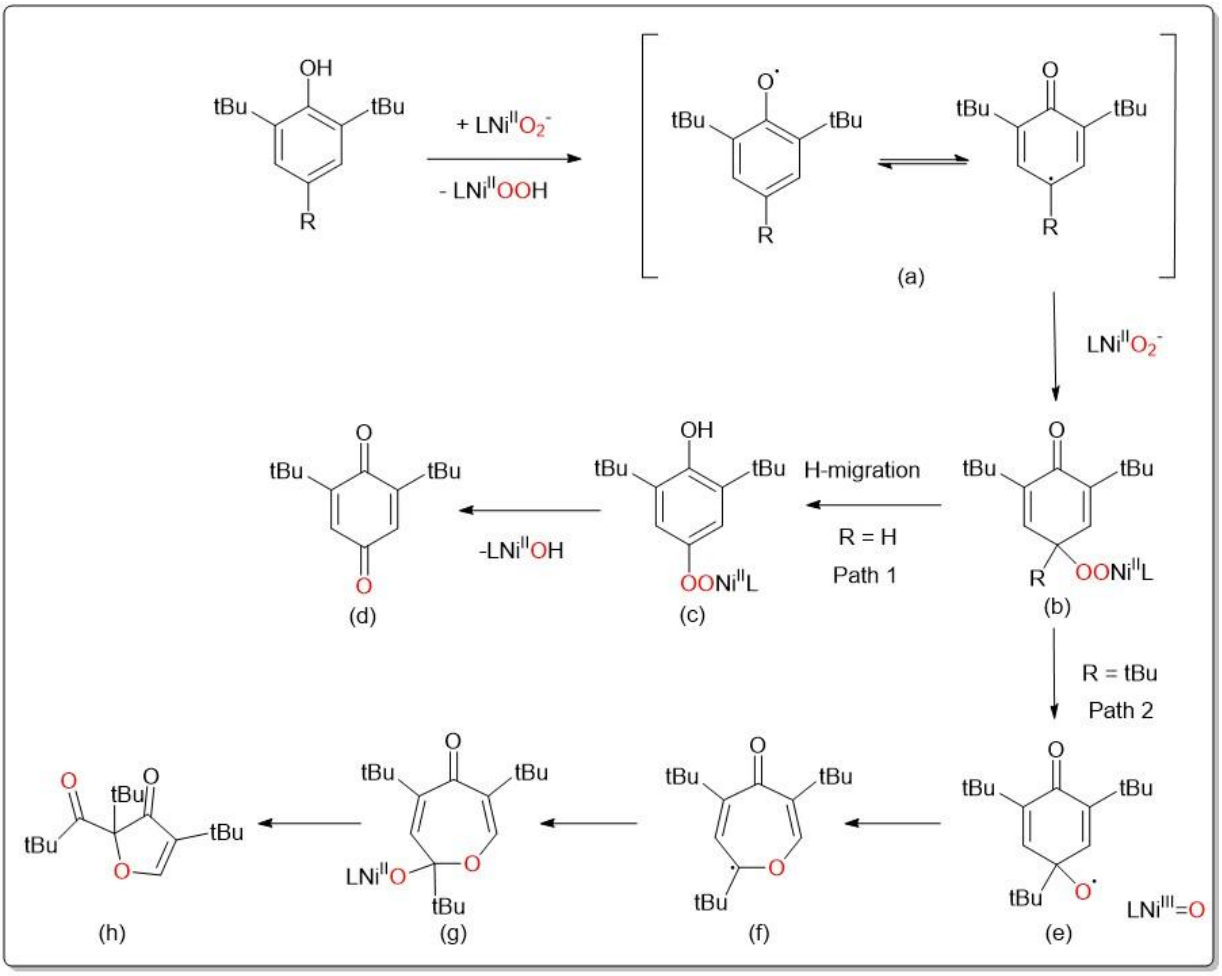

Figure 7. Proposed mechanism for the oxidation of DTBP (R = H) and TTTP (R = tBu) by [Ni^{II}(L)(O_2)] (L = nacnac). Adapted from ref [71]

The use of the para-substituted TTBP was expected to form a peroxy-para-quinol as the product.[71] Indeed, the reaction occurred with 40 % yield, and if done with the 2,4,6-tri-tert-butylphenoxy radical in 90 % yield, giving precedent for again the requirement of 2 eq. of the Ni^{II}-superoxide to effect the O-H cleavage followed by peroxide incorporation.[71] The product however, was in fact an acyclic ketone which had two atoms of oxygen, determined to be from the Ni^{II}-superoxide, incorporated into its structure (Fig. 7(h)), the Ni^{II}-superoxide acted as a dioxygenase. The key intermediate in the formation of the acyclic ketone was proposed to be a metal-aryl peroxo species (Fig. 7(b)) which led to an initial ring expansion (Fig. 7(f), Path 2) and formation of an Ni^{III}=O complex which then underwent radical rebound with the substrate (Fig. 7(g)) and eventual rearrangement yielded the final product (Fig. 7(h)). Precedent for the use of

Ni^{III}=O in the mechanism was previously proposed to be involved in the formation of $OPPh_3$ from PPh_3 with [Ni^{II}(nacnac)(O_2)].[38]

[Ni^{II}(nacnac)(O_2)] was also found to decay at room temperature to give a mass peak corresponding to a hydroxylated product (which shifted by two mass units when generated with $^{18}O_2$), which, followed by an acid workup, yielded the mass of the nacnac ligand plus an oxygen atom. In this way, it was proposed that the Ni^{II}-superoxide complex underwent self-hydroxylation on the ligand isopropyl groups.[71] This was reflective of the mechanisms of many of the previously mentioned enzymes which incorporate an electrophilic metal superoxide species, wherein an initial C-H cleavage step preceded the formation of a high valent metal-oxo adduct which then effected a second oxidation step.[10]

Thus, examples of synthetic metal-superoxide complexes are found throughout the literature and the means of characterising them as such oxidants are well understood. They are characterised by their ability to cleave C-H, O-H or N-H bonds of substrates or by their abilities to transfer an oxygen atom to a nucleophilic substrate such as PPh_3. This wealth of reactivity studies for electrophilic metal-superoxide complexes are a stark contrast to the three characterised nucleophilic metal-superoxide complexes.

1.4.2 Nucleophilic Metal Superoxide complexes

There are only three known synthetic metal-superoxide complexes which react as nucleophiles, [Cu^{II}(PyN_2^{iPr2})(O_2)]$^-$,[40,72] [Fe^{III}(TAML)(O_2)]$^{2-}$, [39] and [Ni^{II}(Bi^{iPr2})(O_2)]$^-$ (PyN_2^{iPr2} = N,N'-bis(2,6-diisoproylphenyl)-2,6-pyridinedicarboxamido, Bi^{iPr2} = diphenylisopropyl biuret).[41] The reactivity of Tolman's Cu^{II}-superoxide complex as a potential nucleophile was analysed by McDonald and co-workers due to its inability to react with substrates having weak C-H bonds and its ability to be readily protonated.[40,72] Addition of 10 eq. of benzoyl chloride caused the decay of the UV-vis features of [Cu^{II}(PyN_2^{iPr2})(O_2)]$^-$, at -80 °C in THF:DMF (3:1). ^{1}H NMR spectroscopy and GC-MS analysis identified benzoic acid as the product with a pseudo first-order rate constant (k_{obs}) which varied as a function of the concentration.[40] Plotting these k_{obs} values as a function of concentration yielded a second-order rate of constant (k_2) of 4.49 $M^{-1}s^{-1}$.

Typically, metal-peroxide complexes act as nucleophiles in the oxidation of aldehydes, wherein a plot of log($^Rk_2/^Hk_2$) versus the electrophilicity of the para substituent (σ_{p+}) yielded a linear Hammett plot with a positive slope (Hammett parameter, ρ), indicative of a nucleophilic mechanism.[37,73–75] It was assumed a similar process could be used for a nucleophilic metal-superoxide complex. For a series of para-substituted acyl chlorides, a slope of ~ 0 was obtained, suggesting that nucleophilic attack onto the electrophilic carbonyl group was not the RDS. Interestingly, the Cu^{II}-superoxide complex was found to not react with para-substituted benzaldehydes, as was common for nucleophilic metal-peroxide complexes, even though aldehydes are more electrophilic in nature than acyl chlorides. Instead, it was found that reaction was dependent on the degree of substitution at the α-carbon of the aldehyde, so that oxidation occurred for 3° (2-phenylpropionaldehyde (PPA), cyclohexane carboxaldehyde (CCA)), and quaternary α-carbons (trimethylacetaldehye (TMA)), but not for 1° (acetaldehyde (EtA)) or 2° α-carbons (Propanal (PrA)).[40]

Higher degrees of α-carbon substitution lead to a more electron rich α-carbon, thus the electrophilicity of the α-carbon was proposed to be involved in the RDS. The mechanism was proposed to follow a Baeyer-Villiger oxidation (Fig. 8 bottom), which occurred for some previously characterised metal-peroxide complexes, with a Criegee rearrangement for the aldehyde substrates, while Cl acted as a leaving group for the acyl chlorides (Fig. 8 top).[40] The Criegee rearrangement involved α-carbon attack onto the distal oxygen of the proposed Cu^{III}-alkylperoxide (electron transfer from Cu^{II} to superoxide after attack onto the carbonyl) which was the RDS, thus electron rich α-carbon aldehydes reacted more favourably due to the transient cationic nature of the intermediate α-carbon.[76]

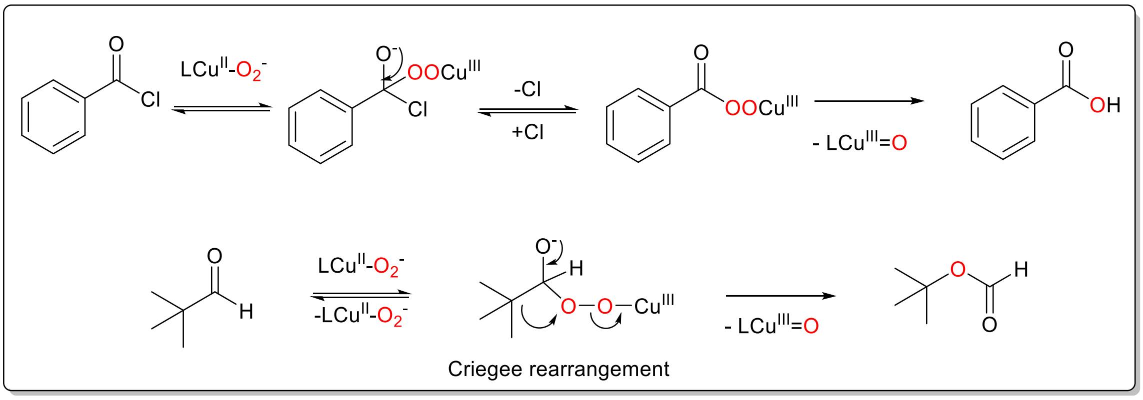

Figure 8. Proposed Baeyer Villiger oxidation of acyl chlorides (top) and aldehydes (bottom) by LCu^{II}-O$_2^{\bullet-}$ (L = N,N’-bis(2,6-diisoproylphenyl)-2,6-pyridinedicarboxamide). Adapted from ref[40]

Both Nam's $[Fe^{III}(TAML)(O_2)]^{2-}$ and Ray's $[Ni^{II}(Bi^{iPr2})(O_2)]^{-}$ reacted as nucleophilic oxidants with electrophilic aldehydes, and yielded Hammett plots with $\rho = 1.4$ and 0.44 respectively, providing evidence for rate determining nucleophilic attack onto the carbonyl groups.[39,41] $[Fe^{III}(TAML)(O_2)]^{2-}$ could also mimic metal-peroxide complexes which have been shown to transfer their peroxide groups to Mn-macrocycle complexes, reacting with $[Mn^{III}(TAML)]^{-}$ to irreversibly form the Mn^{IV}-peroxide complex $[Mn^{IV}(TAML)(O_2)]^{2-}$ and $[Fe^{III}(TAML)]^{-}$.[39] Interestingly, $[Fe^{III}(TAML)(O_2)]^{2-}$ was also capable of cleaving the O-H bond of DTBP, which was characterised by the product 2,2'-dihydroxy-3,3',5,5'-tetra-tert-butylbiphenol, the phenoxy radical coupling product, and $[Fe^{III}(TAML)]^{-}$.[39] To date it is the only known metal-superoxide complex which can act as both an electrophilic and nucleophilic oxidant. In contrast, $[Ni^{II}(Bi^{iPr2})(O_2)]$ did not undergo electrophilic HAT of the even weak C-H bonds of dihydroanthracene (DHA), but it did oxidise PPA, CCA and para-substituted benzaldehydes.[41]

Thus, this dearth of metal-superoxide complexes acting as nucleophilic oxidants are in stark contrast to that of the enzymatic studies mentioned previously. To date, no metal-superoxide complex has been isolated which can replicate the reactivity of the αKG-dependent enzymes wherein the nucleophilic attack onto a carbonyl group leads to the loss of CO_2 from an α-keto acid. This remains an important area for synthetic chemists to explore, as the spectroscopic evidence for this enzymatic mechanism has so far failed to have been revealed. More importantly, the properties which define a metal-superoxide complex as having the potential to act as a nucleophilic or electrophilic oxidant are still not understood.

1.5 X-ray Absorption Spectroscopy

X-ray absorption spectroscopy (XAS) is a spectroscopic technique which utilises X-rays to gain electronic and structural information of a given sample. It is a technique which has broad applications to fields such as chemistry, earth sciences, engineering, materials science as well as molecular and condensed matter physics. XAS is inherently useful for unstable intermediates such as those mentioned previously, which are only stable for short periods of time at cryogenic temperatures. XAS can be used to detail the structural and electronic symmetry of a flash frozen solution. It is most often used in conjunction with other experimental techniques such as EPR, UV-vis, Mössbauer and vibrational spectroscopies when single crystal XRD analysis is not possible. XAS differs from XRD as it does not require a crystalline sample, amorphous samples can be adequately studied.[77–81]Importantly, XAS can study a specific element in a given sample, as the technique involves the excitation of a core electron to either valence orbitals or complete ejection of the electron to the continuum. The energy of this differs to a relatively large extent between elements. However, if multiple elements of the same type are present, an average reading of the two (or more) elements is given.[79,81–83]

1.5.1 General Background

XAS is a broad term which is used to generalise the two main experiments carried out, X-ray absorption near edge spectroscopy (XANES) and extended X-ray absorption fine structure (EXAFS) analysis. While having similar data collection techniques, the two experiments focus on separate areas of the output spectrum. XANES gives data on the electronic symmetry of an element, from which the oxidation state can be obtained, while structural information such as neighbouring atom distances and the assignment of neighbouring atoms is garnered from EXAFS. The method of XAS collection involves; the generation of a sufficient X-ray flux within a sufficient energy range, tuning this energy with a monochromator for a specific element, and using a detector to measure the outgoing (transmission) or generated (fluorescence) X-rays from the sample of interest.[79,81]

XAS is an inherently insensitive technique, requiring a highly concentrated X-ray beam to allow the collection of sufficient data for analysis. Due to this, XAS must be carried out at synchrotron radiation facilities. Synchrotron facilities incorporate either a linear or circular particle accelerator which, as well as potential storage rings and undulators/wigglers, combine to produce high flux X-rays.[81] The emitted X-rays are often of a wide range (2 – 30 keV) (keV = kilo electron volts) and thus must be focused to specific frequencies for the desired sample.

Monochromators are used to tune the frequency of the X-ray beam. They utilise Bragg's reflection from two parallel Si single crystals to tune the energy. This is done by changing the angle of incidence (θ) of the electron beam and the Bragg lattice plane of the crystal.[79] In this way, the wavelength of light incident on the sample (λ) is dependent on θ by equation (3) below:

$$n\lambda = 2d\sin\theta \qquad (3)$$

where n is the order of reflection and d is the lattice spacing.

Once the X-ray beam has been generated and the energy/frequency tuned, it becomes incident on the sample. There are two methods of data detection; transmission or fluorescence detection.[79,81] Transmission detection is most common and incorporates ionization chambers as the detectors. These ionisation chambers are gas-filled devices of which gas particles become excited by the incident X-ray, to which a voltage is applied to generate a current. Changes to the ionisation of the gas molecules leads to a change in the necessary applied voltage.[81] In transmission detection, the ratio of the X-ray incident on a reference sample (I_0) and the transmitted X-rays after passing through the sample (I_1) gives the corresponding absorption coefficient which is used to generate the output spectrum.[81]

Fluorescence detection is most commonly used for dilute samples, such as those used in biomimetic model complexes. Fluorescent detectors measure X-ray radiation emitted from the sample and are placed at a 90° angle to the X-ray beam. This 90° angle is used to inhibit the incident X-rays which are scattered from the sample, which is at a minimum at 90°. Contrastingly, fluorescence X-rays are emitted isotropically from the sample so their measurement are not affected.[81] Transition metal fluorescence detectors incorporate a filter using an element with an atomic number which is one below the measured sample (Z - 1 filter). This ensures that X-rays emitted from the sample are not absorbed by the filter, but that reflected incident X-rays are.[81]

1.5.2 X-ray Absorption Near Edge Spectroscopy

As previously mentioned, XAS is a general term for both XANES and EXAFS. A typical XAS spectrum is shown in Figure 9 and it is divided into two regions, the XANES which encompasses the pre-edge and the edge regions, and the EXAFS, which occurs after the maximum absorbance of the rising edge. The “edge” refers to the sharp rise seen in the XANES spectrum and is due to an absorption of X-ray energy due to excitation of a 1s electron into the continuum. The pre-edge refers to any processes, such as the excitation of a 1s electron to a valence d or p orbital, which occur before the rising edge.[77–82] Knowledge of XANES in these regions allow the assignment of oxidation state, while also giving information regarding the electronic symmetry of the metal site of the sample. Importantly, comparison of two samples which differ by one or more electrons allow changes therein to be determined, the primary use of XANES for bioinorganic samples by comparison of their edge energies (discussed below).

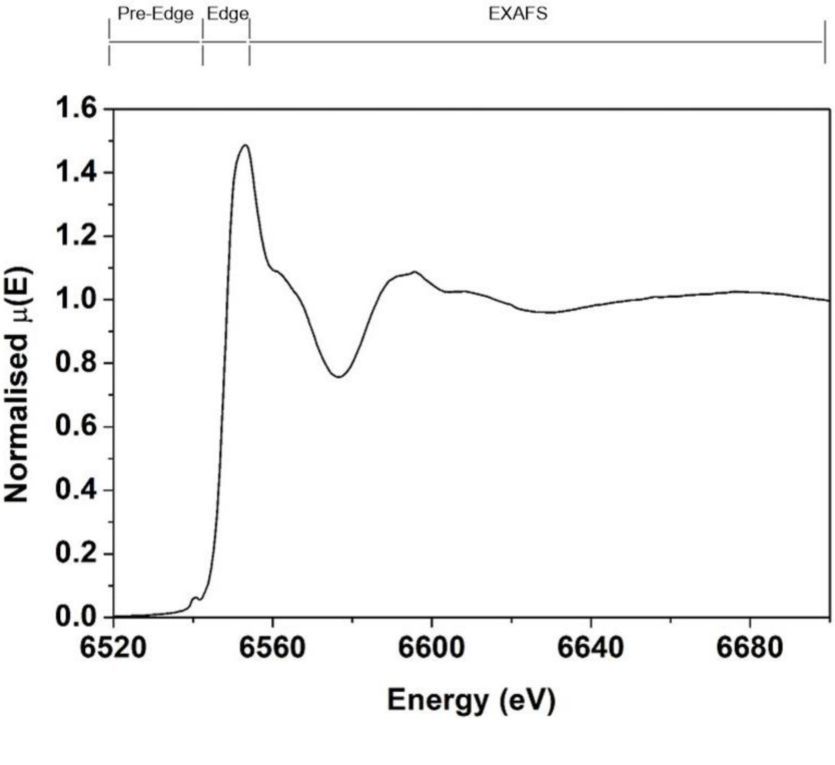

Figure 9. XAS spectrum highlighting the different regions of the data output

When enough energy is provided to the metal site of interest, ejection of an inner sphere electron occurs and leads to a sharp rise in the XANES spectrum. For a given metal, there exists a number of possible “edges” which can be measured, over a variety of energies. These edges refer to the core orbital from which the electron is ejected from. Most commonly for first row transition metals, the K-edge is investigated in an XAS experiment, which corresponds to excitation of a 1s electron. However, other edges, such as L_1, L_2, which correspond to the 2s and 2p orbitals respectively, also can be measured. However, they are at very low energies for first row transition metals. These lower energy transitions are often used for metals in the third row, as the K-edge energies are too high to be reached by synchatron radiation.[79]

The "edge" energy of a metal is defined as the first inflection point of the rising edge and is most commonly used to identify the oxidation state of transition metals.[77–82] The edge energy is effectively the ionisation energy of the metal in the sample. However, it must be noted that there are exceptions to this definition, as in the case of copper, as core to valence excitations can occur within the energy range of the rising edge which lead to distortions of the edge energy. This therefore distorts the positioning of the first inflection point. For metals such as copper, other defining features are used to detail the oxidation state of the metal.[84] Importantly, the edge energy of a metal is specific. Within this, the oxidation state for a specific metal also has a known range of energies. Thus, the main characteristic which is obtained from the edge energy in transition metal complexes is that of the oxidation state of the metal of interest.[79,80]

The pre-edge of the XANES spectrum corresponds to any features in the region prior to the rising edge. This region incorporates weak absorption features arising from the excitation of a core electron to an unfilled valence orbital. The most common excitation for K-edge spectra of first row transition metals are 1s → 3d transitions, but 1s → 4p transitions can also occur.[79] Pre-edge energies, the energy corresponding to the maximum of the pre-edge absorption band, can be used to define the oxidation state of a metal in some cases. For example, pre-edge energies for the 1s → 3d transition shift by up to 2 eV for Cu between the Cu^{II} and Cu^{III} states. Importantly, there is no 1s → 3d pre-edge feature for Cu^{I}, as it is a d^{10} species.[83,84] However, in other metals, such as Mn, no appreciable energy change is observed in the 1s → 3d pre-edge until the higher oxidation states of Mn^{IV} and Mn^{V}, Mn^{II} and Mn^{III} states generally have identical pre-edge energies.[85]

The pre-edge features are also an indication of the metal-site symmetry, due to mixing of the contributing orbitals, a 1s → 3d transition is more allowed in a tetrahedral geometry than compared to a square pyramidal geometry by selection rules. Thus, the area of the pre-edge and its intensity can be correlated to a change in electronic symmetry when comparing two samples.[79] However, it must be noted that changes in the oxidation state of a metal can also play a role in the pre-edge area and thus must be accounted for when comparing pre-edge areas.

Taken together, the edge and pre-edge features in the XANES spectrum can be used to identify the oxidation state of the metal as well as to compare changes in the electronic symmetry between two similar species.

1.5.3 X-ray Absorption Fine Structure Analysis

Beyond the rising edge absorbance maximum lies the EXAFS region of the XAS spectrum. EXAFS yields information regarding the coordination environment, the identity of the neighbouring atoms and their distances from the absorbing nucleus, that which is the target of the X-ray beam. Information from the EXAFS region can only be obtained by fitting of model data to that obtained.[78–81]

In the EXAFS region, the electron has been ejected from the metal and thus the energy corresponds to above that of the ionisation energy. This excess energy is explained by the interaction of the ejected electron with the immediately surrounding nuclei.[79,81] Proof for the interaction of the ejected electron with the surrounding nuclei comes from analysis of monoatomic gas molecules, such as argon, by EXAFS analysis, which show no EXAFS features.[79] However, for any diatomic or multiatomic species, the EXAFS region of the XAS spectrum can be seen as being of a similar shape as in Figure 9.[79,81] The atoms which the ejected electron interacts with are referred to as the backscattering atoms and they interact with the photoelectron in alternating constructive and destructive waves. In the most simplistic view of EXAFS, the ejected photoelectron interacts with each neighbouring nuclei to produce data in the form of sine waves which are transformed by Fourier analysis to yield the final EXAFS spectrum.

The sine wave obtained from each photoelectron-scatterer interaction has three observable features; frequency, amplitude and phase. The frequency of the sine wave is related to the distance of the ejected electron to the scattering atom, the amplitude to the number of identical scatterers at a set distance (as two identical scatterers produce identical sine waves which are summated) and the phase, positive or negative interference, is a function of both the absorbing and scattering atom.[79] Importantly, heavier atoms scatter the sine waves more effectively which allow their identification quite easily after Fourier transformation of the data. This is most important for metal clusters and multi-metal complexes which are separated by bridging species where a characteristic, large absorption peak is seen at the corresponding distance in the Fourier transformed spectrum.

This description has dealt with the simple explanation of single-scattering, where the scattering event of the ejected electron has been done by a single backscatterer, which can be modelled quite well. However, multi-scattering events can also occur, scattering by a number of atoms, which are much more difficult to model and are often avoided in the treatment of the EXAFS model.[79]

In combination, XANES and EXAFS allows the identification of the oxidation state of the metal, the electronic symmetry as well as the identity and bond distances to neighbouring atoms.

1.6 Aims

The aims of this project were to synthesise metal-superoxide complexes supported by the $H_2PyN_2^{iPr2}$ ligand framework. For the basis of this project, it was chosen to focus primarily on Ni and Fe as the metals of interest. These metals are biologically relevant, and examples of synthetic superoxide complexes thereof are known. Also, the corresponding Cu^{II}-superoxide complex of this ligand system has been previously characterised, and its reactivity has been thoroughly investigated. Thus, the ultimate goal was to gain an understanding of how the stability and reactivity of the metal-superoxide complex changes as the number of d-electrons change.[40,72] Initially, synthesis and characterisation of the Ni^{II} and Fe^{II} precursor complexes supported by the pyridine dicarboxamide ligand would be carried out, with the Fe^{II} based complexes being synthesised under an inert atmosphere due to the propensity of Fe^{II} and low coordinate Fe complexes to react with atmospheric oxygen.

Once these complexes had been formed and suitably characterised, they would be reacted with KO_2 or O_2 at sub-millimolar levels at temperatures ranging from room temperature to cryogenic temperatures. It is expected that potential superoxide complexes will be highly unstable, due to, as previously mentioned, their inherent thermal instabilities. Changes in the electronic absorption bands would be monitored and the conditions which maximise the yield of potential intermediates would be determined. These metastable species would be probed by various spectroscopies (UV-vis, vibrational, NMR, EPR and XAS spectroscopies). Once the intermediates have been characterised, their reactivity will be studied with a variety of organic substrates in potential electrophilic and nucleophilic oxidation reactions. A thorough kinetic investigation into the rates of potential reactivity with organic substrates will allow determination of the reaction mechanisms. If potential reactive intermediates do form but their reactivity is too high as to allow isolation, their existence will be inferred through the decay products of the reaction, through intramolecular oxidation of the ligand, or through potentially oxidised solvent molecules.

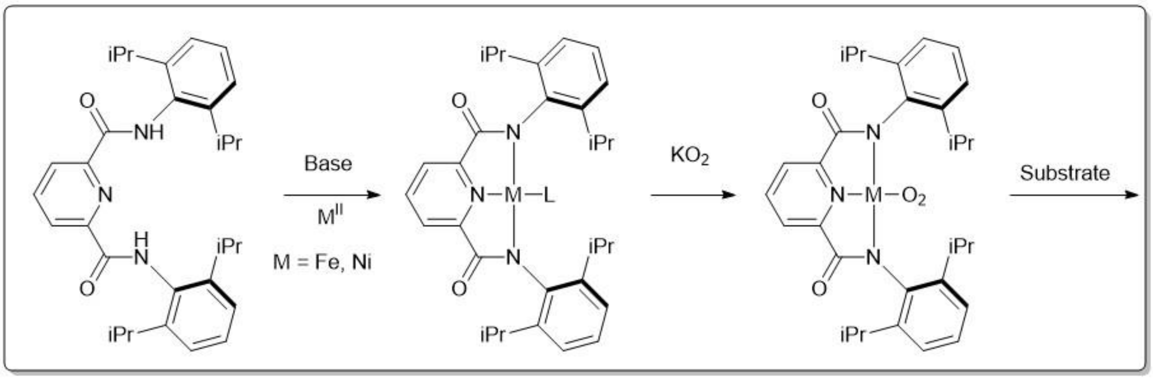

Scheme 2. Graphical Aims

2 Results and Discussion

2.1 Synthesis

2.1.1 Ligand Synthesis

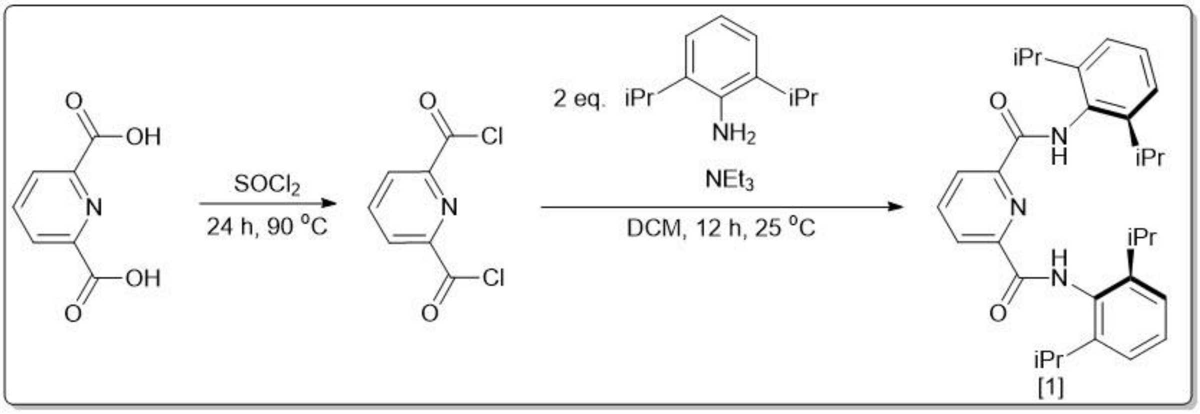

Scheme 3. Synthesis of **1**

The synthesis of $H_2PyN_2^{iPr2}$ (**1**) was carried out by a reported procedure,[86] by the reaction of 2,6-pyridinedicarboxylic acid chloride and 2 equivalents of 2,6-diisopropylaniline in the presence of triethylamine (NEt_3) (Scheme 3). 2,6-pyridinedicarboxylic acid chloride was synthesised by the chlorination of 2,6-pyridinedicarboxylic acid by thionyl chloride ($SOCl_2$).

2.1.2 [Ni^{II}(PyN$_2$^{iPr2})(NCMe)] synthesis

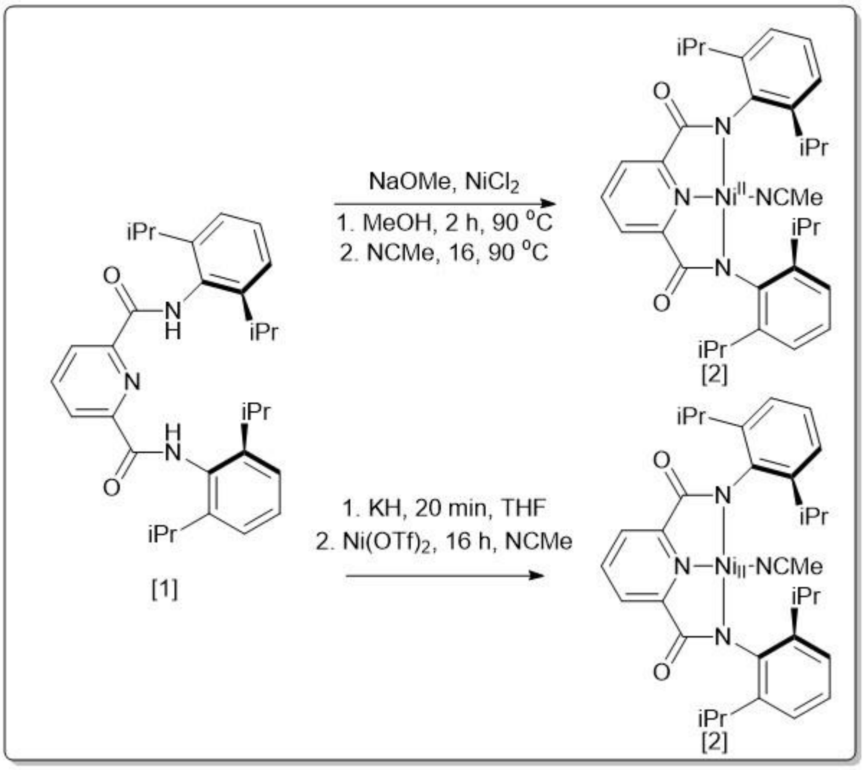

Scheme 4. Synthesis of **2** via NaOMe/NiCl$_2$ (top) and KH/Ni(OTf)$_2$ (bottom)

The synthesis of [Ni^{II}(PyN$_2$^{iPr2})(NCMe)] (**2**) could be carried by one of two reported procedures (Scheme 4).[87,88] The first route involved the reaction of **1** with NiCl$_2$ in MeOH in the presence of NaOMe. Introduction of NCMe and subsequent reflux yielded **2** after subsequent filtration, drying and recrystallisation from DCM/Et$_2$O as a red crystalline product which was previously reported as a square planar Ni^{II} complex.[88]

Alternatively, **2** could be synthesised by the initial deprotonation of **1** with KH in THF, followed by the addition of Ni(OTf)$_2$ and then NCMe.[88]

2.1.3 Synthesis and Characterisation of $K_2[Fe^{II}_2(PyN_2^{iPr2})_2(bis\text{-}\mu\text{-}OH)_2]$

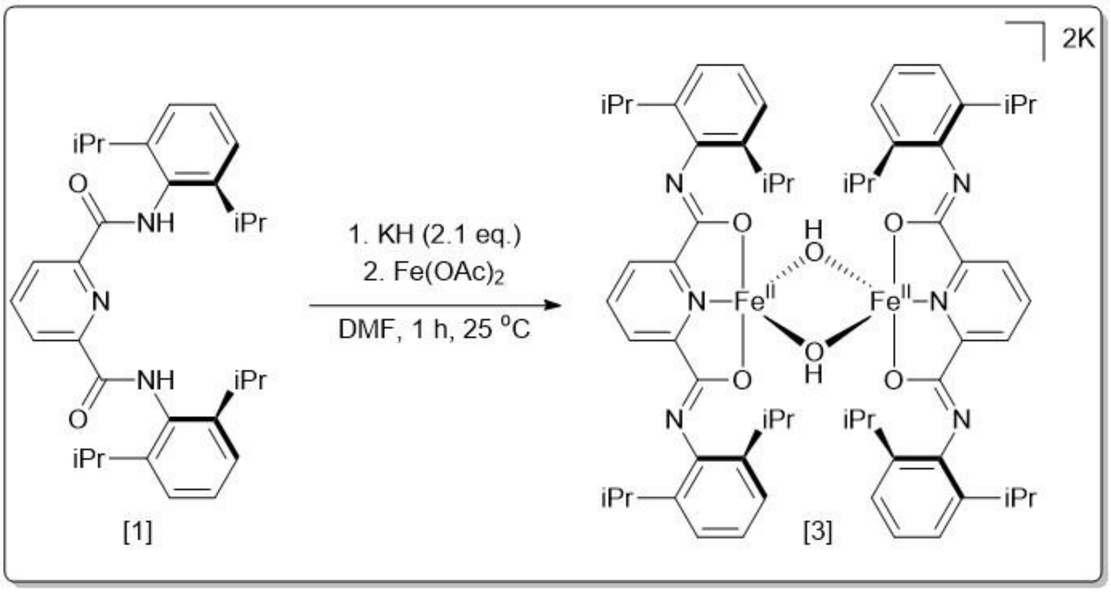

Scheme 5. Synthesis of **3**

The bis-μ-hydroxide complex, $K_2[Fe^{II}_2(PyN_2^{iPr2})_2(bis\text{-}\mu\text{-}OH)_2]$ (**3**), was synthesised under an inert atmosphere by deprotonation of **1** with two equivalents of KH in DMF followed by the addition of $Fe^{II}(OAc)_2$ to form a dark blue solution which changed to a dark purple colour over 2 - 3 minutes (Scheme 5). The hydroxide moiety was proposed to form due to the presence of adventitious water in the solvent. Subsequent filtration and recrystallisation by layering with ether yielded a dark red crystalline solid which was suitable for single crystal XRD.

The crystal structure of **3** (Fig. 10) showed the complex to be a binuclear bis-μ-hydroxide Fe^{II}_2 complex. The asymmetric unit was composed of $[Fe_2(PyN_2^{iPr2})_2(bis\text{-}\mu\text{-}OH)_2]^{2-}$, two K^+ ions and two disordered DMF moieties. The structure was constituted from two disordered $[Fe_2(PyN_2^{iPr2})_2(bis\text{-}\mu\text{-}OH)_2]^{2-}$ units, wherein the distortion was centred only around the isopropyl groups of the ligand backbone and the solvent residues. Critical parameters are displayed in Table 5.

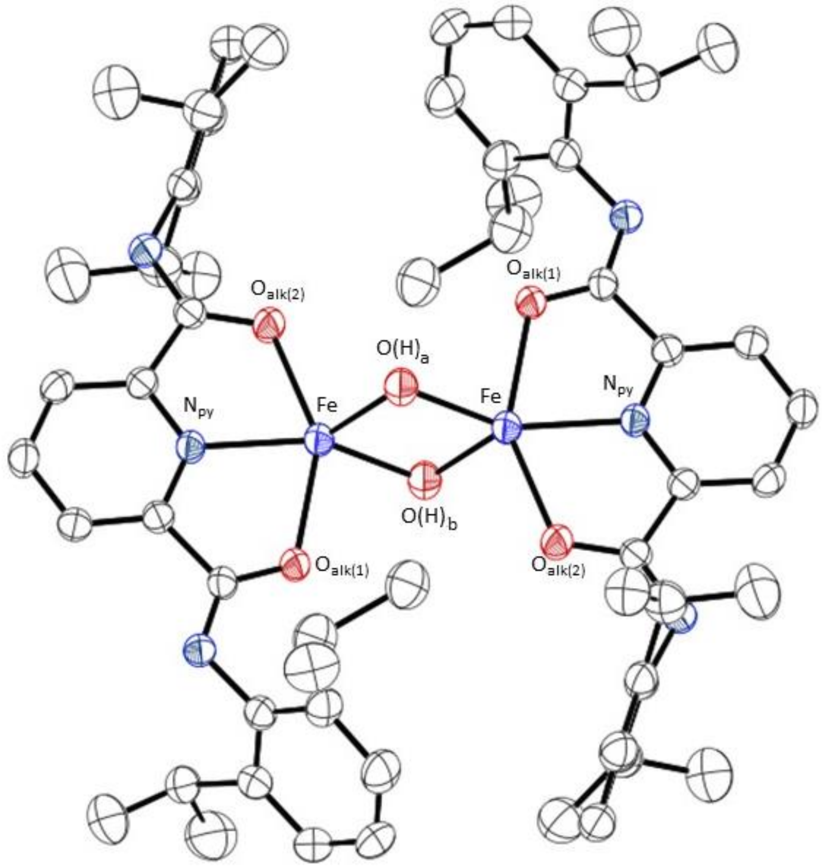

Figure 10. Molecular structure of $[Fe^{II}_2(PyN_2^{iPr2})_2(bis\text{-}\mu\text{-}OH)_2]^{2-}$. Potassium ions, hydrogen atoms and solvent molecules are omitted for clarity. Only one of the disordered units is shown for clarity. Thermal ellipsoids are shown at 50% probability.

Table 5. Selected structural parameters for **3**

Bond	Distance (Å)		Angles (°)
Fe-N_{py}	2.111(3)	$O(H)_1$-Fe-N_{py}	151.76(10)
Fe-$O_{alk(1)}$	2.155(2)	$O_{alk(1)}$-Fe-$O_{alk(2)}$	146.84(9)
Fe1-$O_{alk(2)}$	2.137(2)		
Fe1-O(H)a	2.015(2)		
Fe1-O(H)b	2.041(2)		
Fe•••Fe	3.064 (2)		

Each iron centre was penta-coordinate in the molecular structure. Coordination of the ligand was through the oxygen moieties, as well as the pyridine nitrogen. Coordination of the ligand in this isomeric form, resulted in a change in the bond order of the ligand’s amide-centred bonds. This was most evident in the C=N and C-O bonds of the complex (previously C-N and C=O bonds of the ligand). For **3** the average C=N bond length of the bound ligand was 1.290(6) Å while the average C-O bond length was 1.297(6) Å. These bond lengths were in contrast to the previously characterised complexes **2** and [Cu^{II}(PyN$_2$^{iPr2})(NCMe)], both coordinated at the amidic nitrogen positions, which had average C-N bond lengths of 1.346(4) and 1.338(4) Å and average C=O bond lengths of 1.236(3) and 1.234(3) Å respectively.[88,89] The average C-O bond distance of **3** compared well with other Fe complexes with similar ligands, having C-O bond lengths between 1.25 – 1.30 Å, while the C=N bond length were in the range of 1.31 – 1.34 Å, ~ 0.02 Å larger than for **3**. From the structure of the complex, as well as the detailed bond lengths of the ligand, it was concluded that the ligand had undergone significant electronic rearrangement.

This coordination mode was atypical for complexes of the form [M(PyN$_2$^{iPr2})(X)] (X = Cl, F, Br, I, OH, OCH$_3$, OCO$_2$H, O$_2$CCMe, ONO$_2$, OPh bipyridine, terpyridine, acetylacetone, M = Cu, Ni), which were coordinated via the amidic nitrogens.[72,89–97] Two examples of penta-coordinated Fe^{III} complexes bearing the pyridine dicarboxamide ligand family are known, [Fe^{III}(PyN$_2$$^{R,R'}$) (R = Ph, R' = Ph^{S}, Ph^{SO2}).[98] In both cases, coordination of the pyridine dicarboxamide ligand was via the amidic nitrogens. For complexes of the form [Fe^{III}(PyN$_2$^{R2})$_2$]$^{1+}$ (R = Ph, Ph^{SMe}, Ph^{OMe}), wherein two pyridine dicarboxamide ligands were bound to one Fe^{III} centre, coordination via the amidic nitrogens was also reported.[99,100] No reported structures of Fe^{II} complexes or of dinuclear Fe$_2$ complexes bearing a pyridine dicarboxamide ligand have been reported to date. The ruthenium complexes, [Ru^{II}(PyN$_2$^{R2})(PPh$_3$)$_2$(DMF)] (R = naphthalene) and [Ru^{II}(PyN$_2$^{iPr2})(PPh$_3$)(CHPh)] are the only examples of compounds bearing this family of pyridine dicarboxamide ligands bound via the oxygen atoms.[95,101] [Ru^{II}(PyN$_2$^{iPr2})(PCy$_3$)(CHPh)] has also been reported to have a structure wherein the pyridine dicarboxamide ligand was bound via one amidic nitrogen and one alkoxide oxygen. Thus, **3** represented both the first non-ruthenium complex, as well as the first dinuclear compound, bearing the pyridine dicarboxamide ligand coordinated in this isomeric form.

The Fe$^{II}_2$(OH)$_2$ core was asymmetric regarding hydroxide coordination to the iron centres with Fe-O(H) bond lengths of 2.015(2) and 2.041(2) Å which agreed well with previously reported complexes bearing a Fe^{II}(OH)$_2$ core.[102–107] The Fe•••Fe distance of 3.064(2) Å was typical of such dimeric Fe$^{II}_2$(OH)$_2$ cores which vary between 3.0 – 3.1 Å.[102–107] The

τ_5 value of the metal centres gave an insight into the degree of distortion from an idealised geometry, a value of 0 equating to a perfect square pyramidal geometry and a value of 1 indicating a perfect trigonal bipyramidal geometry.[108] The τ_5 value was calculated from equation 4 below where $\beta > \alpha$, the two largest valence angles of the iron core.

$$\tau_5 = \frac{\beta - \alpha}{60°} \qquad (4)$$

The τ_5 value of the iron core, 0.082(3), indicated that the iron centres were best described as distorted square pyramids. Interestingly, it was observed that the phenyl rings were asymmetric. This was due to the interaction of one aromatic ring with a potassium ion, situated in a pocket between the aromatic rings and one bridging hydroxide. This was easily seen by the contrasting distances between the centroid of the aromatic rings and the potassium ion, 3.3306(2) and 4.3166(2) Å, and the angle between the aromatic plane and the potassium-centroid line, 15.460° and 37.140°. This asymmetry was most likely due to the steric bulk of the aromatic rings preventing the coordination of both rings to the potassium ion.

^{1}H NMR spectroscopy yielded a spectrum with line broadening and large chemical shifts, consistent with the paramagnetic nature of the complex. Approximately 17 uniquely paramagnetic signals present between -30 – 100 ppm (Figure 11) were observed. Signals corresponding to the $H_2PyN_2^{iPr2}$ ligand were found in the diamagnetic region suggesting that the reaction had not gone to completion or that the complex had partially decayed in solution. Assuming symmetry through the $Fe^{II}_2(OH)_2$ core, a maximum of 9 signals, assuming the methine iPr protons were inequivalent, would be expected, 7 ligand-based signals and 2 for the distinct OH moieties. Thus, from the number of signals observed, it was likely that the ^{1}H NMR spectrum was a result of more than one complex in solution. The dimeric complex seen in the solid state has been suggested to be in equilibrium with a monomeric structure in solution. The IR spectrum of **3** importantly showed the loss of the amidic proton residues present at 3300 cm^{-1} of **1** (Fig. S1). Direct injection ESI-MS showed the major mass peak at m/z = 629.2790, which matched that of the monoanion $[[Fe^{II}(PyN_2^{iPr2})(OH)] + DMF]^-$ (calc. = 629.2791, Fig. S2).

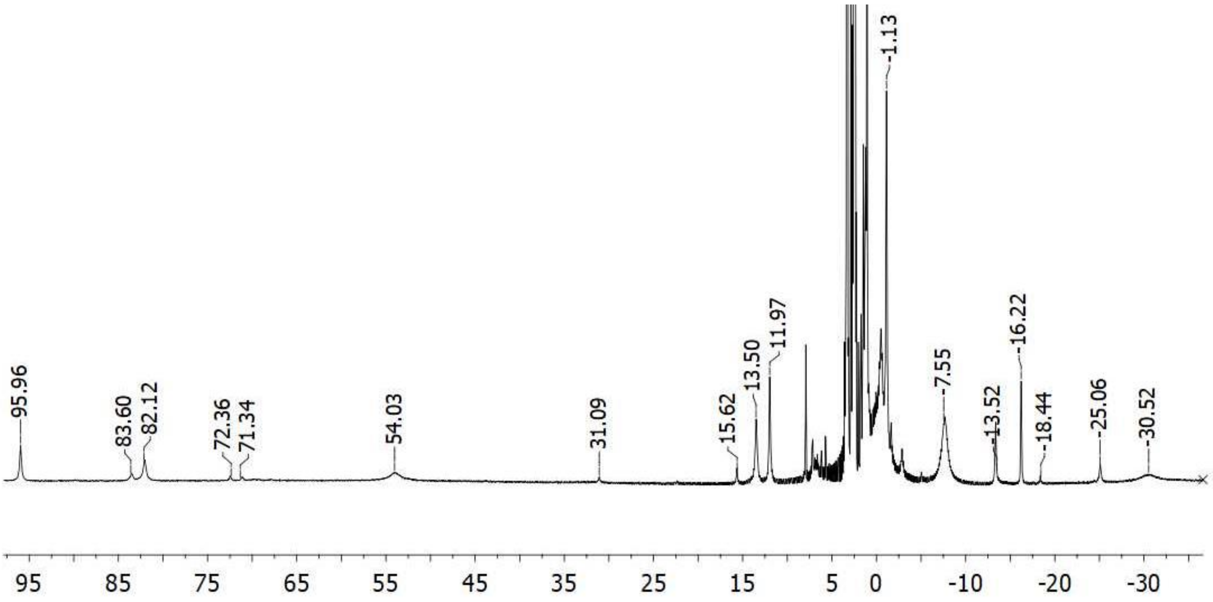

Figure 11. ^{1}H NMR spectrum **3** in DMSO-D_6. Peaks at 7.95 (DMF), 3.3 (H_2O) and 2.5 (DMSO) are solvent peaks.

Thus, **3** was characterised as a dimeric $Fe_2^{II}(OH)_2$ complex. Although the synthesis of a monomeric square planar Fe^{II} complex was not successful, **3** was found to be the first $Fe_2^{II}(OH)_2$ complex, synthesised with an amidic ligand, which was bound via the oxygen atoms, rather than the nitrogen atoms, of this ligand family.

2.1.4 Synthesis and characterisation of [Fe^{II}(PyN$_2^{iPr2}$)(DMF)]

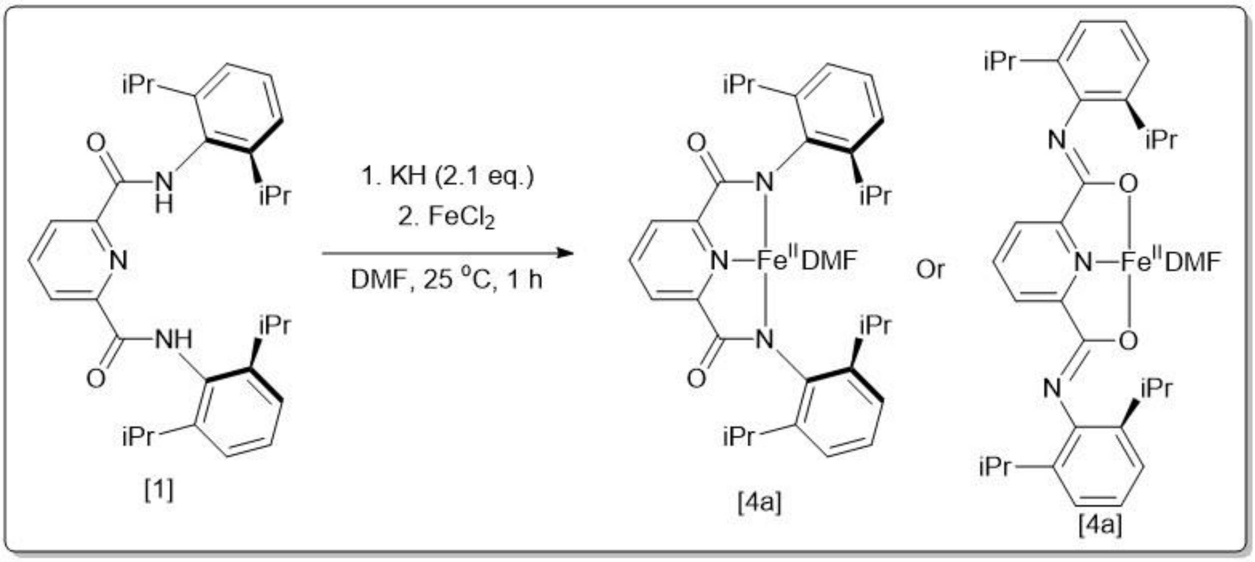

Scheme 6. Synthesis of **4a**

To avoid the formation of **3**, **1** was deprotonated using KH and reacted with $FeCl_2$ in an attempt to synthesise a monomeric Fe^{II} complex. **1** was deprotonated with 2.1 eq. KH in DMF, to which 1 eq. $FeCl_2$ was added to yield a dark purple coloured solution which changed to a wine-red colour after 2 - 3 minutes (Scheme 6). Subsequent filtration and layering with Et_2O yielded a dark purple solid. Interestingly, attempts to dissolve the formed purple solid in THF, NCMe, $CHCl_3$, DCM or acetone yielded a yellow solution, which was inferred to be a decay product. Dissolution in DMSO yielded a purple solution.

Direct injection positive mode ESI-MS of a DMSO solution yielded a spectrum with three mass peak at m/z = 524.2666, 656.1992 and 1009.5806 (Fig. S3). These peaks were assigned as the mono-cations $[H_2PyN_2^{iPr2} + K]^+$ (calc. m/z = 524.2679) $[[Fe^{II}(PyN_2^{iPr2})(DMSO)] + K]^+$ (calc. m/z = 656.2012, Figure S3) and $[K(PyN_2^{iPr2})_2]^+$ (calc. m/z = 1009.5722) respectively. From the ESI-MS results, it was assumed that complex in solution was $[Fe^{II}(PyN_2^{iPr2})(DMSO)]$ (**4b**), wherein the DMF residue of $[Fe^{II}(PyN_2^{iPr2})(DMF)]$ (**4a**) was substituted when dissolved in DMSO. This matched the observation of the complex being red in DMF, but purple in DMSO, due to differences in solvent coordination. ^1H NMR spectroscopy yielded a spectrum with 10 paramagnetically shifted signals in the range of -25 to 92 ppm (Figure 12). Assuming a monomeric complex as in Scheme 6, 7 of these proton peaks would correspond to ligand-based protons while the remaining three would correspond to the DMF protons. Signals present between 0-11 ppm correspond to solvent peaks (DMSO = 2.5 ppm) and minor traces of **1** which were assumed to have formed due to minor decay of the sample prior to examination. Evan's method yielded a $\mu_{eff} = 3.44$ which was suggestive of an S = 1 electronic ground state ($\mu_{SO} = 2.83$ for 2 electrons). This supported the assignment of the complex as a square planar d^6 ion with two unpaired electrons. Importantly IR showed the loss of the characteristic N-H stretch at 3300 cm^{-1} from **1** (Fig. S4) The UV-vis spectrum of **4a** in DMSO showed a single peak centred at 525 nm ($\varepsilon = 650\ M^{-1}cm^{-1}$, Fig. S5).

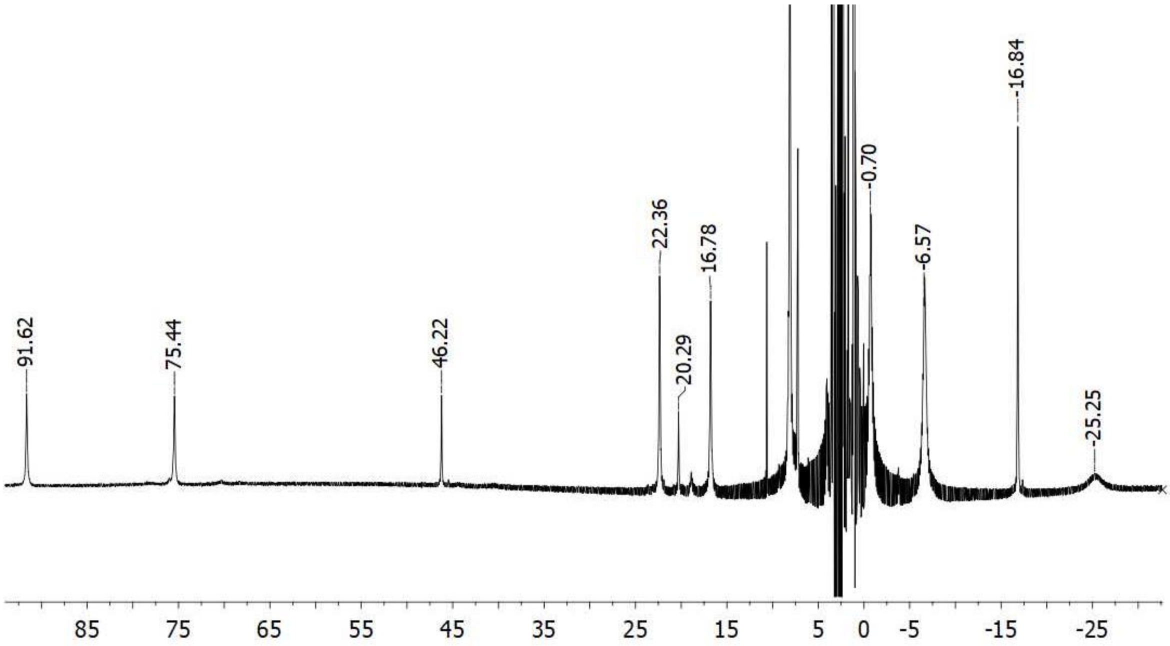

Figure 12. ^{1}H NMR spectrum of **4a** in DMSO-D_6

Thus, the complex **4a** was synthesised and characterised by ^{1}H NMR and IR spectroscopies as well as ESI-MS. Attempts at formation of crystals suitable for XRD were unsuccessful with solutions of DMF or DMSO layered with Et_2O, toluene and hexane, as well as by vapour diffusion with the same solvent systems. Further work should be done in order to determine if the binding mode of the ligand is similar to that of **3**. Fe^{II} compounds **3** and **4a** were reactive towards O_2 (as in equation (1)) and their reactivities are the subject of future studies.

2.2 Nickel and superoxide

2.2.1 Initial UV-vis studies

The reaction of the **2** was investigated towards reaction with KO_2, in an attempt to synthesise a Ni^{II}-superoxide complex based on equation (2). The approach that was taken involved the dissolution of **2** (0.125) in a variety of solvents (THF, DMF, NCMe) followed by the addition of a small volume (100 µL) of a solution of KO_2 (10 mM) and 18-C-6 (20 mM) dissolved in DMF (5 mL).[39] These reactions were done on a UV-vis spectrophotometer at 25 °C.

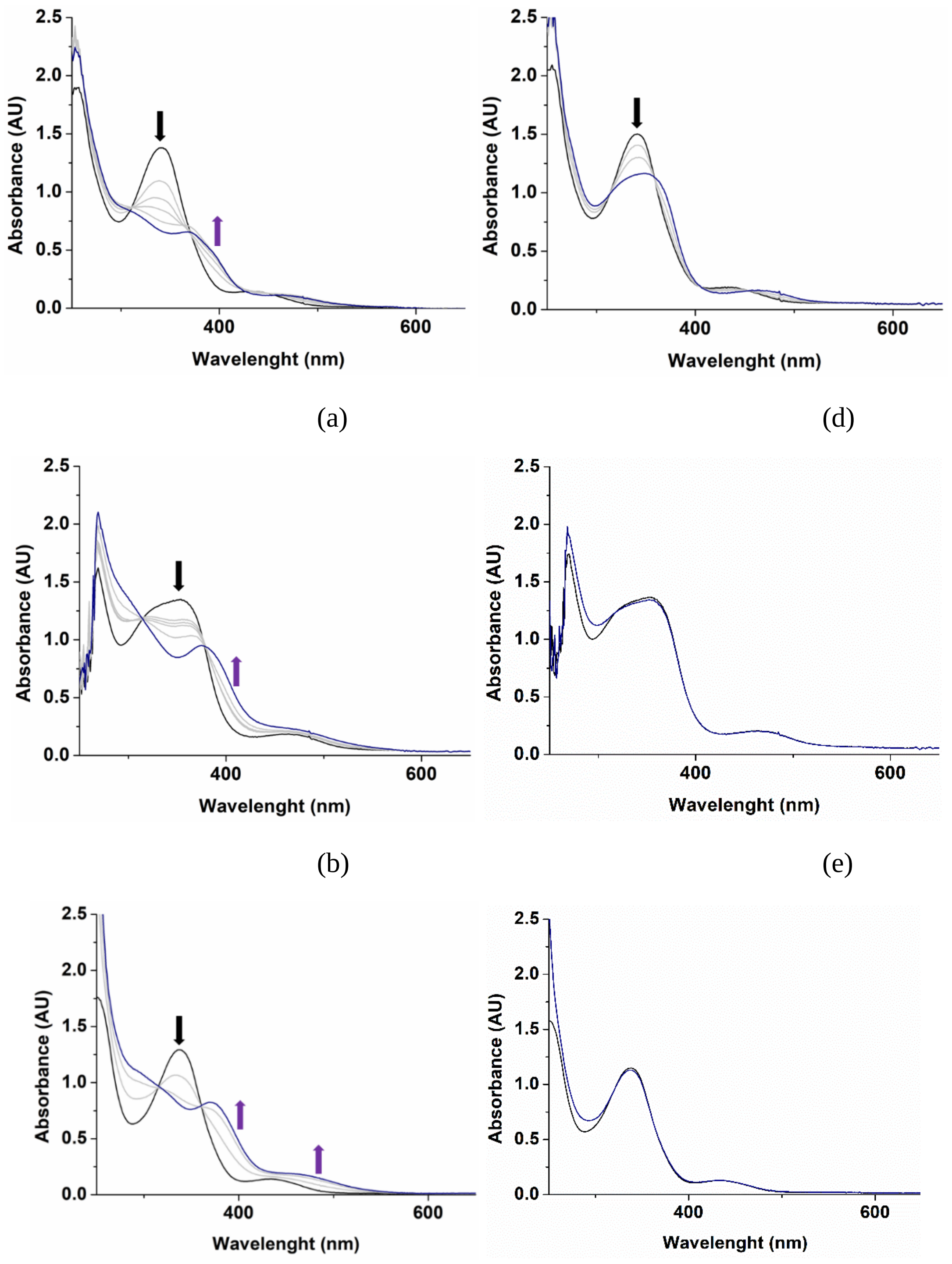

(a) (d)

(b) (e)

(c) (f)

Figure 13. Addition of 100 μL of KO_2 (10 mM) and 18-C-6 (20 mM in DMF) to a 0.125 mM solution of **2** dissolved in THF (a), DMF (b) and NCMe (c) or the addition of 18-C-6 (20 mM in DMF) to a 0.125 mM solution of **2** dissolved in THF (d), DMF (e) and NCMe (f). Black traces correspond to the starting spectra, grey traces to intermediate spectra and dark blue traces to the final spectra obtained after 150 s.

Dissolution of **2** in THF, DMF or NCMe yielded the black absorbance traces seen in Figure 13 (a (THF), b (DMF), c (NCMe)) with UV-vis absorption features at $\lambda_{max(a)}$ = 340 (ε = 10300 $M^{-1}cm^{-1}$), 440 (ε = 1100 $M^{-1}cm^{-1}$) nm, $\lambda_{max(b)}$ = 330 (sh, ε = 10100 $M^{-1}cm^{-1}$), 355 (ε = 10700 $M^{-1}cm^{-1}$), 460 (ε = 1500 $M^{-1}cm^{-1}$) nm, $\lambda_{max(c)}$ = 340 (ε = 12000 $M^{-1}cm^{-1}$), 440 (ε = 1500 $M^{-1}cm^{-1}$) nm respectively. The UV-vis features of **2** in THF and NCMe appeared identical, while they differed in DMF. Thus, from these observations, it was surmised that, in the absence of KO_2 and 18-C-6, when dissolved in NCMe or THF, **2** remained unchanged, but that in DMF, substitution of DMF for NCMe to yield $[Ni^{II}(PyN_2^{iPr2})(DMF)]$ (**5**, see section 2.2.2).

Addition of 2 eq. KO_2 (4 eq. 18-C-6, DMF) to a 0.125 mM solution of **2** at 25 °C yielded the changes seen in the absorbance spectra of Figure 13 (blue trace, a, b, c for THF, DMF and NCMe respectively) after approximately 150 s. Addition of less than two equivalents of KO_2 gave a lower yield of the final species (reduced intensity), while addition of more than 2 eq. KO_2 led to minor decreases in absorption due to dilution. In all three solvent systems, similar changes in the absorption spectra occurred (λ_{max} = 310, 375, 470 nm (red trace, DMF), λ_{max} = 320, 370, 470 nm (blue trace, NCMe), λ_{max} = 320, 370, 400 (sh), 470 nm (black trace, THF), Fig. 14). Control reactions involved the addition of the same volume and concentration of 18-C-6 (4 eq., DMF) and changes in the UV-vis spectra of these control reactions can be seen in Figure 13 (d, e, f for THF, DMF and NCMe respectively). Addition of a solution of 18-C-6 dissolved in DMF to a solution of **2** dissolved in THF yielded **5** as can be seen by comparison of the final blue trace of Figure 13d and the initial black trace of Figure 13b, both of which were characterised by an absorption band at λ_{max} = 350 nm. However, in NCMe, **2** was unchanged in the presence of DMF, likely due to the large excess of NCMe relative to DMF present shifting the equilibrium to **2**. Thus, this implicated KO_2 as the active species for the changes in the UV-vis spectrum.

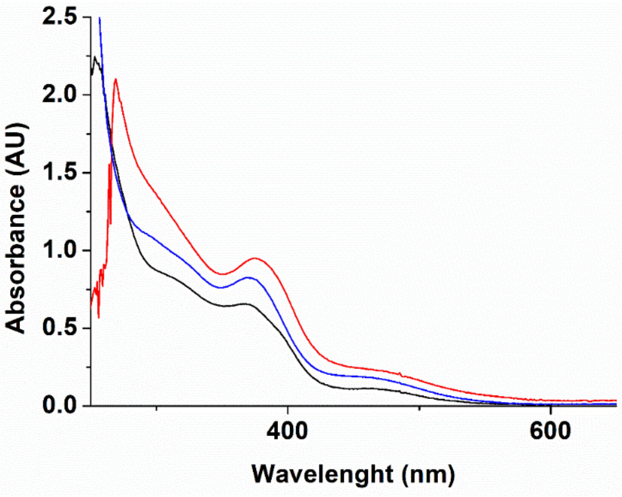

Figure 14. Comparison of the final products obtained after addition of 2 eq. KO_2 to **2** (red trace = DMF, blue trace = NCMe and black trace = THF).

No differences in the reactivity were observed at sub-zero temperatures, merely a reduction in the rate of formation was observed. The intensity of the absorbance features at λ_{max} = 310, 375, 470 nm, formed from the addition of 2 eq. KO_2 and 4 eq. 18-C-6 to a DMF solution of **2** were found to increase linearly as a function of the concentration of the complex at 25 °C (Fig. 15 (a)). When the reaction was carried out a 1mM DMF solution of the complex the presence of a weak absorption feature at 650 nm, which was not visible at lower concentrations, was observed (Fig. 15 (b)).

The reaction was expected to yield a complex of the form $[Ni^{II}(PyN_2^{iPr2})(O_2)]^-$, (**6**) but the UV-vis absorption features were strikingly similar to that of $NEt_4[Ni^{II}(PyN_2^{iPr2})(OCO_2H)]$, (**8b**) formed by Holm and co-workers. This complex was formed by the reaction of $NEt_4[Ni^{II}(PyN_2^{iPr2})(OH)]$, (**7b**) with CO_2 in DMF.[90] **8b** had characteristic UV-vis features at 306, 369 and 475 nm, which matched quite well with those from the reaction of **2** and KO_2 with absorption features at λ_{max} = 310, 375 and 470 nm.[90] Differences in the energies were attributed to the change in counterions. Thus, it was surmised that the addition of KO_2 to a solution of **2** lead to the formation $K[Ni^{II}(PyN_2^{iPr2})(OCO_2H)]$ (**8a**), based on the UV-vis data.[90] $K[Ni^{II}(PyN_2^{iPr2})(OCO_2H)]$ was later surmised to form from the intermediate $K[Ni^{II}(PyN_2^{iPr2})(OH)]$, formed from the reaction of **2** and KO_2 (discussed in section 2.2.3)

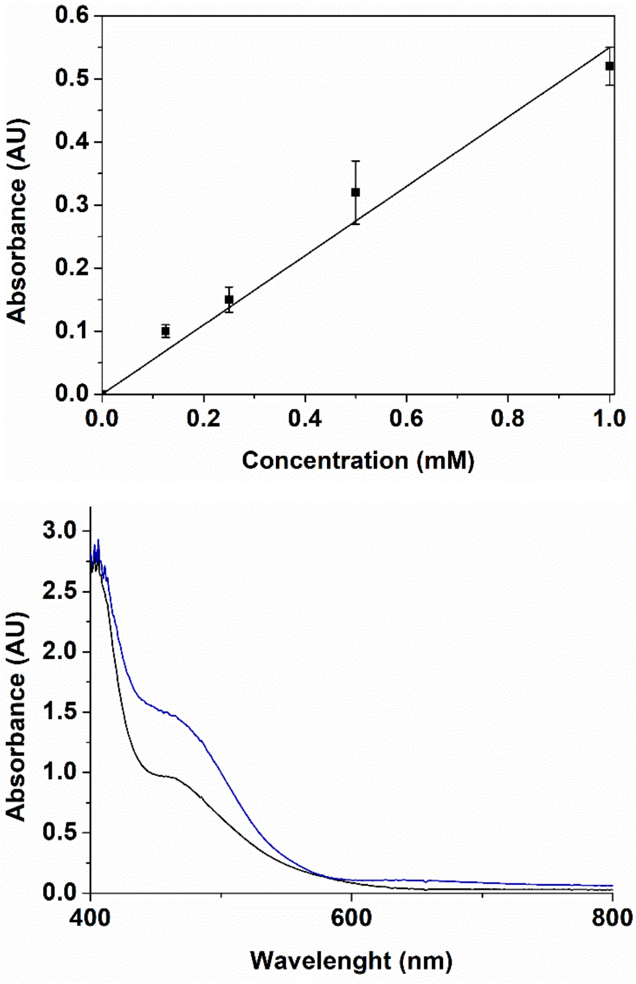

(a) (b)

Figure 15. (a) Absorbance at 470 nm vs concentration of **2** used ($R_{adj}^2 = 0.9875$). (b) UV-vis trace of **2** (1 mM, DMF) before the addition of KO_2 (black trace) and after the addition of 2 eq. KO_2 (blue trace).

The absorption features of **8a** were found to change slowly over time, over a period of 24 h, to a new species which will be discussed further below (Section 2.2.6). Due to this slow decay, a solution of the reaction mixture was frozen after addition of KO_2 and then thawed just prior to cold-injection ESI-MS (Table 6). Two distinct mass peaks (not observed in ESI-MS of **2**) were observed at m/z = 573.2040 and 696.2003 respectively (Figures S6, S7). Comparison with the ESI-MS of control solutions of **2** and **2** + 18-C-6 are shown in Table 6 below. The mass peak at m/z = 573.2040 matched well with a proposed Ni^{II}-superoxide, $[Ni^{II}(PyN_2^{iPr2})(O_2)]^-$ (**6**) (calc. m/z = 573.2138). The mass peak at m/z = 696.2003 could not be assigned. The mass peak at m/z = 576 was assigned as $[Ni^{II}(PyN_2^{iPr2})(Cl)]^-$ (calc. $C_{31}H_{37}ClN_3NiO_2$ = 576.1928) while the mass peak at 572 was assigned as $[Ni^{II}(PyN_2^{iPr2})(OMe)]^-$ (calc. $C_{32}H_{40}N_3NiO_3$ = 572.2423). Both ions were assumed to form within the spectrometer.

Table 6. Negative-mode cold-injection ESI-MS of **2**, **2 +** 18-C-6 and **2** + KO_2 + 18-C-6. Y (main) indicates the major mass peak. Y indicates peak present. X indicates no mass peak present.

Complex	**Mass Peak**			
	572	**573**	**576**	**696**
2	Y	X	Y (main)	X
2 + 18C6	Y	X	Y (main)	X
2 + KO_2 +18C6	Y	Y (main)	Y	Y

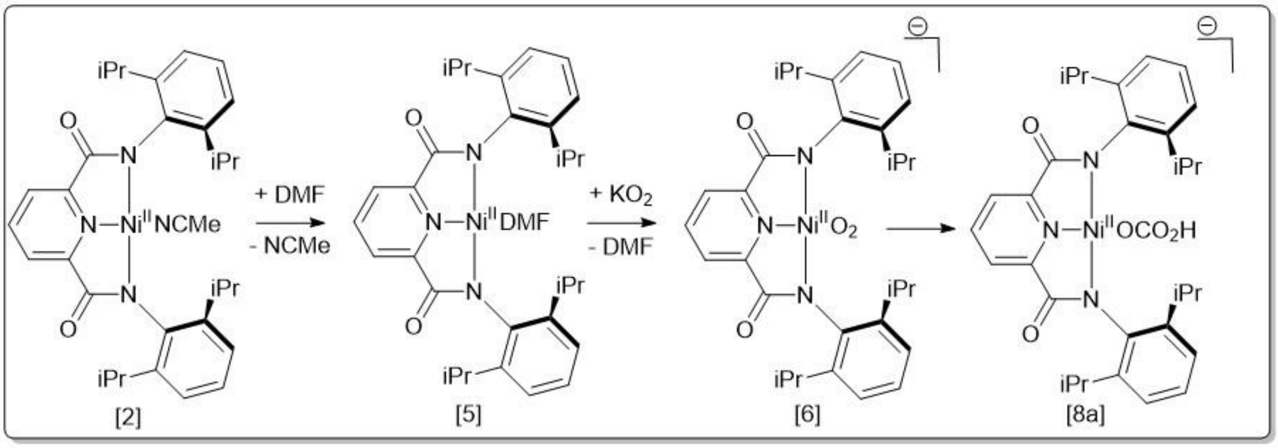

Scheme 7. Proposed reaction of **2** with KO_2 in DMF.

Thus, from the obtained UV-vis and ESI-MS data, the reaction of **2** with KO_2 in DMF was presumed to follow that of Scheme 7. Dissolution of **2** in DMF lead to association of the DMF residue to the Ni^{II} centre, to give **5** as surmised from the analyses of control spectra in Figure 13 ((d), (e) and (f)). Addition of KO_2 lead to the formation of **6**. This intermediate then decayed to form **8a** which has strikingly similar UV-vis absorption features as the previously reported **8b**.

2.2.2 Synthesis and characterisation of [Ni^{II}(PyN$_2$^{iPr2})(DMF)]

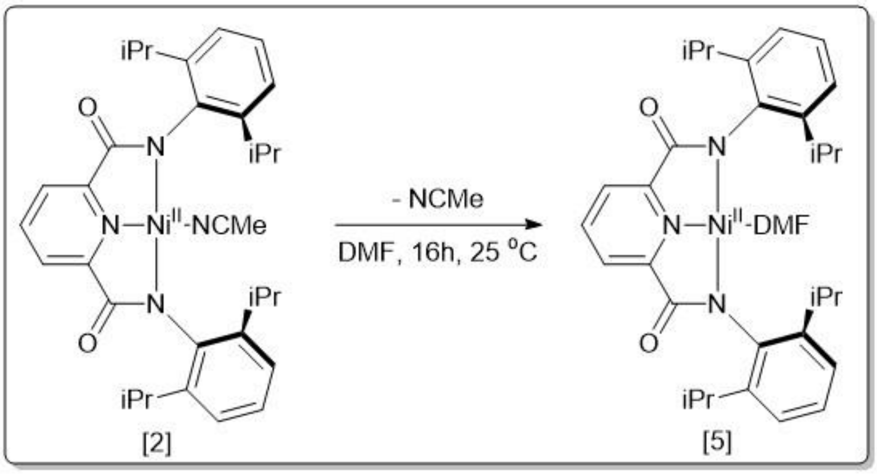

Scheme 8. Synthesis of **5**

In order to test the hypothesis of DMF coordination, a sample of **2** was dissolved in DMF and stirred overnight, followed by the addition of excess ether (Scheme 8). The red solution was left in a freezer to yield dark red crystals after several days, which were suitable for single crystal XRD. The resulting molecular structure identified the product as **5** (Fig. 16). The resulting asymmetric unit contained two crystallographically independent, but conformationally identical, molecules of **5** and one disordered diethyl ether molecule. Major bond lengths and angles are given in Tables 7 and S1. For complex **5** both crystallographic molecules were present in distorted square planar geometries as evidenced by their τ_4 (0.13 and 0.15) and τ_4' (0.10 and 0.14) values respectively. The τ_4 value (equation 5) has been used in crystallography to define the degree of distortion in a tetra-coordinate metal atom.[109] When τ_4 is close to zero, the coordination sphere is best described as square planar, while a value of 1 indicates a tetrahedral geometry. However, the formula does not distinguish between the largest two valence angles (used in the calculation) and thus since 2015, a more accurate parameter, τ_4', has been used which more accurately reflects changes in the overall structure of the complex (equation 6).[110] Similarly, a value of 0 indicates a square planar geometry while a value of 1 indicates a tetrahedral structure. These values compare well with those of **2**, 0.12 and 0.08 for τ_4 and τ_4' respectively, indicating that the change in coordinated solvent residue has not deviated the square planar geometry.[86]

$$\tau_4 = \frac{360-(\alpha+\beta)}{360-2\theta} \qquad (5)$$

$$\tau_4' = \frac{\beta - \alpha}{360 - \theta} + \frac{180 - \beta}{180 - \theta} \qquad (6)$$

The bond lengths of 1.8190(12)/1.8169(13) Å, 1.8992(13)/1.9027(13) Å (Ni-N_{py}) and 1.9153(13)/1.9027(12) Å (Ni-N_{am}) differ by only 0.01 – 0.02 Å when compared to those of **2**. The Ni-O_{DMF} bond length of 1.8786(11)/1.8747(11) also differs only by 0.01 Å when compared to the Ni-N_{NCMe} bond of **2**, even though the two complexes differ by the atom which is coordinated (O for **5** vs. N for **2**).[86] The only bond angles of the first Ni-coordination sphere which are appreciably different are those incorporating the DMF oxygen atom (N_{am}-Ni-O_{DMF}) of **5** which differ from the corresponding angle in **2** (N_{am}-Ni-N_{NCMe}) by ~ 3 – 4 ° (Table S1).[86] The phenyl rings of **5** which lay at an angle of 89.02 ° and 75.54 ° for unit 1 and 83.09 ° and 74.70 ° for the second crystallographically unique unit of the unit cell (Table S1).

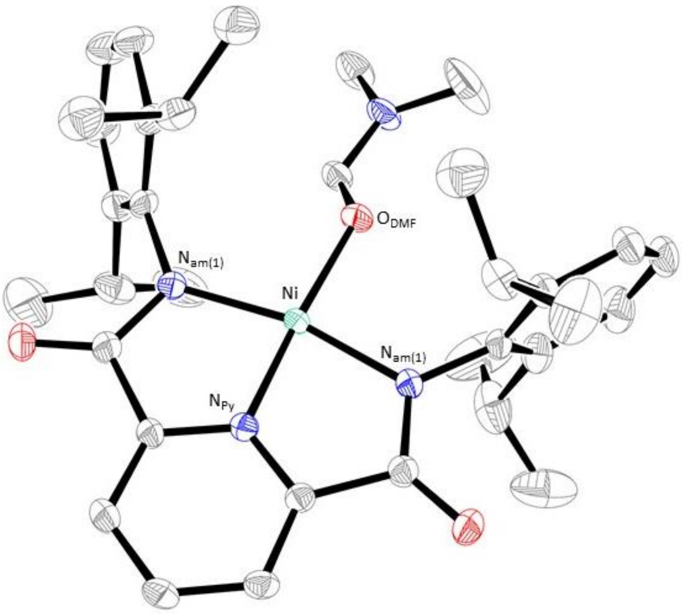

Figure 16. Molecular structure of **5** showing one of two crystallographically independent molecules. Hydrogen atoms omitted for clarity. Thermal ellipsoids shown at 50 % probability.

Table 7. Major bond lengths of **5**

	Unit 1	Unit 2
Bond	Length (Å)	Length (Å)
Ni-O_{DMF}	1.8786(11)	1.8747(11)
Ni-N_{py}	1.8190(12)	1.8169(13)
Ni-$N_{am(1)}$	1.8992(13)	1.9027(13)
Ni-$N_{am(2)}$	1.9153(13)	1.9027(12)

The ^{1}H NMR spectrum of **5** was characteristic of such Ni^{II} complexes with pyridine dicarboxamide ligands (Fig. 17).[88,111] Of note was the appearance of three new singlets in the NMR spectrum: 5.28, 2.32 and 1.65 ppm. The integration pattern of 1:3:3 matched well with a Ni-coordinated DMF moiety (free DMF in $CDCl_3$ has: 7.95, 2.89 and 2.73 ppm, all singlets).[112] Thus, it appeared that Ni binding of the DMF moiety largely shifted these resonances, the aldehyde proton most of all, as expected due to carbonyl group coordination as seen in the molecular structure (Fig. 16). From the IR spectrum, the intense peaks located at 1627 and 1256 cm^{-1} respectively can be assigned as the ν(C=O) and ν(N-C) of the DMF moiety respectively, which were shifted relative to the free DMF values of 1677 and 1288 cm^{-1} (Fig. S8).[113] ESI-MS yielded two mass peaks at in the negative mode at m/z = 572.2413 and 576.1936 of which the latter was assigned as $[Ni^{II}(PyN_2^{iPr2})(Cl)]^-$ (calc. 576.1928). The former could be assigned as $[Ni^{II}(PyN_2^{iPr2})(OMe)]^-$ (calc. 572.2423). Both species were assumed to have formed within the ionisation chamber. Presumably the DMF moiety was too labile to be identified by ESI-MS which would yield a calculated mass peak at 613.2759 $[[Ni^{II}(PyN_2^{iPr2})(DMF)] - H]^-$. Upon dissolution of **5** in DMF, the UV-vis spectrum matched that of **2** in DMF, as in Figure 13(b) (black trace).

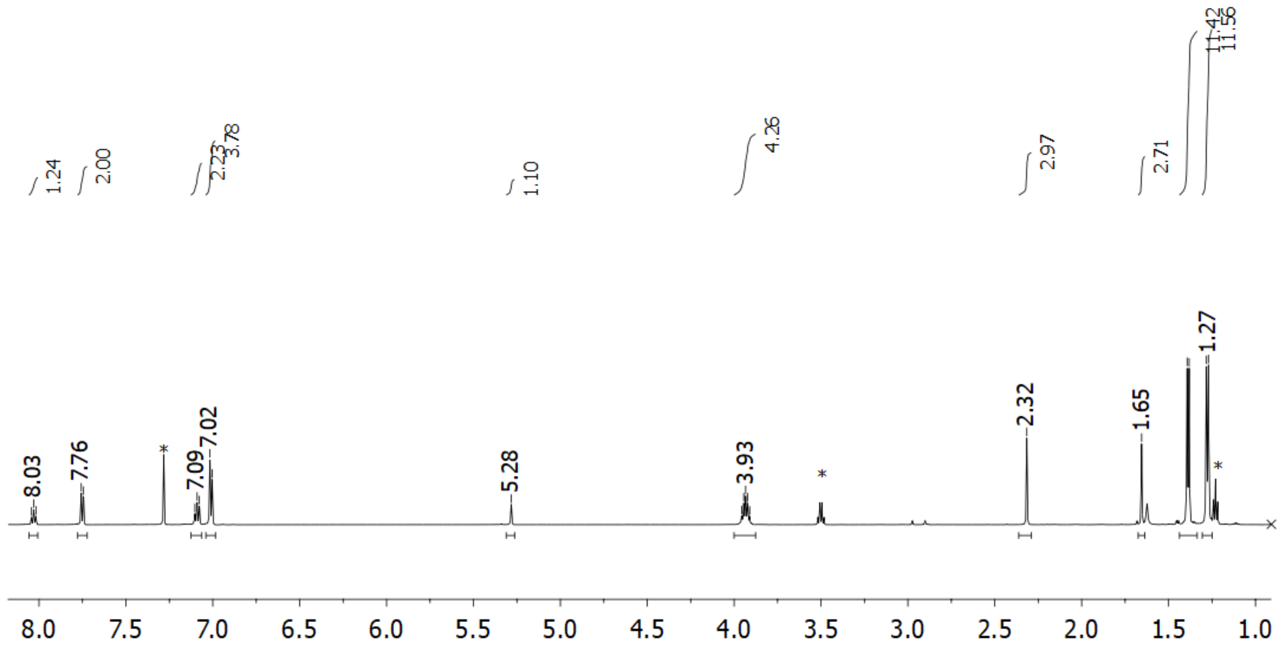

Figure 17. ^{1}H NMR spectrum of **5** in $CDCl_3$. * refers to solvent peaks ($CHCl_3$ (7.26 ppm) and Et_2O (1.21/3.48 ppm))

2.2.3 Scale-up reaction of $[Ni^{II}(PyN_2{}^{iPr2})(NCMe)]$ and KO_2

The reaction of **2** with KO_2 and 18-C-6 in DMF was carried out at a 34 mM concentration, under an N_2 atmosphere in order to analyse the formed product. To a 4:1 THF:DMF (5 mL) solution of **2** was added 2 eq. of KO_2 and 4 eq. 18C6 dissolved in DMF (2 mL). Stirring of the reaction mixture for 1 day followed by filtration and layering with Et_2O yielded a red crystalline product after 2 - 3 days which was suitable for single crystal XRD and which was characterised as $K[Ni^{II}(PyN_2{}^{iPr2})(OH)]$ (**7a**).

The IR spectrum of the product displayed a vibrational stretch at 3595 cm^{-1} indicative of a bound hydroxide (Fig. S10). The metal-bound amide C=O stretches of the pyridine dicarboxamide ligand were observed at 1619 and 1605 cm^{-1}. In the ^{1}H NMR spectrum a new singlet was observed at -5.38 ppm which integrated to one proton in comparison to the other seven ligand signals (Fig. 18 top). It was therefore assigned to the hydroxide moiety. The remaining peaks of the NMR spectrum were assigned to the bound pyridine dicarboxamide ligand, and followed the typical pattern of this family of complexes.[88,111] The singlet at 3.51 ppm was assigned as free 18-C-6.[114]

Independently, a sample of **7b** was prepared by the reaction of **1**, NEt_4OH and $Ni(OTf)_2$ in THF as reported in the literature.[90] IR spectroscopy identified the OH stretch at 3586 cm^{-1} (Fig. S11). The resulting ^{1}H NMR was compared to that of **7a**, in DMSO-D_6, showing identical chemical shifts for all peaks, apart from a minor deviation for the OH residue (ΔOH = 0.06 ppm), as well as the presence of the NEt_4 counterion at 1.13 and 3.17 ppm (Figure 18 bottom). Thus, the two complexes were identical by NMR.

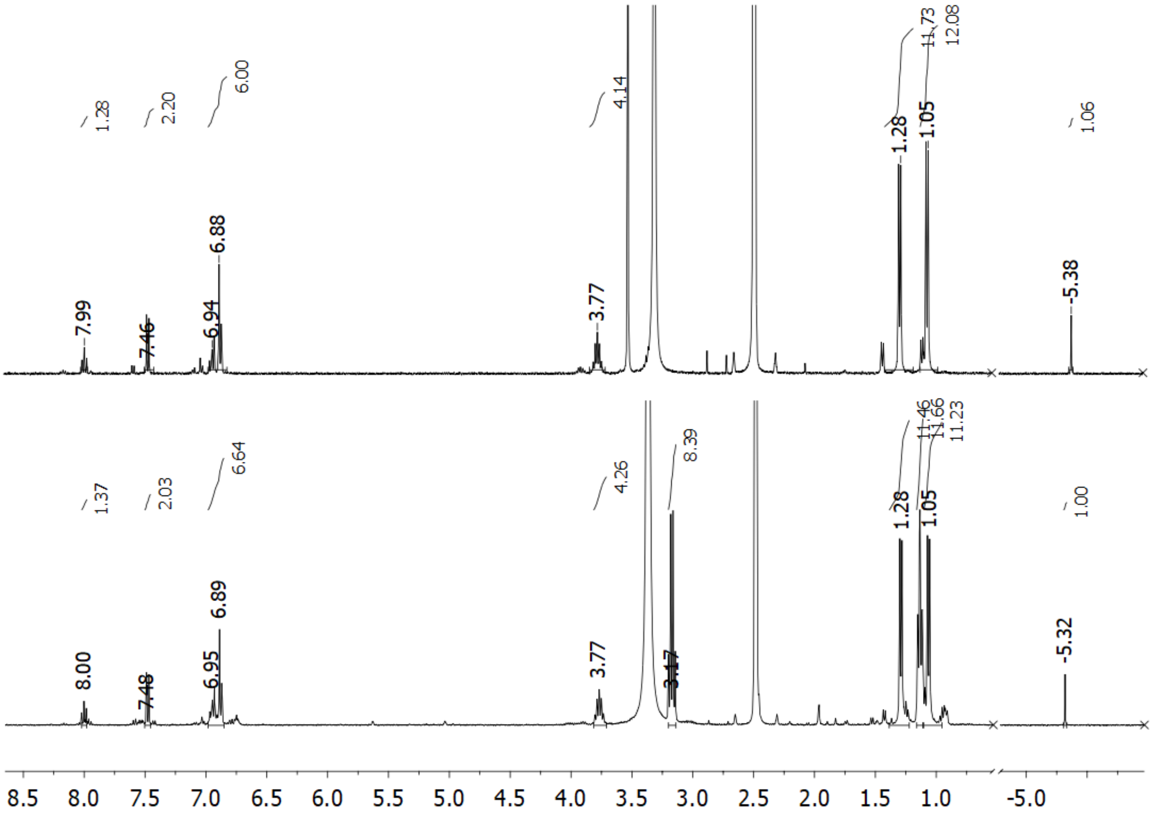

Figure 18. Comparison of the ^{1}H NMR of **7a** (top, singlet at 3.51 is free 18-C-6) and **7b** (bottom). Solvent peaks present at 3.33 (H_2O) and 2.5 (DMSO).

Single crystal XRD analysis of **7a** showed two crystallographically identical molecules in the asymmetric unit, of which one was modelled as a disordered moiety with 65:35 occupancy (Fig. 19). There were also 4 half-occupied K^+ ions and 2 half-occupied and disordered 18-C-6 units. The void contained a mixture of solvents, 3 half-occupied Et_2O (one in two sites 25:75% occupancy) and THF (fully occupied). Major structural parameters are represented in Table 8 below. Each Ni^{II} ion was present in a square planar geometry, as referenced by the τ_4 = 0.11, 0.11 and 0.14 for unit 1, 2a and 2b respectively with 3 N-donors from the pyridine dicarboxamide ligand as well as a coordinated hydroxide OH unit. Interestingly the solid-state structure was that of a dimeric unit bridged by a potassium ion, which acted as a centre of inversion. This dimeric structure in the solid state was in stark contrast to that of **7b** which was a monomeric species.[114] All bond lengths were found to mirror those of the reported structure of **7b** by Holm and co-workers with only minor deviations (Table 8).[114] Interestingly, the Ni-O(H) bond length appeared unaffected by the interaction with the bridging K^+ ion, which was not present in **7b**. Finally, it was noted that the K^+ ion bridging the Ni-OH units had a weak interaction with one of the aromatic rings of each pyridine dicarboxamide ligand. This was visible by the differences of the distance between the centroid of each aromatic ring and the bridging potassium ions: 2.972(2), 2.999(3), 2.998(2) Å, vs 5.684(3), 5.710(3), 5.563(3) Å distances for unit 1 and 2 (65:35 moieties) respectively.

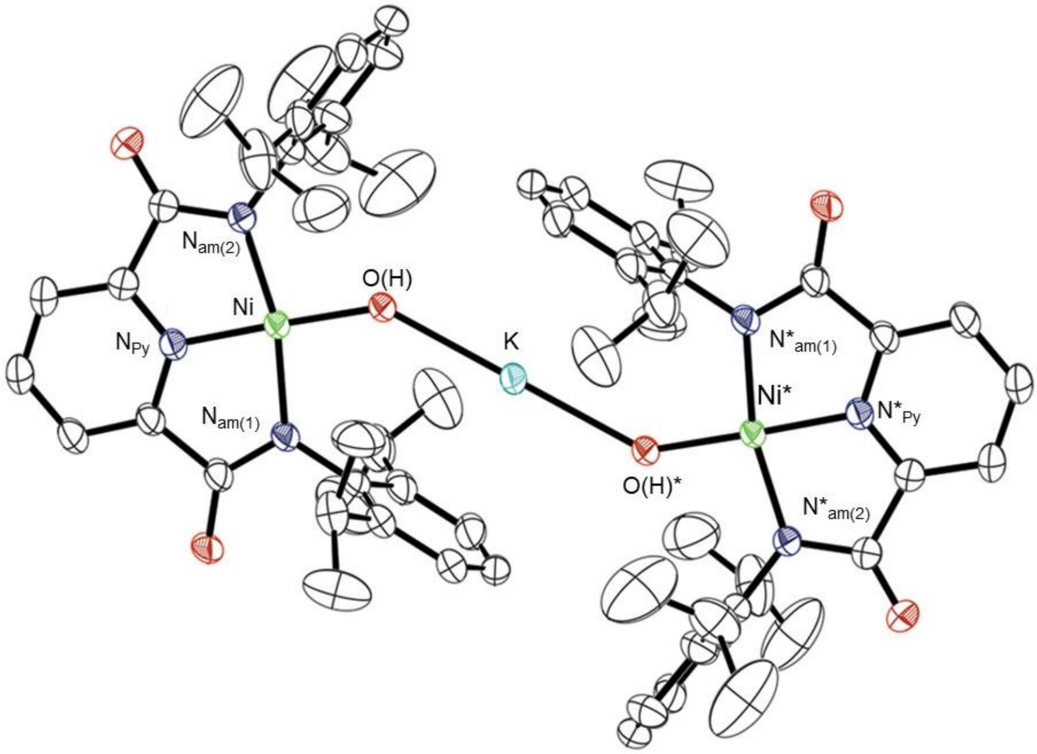

Figure 19. Molecular structure of $[Ni^{II}(PyN_2^{iPr2})(OH)]^-$. 18-C-6, solvent residues, protons and counterions (except bridging K^+) omitted for clarity. Thermal ellipsoids shown at 50 % probability.

Table 8. Major structural parameters of **7a**. Unit 2A and 2B refer to the 65:35 disordered modelled moieties of the second unit.

	Unit 1	Unit 2A	Unit 2B	**7b**[90]
Ni-O(H)	1.814(2)	1.805(12)	1.82(2)	1.820
Ni-N_{py}	1.812(2)	1.819(5)	1.782(7)	1.818
Ni-$N_{am(1)}$	1.898(3)	1.895(5)	1.929(12)	1.906
Ni-$N_{am(2)}$	1.896(2)	1.887(9)	1.960(2)	1.909
τ_4	0.11	0.11	0.14	0.11
τ_4	0.07	0.07	0.11	0.07

A summary of the ESI-MS data for **7a** and **7b** is present in Table 9 below. Both **7a** and **7b** had a mass peak corresponding to the $[Ni^{II}(PyN_2^{iPr2})(OH)]^-$ anion at m/z = 558.2356 and 558.2326 respectively (calc. $C_{31}H_{38}N_3NiO_3$ = 558.2267, Fig. S12, S13) as well as mass peaks at m/z = 572 ($[Ni^{II}(PyN_2^{iPr2})(OMe)]^-$, calc. = 572.2423) m/z = 576, ($[Ni^{II}(PyN_2^{iPr2})(Cl)]^-$, calc. = 576.1928) and 586 ($[Ni^{II}(PyN_2^{iPr2})(O_2CH)]^-$, calc. $C_{32}H_{38}N_3NiO_4$ = 586.2216), all of which were presumed to have formed in the ionisation chamber. The mass peaks at m/z = 554.2113 and 556.2184 however were unique to the reaction mixture containing **7a**. The latter was been assigned as a Ni^{II} complex of the form $[Ni(PyN_2^{iPr,iPrO})]^-$, (**9a**) (calc. $C_{31}H_{36}N_3NiO_3$ = 556.2110, $H_2PyN_2^{iPr,iPrOH}$ (**10a**) = N-(2,6-diisopropylphenyl)-N’-(2-(2-hydroxypropan-2-yl)-6-isopropylphenyl)pyridine-2,6-dicarboxamide) wherein an oxygen moiety has been inserted into the isopropyl group) pyridine dicarboxamide ligand (discussed and characterised in detail below in section 2.2.6). The former has tentatively been assigned as $[Ni[(PyN_2^{iPr,EtCHO})$ (**9b**) - $H]^-$ (calc. $C_{31}H_{34}N_3NiO_3$ = 554.1954 , $H_2PyN_2^{iPr,EtCHO}$ (**10b**) = N-(2,6-diisopropylphenyl)-N’-(2-isopropyl-6-(1-oxopropan-2-yl)phenyl)pyridine-2,6-dicarboxamide) wherein **9a** has been further oxidised to an aldehyde (at the methyl position). These mass peaks have been hypothesised to be due to the formation of secondary products formed from an intramolecular reaction involving **6** with the pyridine dicarboxamide ligand in an electrophilic oxidation reaction.

Table 9. Summary of the mass peaks present in the negative mode ESI-MS spectra of **2**, **7a** and **7b**. Y indicates a mass's presence, X indicates its absence.

Mass peak	Complex		
	2	**7a**	**7b**
554 $[Ni^{II}(PyN_2^{iPr,\ EtCHO} - H]^-$	X	Y	X
556 $[Ni^{II}(PyN_2^{iPr,\ iPrO})]^-$	X	Y	X
558 $[Ni^{II}(PyN_2^{iPr2})(OH)]^-$	X	Y	Y
572 $[Ni^{II}(PyN_2^{iPr2})(OMe)]^-$	Y	Y	X
576 $[Ni^{II}(PyN_2^{iPr2})(Cl)]^-$	Y	Y	Y
586 $[Ni^{II}(PyN_2^{iPr2})(O_2CH)]^-$	X	Y	Y

Thus, from the above ^{1}H NMR and XRD results, it is proposed that **2** reacted with KO_2 in DMF to yield the intermediate **6** which led to the formation of **7a**. Analysis by ESI-MS also suggested that **9a** and **9b** were being formed as side products in the reaction. The formation of these compounds was studied in more detail in section 2.2.6.

2.2.4 Effect of reacting $[Ni^{II}(PyN_2^{iPr2})(NCMe)]$ with H_2O_2

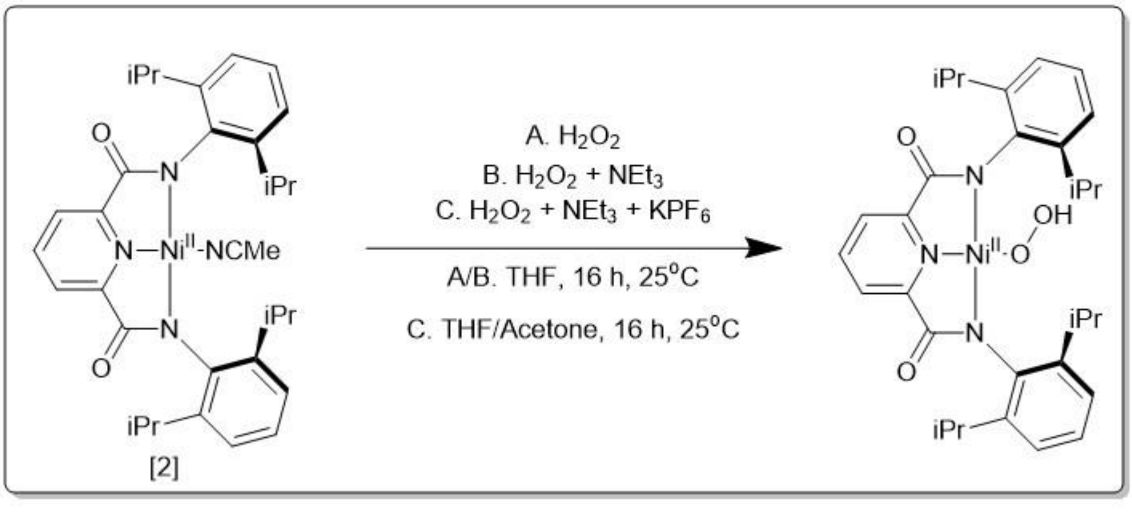

Scheme 9. Hypothesised reaction of **2** with H_2O_2 (A), H_2O_2 + NEt_3 (B) and H_2O_2 + NEt_3 + KPF_6 (C).

A possible explanation for the formation of **7a** was that KO_2 was first disproportioning to dioxygen and dipotassium peroxide (equation 7),[4,115] followed by reaction of peroxide with **2**.

$$2KO_2 \rightarrow K_2O_2 + O_2 \qquad (7)$$

To test this hypothesis, reactions A - C in Scheme 9 were carried out with 2 eq. of H_2O_2, 2.1 eq. of NEt_3, and 2 eq. KPF_6 acting as a K^+ ion source. Reaction C involving KPF_6 required acetone in order to solubilise the salt. The reactions were left to stir overnight before being filtered, and the solvent removed *in vacuo* to yield red powders. ^{1}H NMR spectroscopy clearly showed that no reaction had taken place and that only the starting material was present (Fig. 20). Thus, it was concluded that the formation of **7a** was dependent on the reaction of **2** with KO_2 and independent of a peroxide decay product from KO_2.

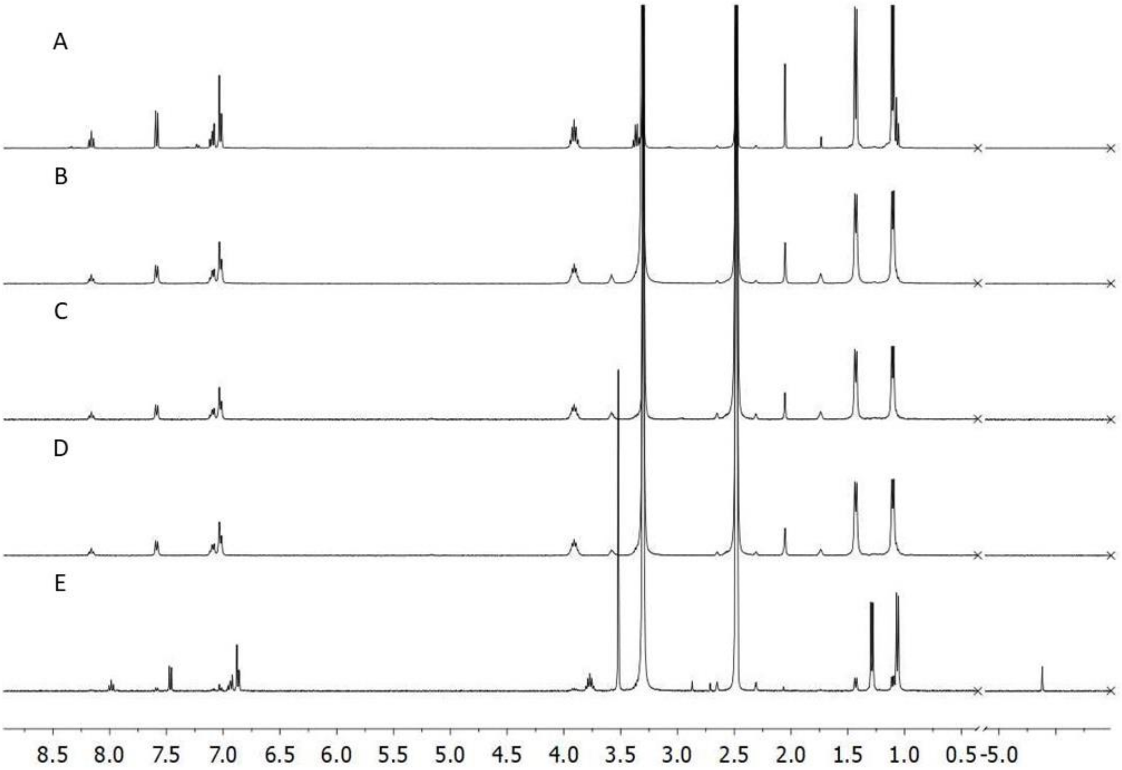

Figure 20. Comparison of the ^{1}H NMR spectrum of **2** (A), **2** + H_2O_2 (B) **2** + H_2O_2, NEt_3 (C), **2** + H_2O_2, NEt_3, KPF_6 (D), and **7a** (E). Solvent peaks present at 3.33 (H_2O) and 2.5 (DMSO). The singlet at 3.51 in E was free 18-C-6.

2.2.6 Analysis of the post reaction mixture [$Ni^{II}(PyN_2^{iPr2})(NCMe)$] + KO_2

Interestingly, it was found that the UV-vis features of the reaction mixture of **2** + KO_2 + 18-C-6 in DMF changed gradually over time. Stirring of this solution over 24 h under atmospheric conditions yielded the changes seen in Figure 21. This new species was characterised by absorption features at λ_{max} = 390 and 490 nm.

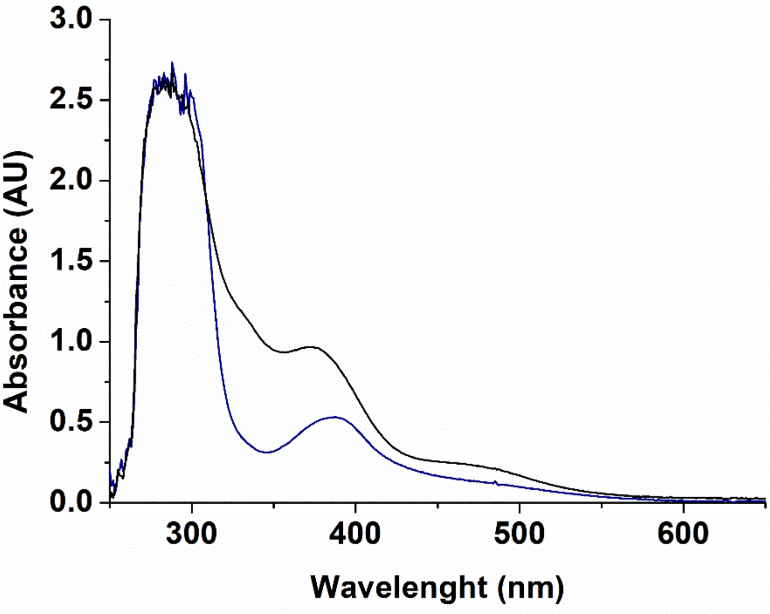

Figure 21. UV-vis trace of the reaction mixture of **2** + KO_2 + 18-C-6 (0.125 mM, DMF, black trace) and its decay product after 3 days (blue trace).

In order to gain an insight into the identity of the new species, samples of the reaction mixture were frozen after different periods of time and were analysed by cold injection ESI-MS (Table 10). Immediately after addition of the KO_2 and 18-C-6, there were two major mass peaks present in the negative mode of the mass spectrum at m/z = 573.2158, and 696.2161 and a weak mass peak at m/z = 583.2172. The peak at m/z ~ 696 disappeared rapidly (Table 10) while two new features at m/z = 554.1970 (Fig. S14) and 556.1976 (Fig. S15), as well as 583.2172 (Fig. S16), grew gradually into the spectrum as the peak at 573.2158 reduced in relative intensity. The peak at 583 could not be assigned but was presumed to be caused by a change in **8a**, of which the bicarbonate residue was too labile to allow characterisation by ESI-MS.[90] It must be noted that ESI-MS is a qualitative technique and thus, care must be given when comparing relative peak intensities over time. However, there was a significant trend observed in the relative intensities of the m/z = 554 and 556 peaks vs. m/z = 573 peak. This data agrees with that in the ESI-MS analysis from Table 9, suggesting that the products of the reaction mixture form over time from the hypothesised complex **6** (m/z = 573).

Table 10. ESI-MS data for selected mass peaks for the reaction of **2** + KO_2 + 18-C-6 at different time points. Y (main) indicates the major peak in the MS spectrum, Y indicates a peak present, X indicates a peak's absence.

mass peak	**554**	**556**	**573**	**583**	**696**
Time					
Complex **2**	N	N	N	N	N
Straight after adn.	N	N	Y (main)	Y(weak)	Y
5 min	Y (weak)	Y (weak)	Y (main)	Y	N
15 min	Y	Y	Y (main)	Y(weak)	Y (weak)
30 min	Y	Y	Y (main)	Y	N
60 min	Y	Y	Y (main)	Y	N
120 min	Y	Y	Y (main)	Y	N
24 h	Y	Y (main)	Y (weak)	Y	N

In order to isolate the proposed side-products from the reaction of **2** and KO_2, with mass peaks of m/z = 554.1970, **9b**, and 556.1976, **9a**, an acidic workup of the post-reaction mixture was performed on an up-scale reaction (Scheme 10). A solution of **2**, 2 eq. KO_2 and 4 eq. 18-C-6 were stirred in DMF under an inert atmosphere for 24 h to which 1M HCl was added. The solution was stirred until the red solution had turned colourless indicating complete demetallation. The resulting off-white solid, was analysed by ^1H NMR, ^{13}C NMR, HSQC, HMBC and IR spectroscopies and ESI-MS.

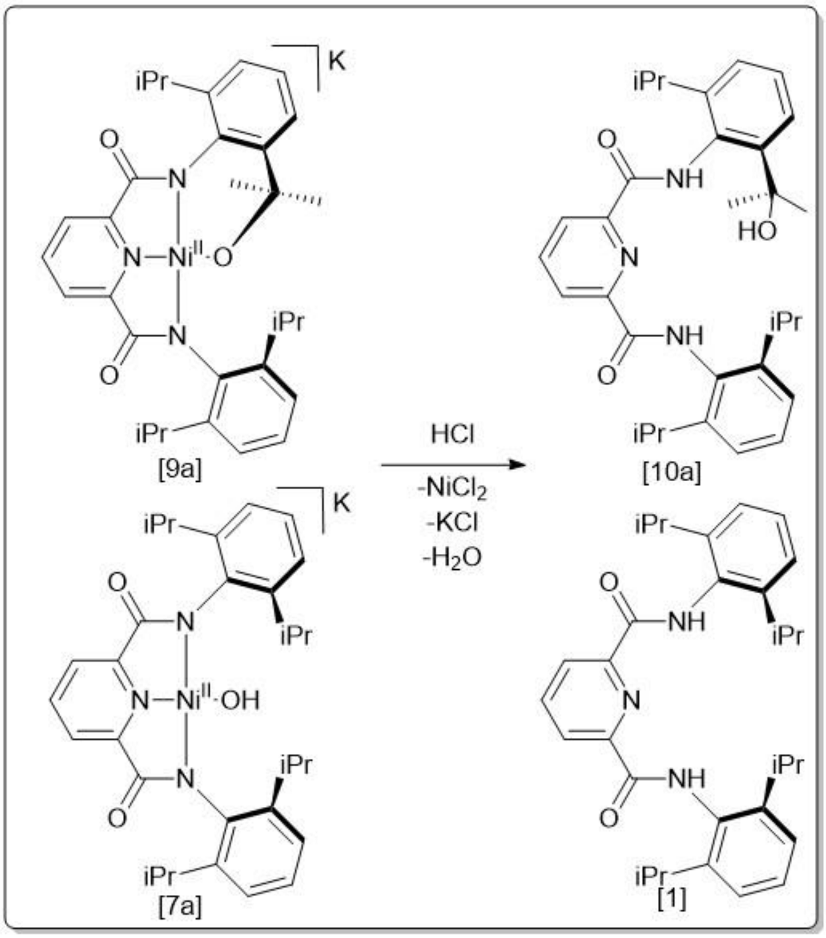

Scheme 10. Demetallation of **9a** and **7a** with HCl yielding **10a** and **1**

The resulting ESI-MS spectrum showed two main peaks in the negative mode with m/z = 484.3166, m/z = 500.2865 which were identified as [**1** – H]$^-$ (calc. $C_{31}H_{39}N_3O_2$ = 484.2964) and [**10a** - H]$^-$ (calc. $C_{31}H_{38}N_3O_3$ = 500.2913) respectively. The ^{1}H NMR spectrum showed an approximate 1:1 mixture of two species present of which one was the previously characterised **1**, while the other was identified as **10a** (Scheme 10, Fig. S17). The ratio of the two species was determined by comparison of the N-H residues of **1** (1 singlet due to equivalency) and **10a** (2 singlets of equal intensity). Interestingly, when the reaction was repeated but stirred for only 15 minutes prior to the addition of acid, only **1** was isolated. This result provided further precedent for the time-dependent ESI-MS data seen in Table 10 wherein the proposed product peaks at m/z = 554.1970 and 556.1976 were found to be formed over a period of many hours. However, no evidence for the formation of **9b** was seen by post-reaction acidified workup.

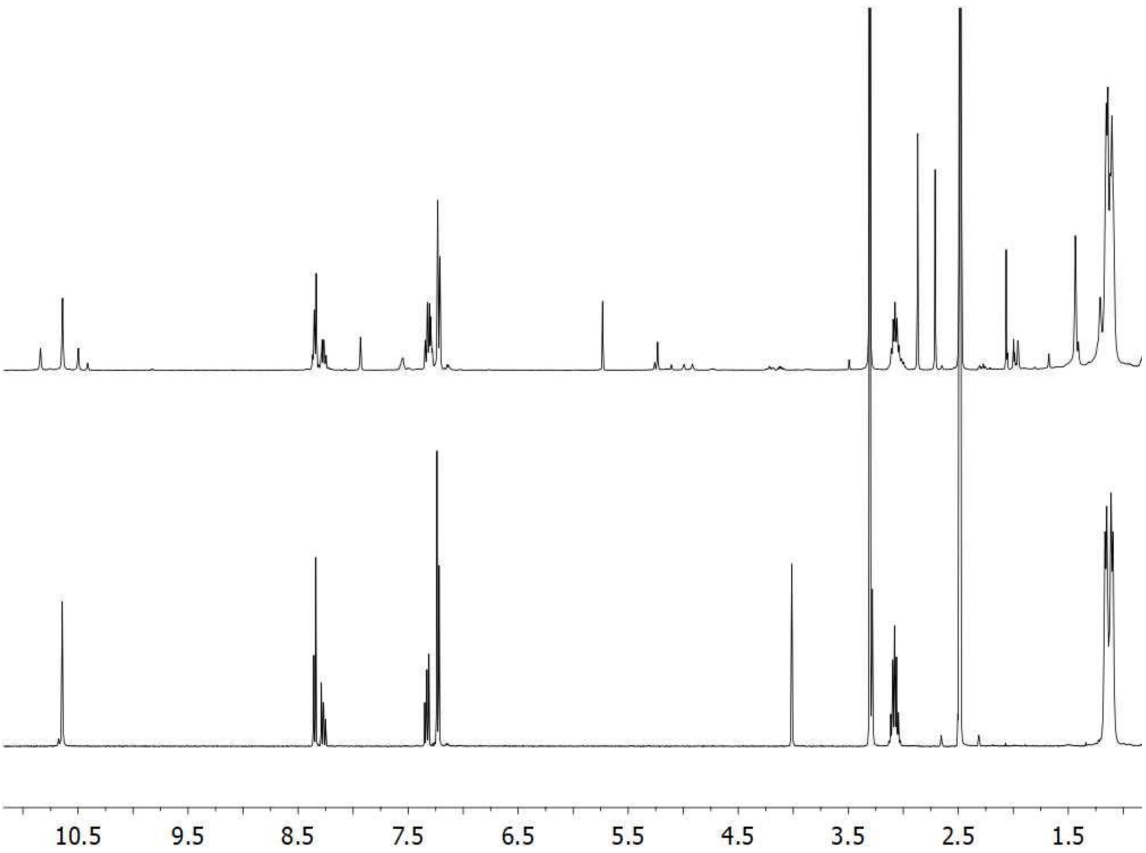

Figure 22. Comparison of the ^{1}H NMR spectra of the post-reaction acidified workup for the reaction of **2** + 2 eq. KO_2 + 4 eq. 18-C-6 (top) and **1** (bottom) in DMSO-D_6

The organic mixture was separated using preparative thin layer chromatography (TLC) using 20 % ethyl acetate in hexane in order to isolate **10a**. ESI-MS analysis showed two mass peaks at m/z = 484.3166 ([**1** - H]$^-$ calc. = 484.2964) and 500.2972 ([**10a** - H]$^-$, calc. = 500.2913) respectively (Fig. S18), suggesting contamination with **1**. The ^{1}H NMR spectrum is displayed in Figure 23 below and shows minor (< 10 %) contamination with **1**. Addition of a drop of D_2O cause the loss of the singlet present at 5.25 ppm, thus implicating it as the OH group, due to OH/OD exchange in solution. The multiplets at 3.04 and 3.09 integrated to 2 protons and 1 proton respectively and were assigned as the methine protons of the iPr groups on the aniline rings. The iPr methyl protons were found at 1.13 and 1.18 ppm as two overlapping doublets integrating to 18 protons, and a singlet found at 1.46 ppm which integrated to 6. This suggested that hydroxylation occurred at one iPr group only. The singlet corresponded to the iPr group wherein hydroxylation had occurred while the overlapping doublets were the remaining iPr group of the aniline rings. The two NH residues were present as equal intensity singlets at 10.52 and 10.86 ppm respectively due to the loss of C_2 symmetry through the pyridine moiety. Finally, the aromatic protons were present between 7.25 and 8.40 ppm.

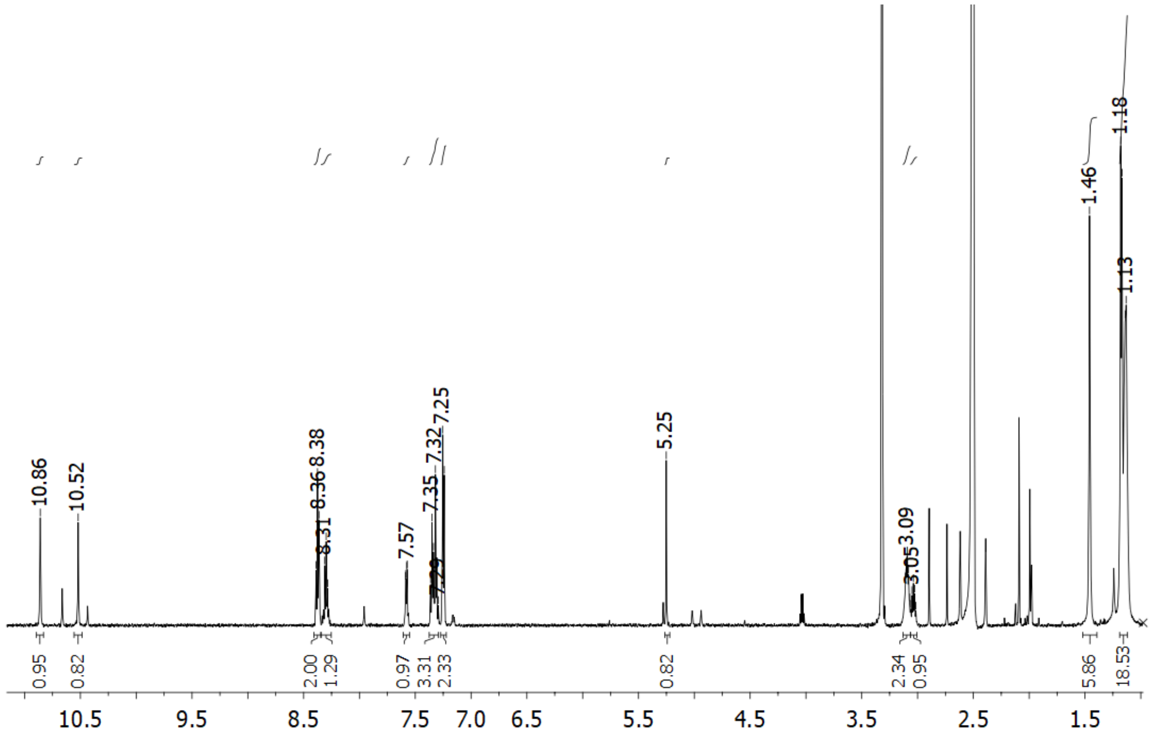

Figure 23. ^{1}H NMR spectrum of **10a** in DMSO-D$_6$. Solvent peaks are present at 2.5 (DMSO) 3.33 (H_2O), 2.74, 2.89 and 7.96 (DMF), 1.99 and 4.01 (ethyl acetate), 2.09 (acetone), 1.25 ppm (hexane).

In order to determine the hydroxylating agent, a number of control reactions were carried out. $O_2^{-\bullet}$ has been known to carry out electrophilic and nucleophilic oxidation reactions to a variety of organic compounds.[4,115,116] Thus, a solution of **1** and **7b** were separately stirred in DMF overnight with 2 eq. KO_2 and 4 eq. 18-C-6 for 24 h, followed by the addition of 1 M HCl. Subsequent workup and isolation of the organic product as a solid yielded ^{1}H NMR spectra which corresponding to **1** only (Fig. S19).

This result, coupled with the approximate 1:1 ratio of **1**:**10a** upon acidic workup of the post-reaction mixture, suggested that the complexes **7a** and **9a** were formed from **2** in two independent pathways of approximately equal probability. It is proposed that **2** reacted with KO_2 to form **6**, a Ni^{II}-superoxide complex, which then reacted rapidly with either the ligand or adventitious water to yield **9a** and **7a** respectfully.

2.2.7 Synthesis and characterisation of Na[Ni^{II}(PyN$_2$^{iPr2})(N$_3$)]

Karlin, Solomon and co-workers have previously suggested that metal-azide complexes can be used as structural mimics for metal-superoxide complexes, with the formed M-N$_3$ unit having a similar binding mode (due to the linearity of the azide moiety), and thus a similar L-M-N bond angle (L = ligand).[52] Of interest to this work is the positioning of the central nitrogen atom of the azide, which would mimic the distal oxygen of an end-on bound superoxide, and its positioning in relation to the iPr groups of the ligand.

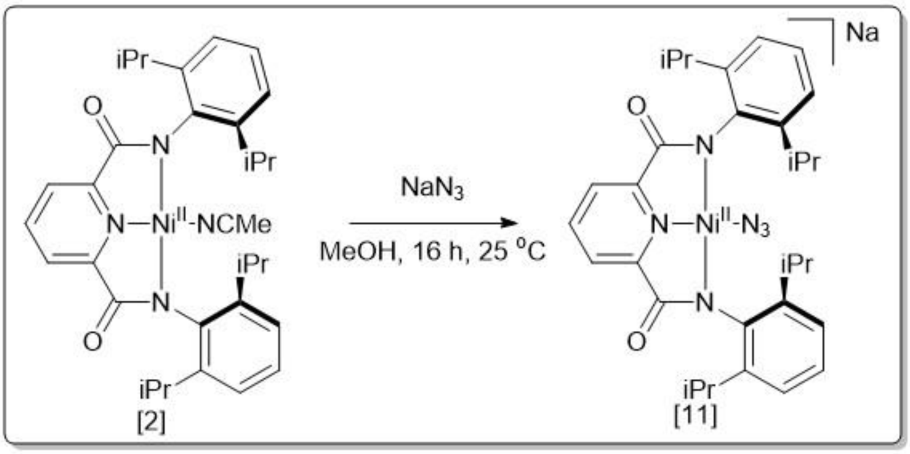

Scheme 11. Synthesis of **11**

The complex Na[Ni^{II}(PyN$_2$^{iPr2})(N$_3$)] (**11**) was synthesised by the reaction of **2** with 1.5 eq. NaN$_3$ by stirring overnight in MeOH (2 mL) (Scheme 11). Subsequent layering with Et$_2$O yielded an orange solid which was recrystallised from DMF and Et$_2$O to yield a red crystalline product after 3 days which was suitable for single crystal XRD. The complex was characterised by ^{1}H NMR, ^{13}C NMR, HSQC, HMBC, UV-vis and IR spectroscopies, ESI-MS and XRD.

The resulting molecular structure identified the formed complex as **11** (Fig. 24) wherein the azide moiety was disordered over two positions (24:76%), with three DMF moieties, two of which were disordered over two positions, coordinated at Na$^+$. Major structural parameters are available in Table 11 below. The τ_4 and τ_4' values of 0.13 and 0.10 respectively identified the Ni^{II} ion as being in a distorted square planar geometry.[107,108] The Ni-N$_{am}$ bonds differed by ~ 0.1 Å, similar to in the above characterised complex **5**. However, the Ni-N$_{Py}$ bond (1.8249(13) Å) was found to be larger by 0.1 Å than either **5** or **2**. The Ni-N$_{az}$ bond length of 1.8686(14) was within ~ 0.05 Å of the Ni-N$_{NCMe}$ bond of **2**,[52] as well as the complex [Ni(PdmBox)(N$_3$)] with Ni-N$_{az}$ = 1.901 Å,[117] but was significantly shorter than the only other reported square planar Ni-N$_3$ complex [Ni(Me$_3$NN)(N$_3$)(2-pic)] (2-pic = 2-picolylamine) with bond length 1.939(2) Å.[118] The N$_{az(1)}$-Ni-N$_{az(2)}$ bond angles were 128.8(6)° (major moiety) and 134.4(14)° (minor moiety) which compare to 123.8(1)° and 133.03(1)° for the reported complexes [Ni(PdmBox)(N$_3$)] and [Ni(Me$_3$NN)(N$_3$)(2-pic)] respectively. The N-N-N bond angle of the azide moieties for **11** were 172.57(2)° and 174.59(2)° which are approximately linear and are slightly less than those of [Ni(PdmBox)(N$_3$)] and [Ni(Me$_3$NN)(N$_3$)(2-pic)] with 175.0(2)° and 177.3(2)° respectively.[117,118] In general, Ni-N$_3$ complexes have azide moieties with bond angles in the range of ~175° - 178°.[119–121]

Importantly, there was also a weak intramolecular interaction between an iPr methyl proton and N$_{az(2)}$, with a distance of 2.757(3) (major) and 3.094(4) Å (minor) respectively for the two azide moieties (Fig. 24). As the azide unit was a structural mimic for an oxygen adduct, this implicated the methyl proton in the oxidation reaction proposed to be carried out by a transient Ni^{II}-superoxide species, **6**, leading to **9a**. While this complex was found to have a hydroxylated methine proton, a HAT reaction by an electrophilic Ni^{II}-superoxide would lead to a radical present on a primary carbon, which could then undergo radical migration to the methine carbon, a tertiary carbon, wherein the radical is more stable (see section 2.2.8).

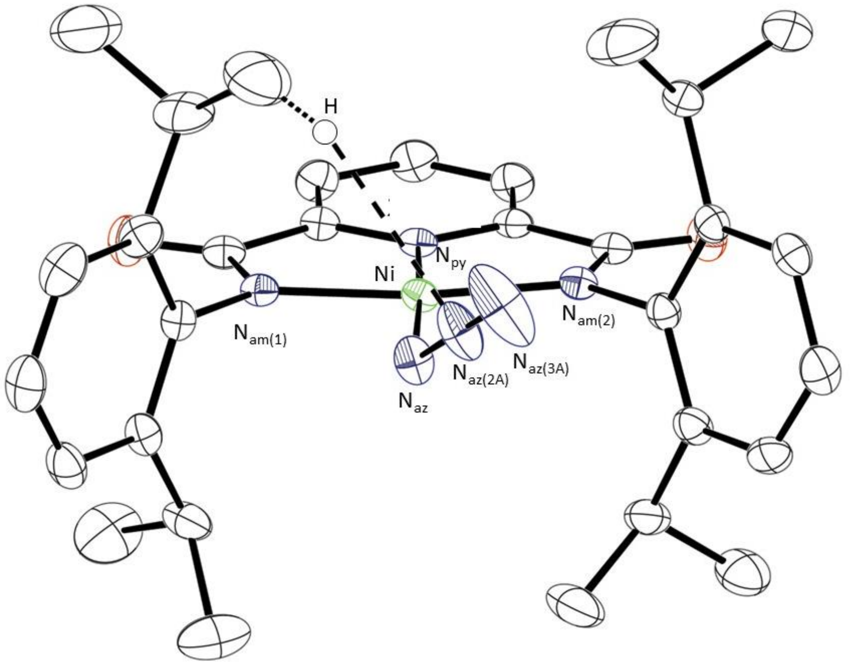

Figure 24. Molecular structure of $[Ni^{II}(PyN_2^{iPr2})(N_3)]^-$ showing the C-H-N$_{az}$ interaction. The azide moiety was disordered over two positions (26:74) with the major moiety shown. Solvent residues, protons and counterions are omitted for clarity. Thermal ellipsoids shown at 50 % probability.

Table 11. Major structural parameters of $[Ni^{II}(PyN_2^{iPr2})(N_3)]^-$. In relation to the azide moiety, A and B refer to the two disordered units.

Parameter	Length (Å) or angle (°)
Ni-N$_{am(1)}$	1.8997(14)
Ni-N$_{am(2)}$	1.9119(14)
Ni-N$_{az}$	1.8686(14)
Ni-Np$_y$	1.8249(13)
Ni-N$_{az}$-N$_{az(2A)}$	128.8(6)
Ni-N$_{az}$-N$_{az(2B)}$	134.4(14)
N$_{az}$-N$_{az(2A)}$-N$_{az(3A)}$	174.59(2)
N$_{az}$-N$_{az(2B)}$-N$_{az(3B)}$	172.57(2)

IR spectroscopy showed an intense azide stretch at 2090 cm^{-1} (Fig. S20). Negative mode ESI-MS showed a mass peak at m/z = 583.2305 ($[Ni^{II}(PyN_2^{iPr2})(N_3)]^-$, calc. $C_{31}H_{37}N_6NiO_2$ = 583.2331, Fig. S21). The resulting ^{1}H NMR spectrum showed peaks corresponding to the pyridine dicarboxamide ligand only (Fig. 25). The isopropyl methyl groups were present as two inequivalent doublets at 1.05 and 1.34 ppm respectively, as is common with such Ni^{II} complexes of this ligand family,[52] while the methine protons were seen as a multiplet at 3.73 ppm. The aromatic signals were found in the range of 6.80 - 8.15 ppm.

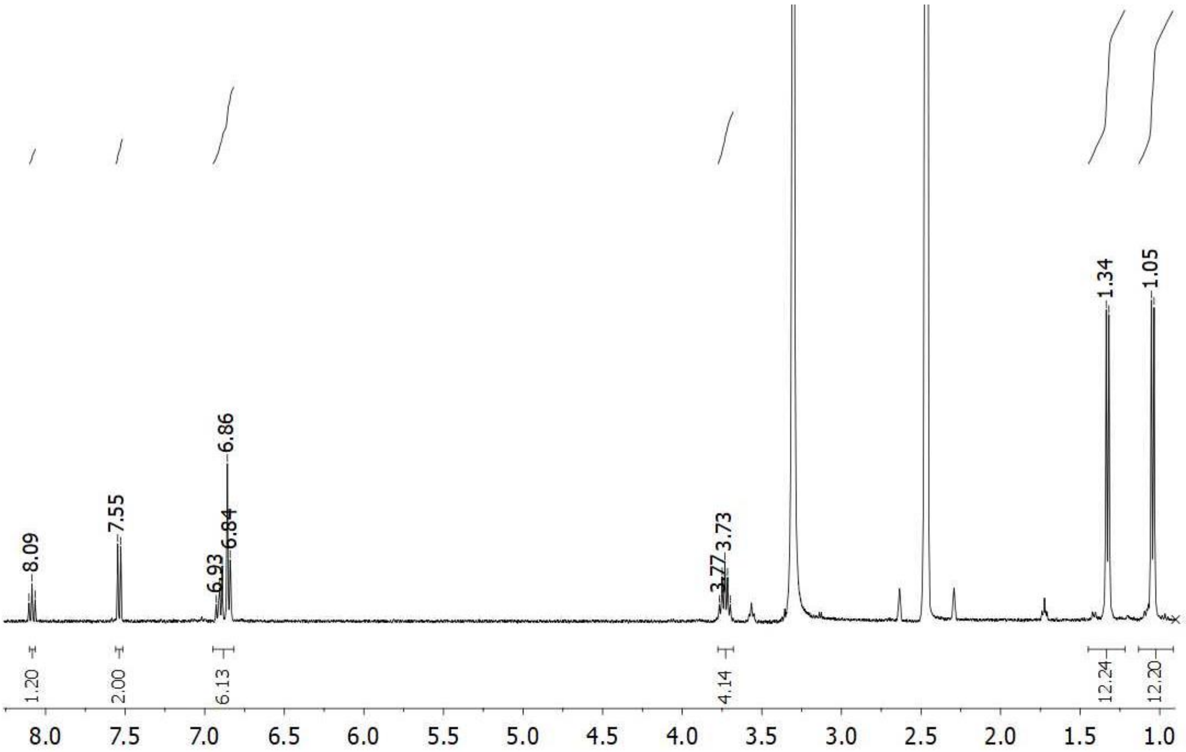

Figure 25. ^{1}H NMR spectrum of **11** in DMSO-D$_6$. Solvent peaks: 2.5 (DMSO), 3.33 ppm (H_2O).

2.2.8 Proposing a mechanism for the reaction of $[Ni^{II}(PyN_2^{iPr2})(NCMe)]$ with KO_2

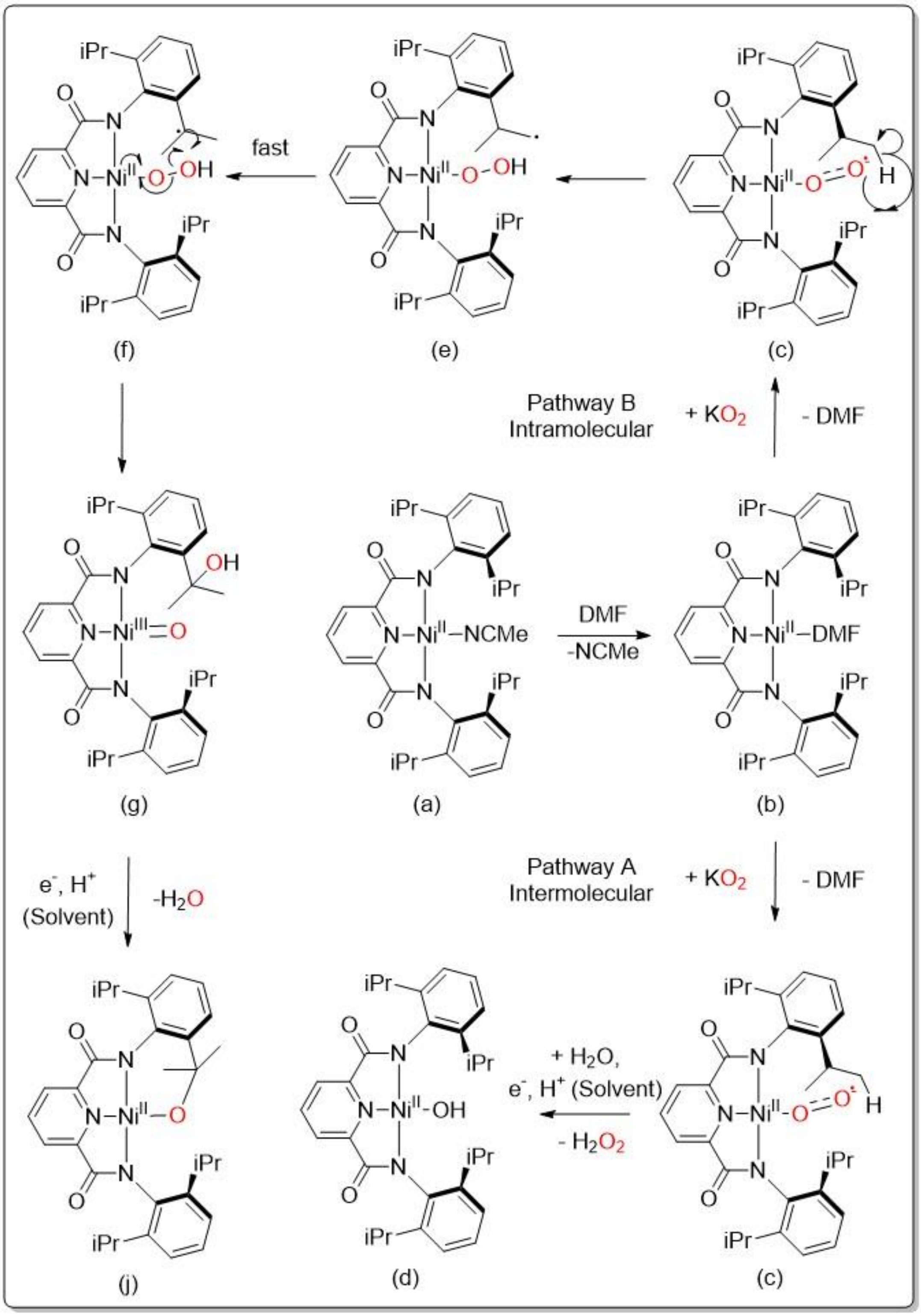

Scheme 12. Proposed mechanism for the reaction of **2** to form **7a** (Pathway A) and **9a** (Pathway B).

The proposed reaction mechanism has two possible paths, pathway A for the formation of **7a** and pathway B for the formation of **10a** (Scheme 12). Initially, dissociation of the NCMe ligand occurs with concomitant coordination of a DMF molecule (Scheme 12 (b)). In both pathways A and B, the reaction of **2** with KO_2 leads to the formation of **6** (Scheme 12 (c)). In pathway A, this has been postulated to react with adventitious H_2O (DMF) and a solvent molecule to form **7a**, H_2O_2 (Scheme 12(d)) which then disproportionates to O_2 and H_2O_2. **7a** would then decay to **8a** in the presence of CO_2. As 1 eq. CO_2 was required to react with 1 eq. **7a** (as reported for **7b**) the total volume of CO_2 required was only 6 μL (as calculated by using the ideal gas law), thus the above assumed reactivity was valid.[90]

The lack of a reaction between **7b** with KO_2 and 18-C-6 (section 2.2.6, Fig. S19) suggested that the formation of **10a** was via an independent pathway and was not formed from the reaction of **7a** with KO_2, once formed. Thus, conversely in pathway B, an intermolecular hydrogen atom abstraction mechanism occurs to cleave a methyl C-H bond from the iPr group of the ligand, based on the structural information inferred from the structure of **11**, and a Ni^{II}-hydroperoxide (Scheme 12(e)). Rearrangement of the radical forms the more stable methine radical which undergoes radical rebound with the Ni^{II}-hydroperoxide (Scheme 12(f)), as in the catalytic cycle of IPNS.[2,10] The formed Ni^{III}=O complex (Scheme 12(g)) then decays by reaction with a solvent molecule, with deprotonation of the hydroxide group to form H_2O and the hydroxylated product (Scheme 12(h)).

It must be noted that McDonald and co-workers postulated the presence of **10a** as an intermediate which lead to the formation of a benzo-1,3-oxazine ring system.[88] Their study in question detailed the suggested mechanism of a Ni^{III}-$O^{\bullet}$ complex (with no hydroxyl group inserted into the ligand) which likewise underwent abstraction of a proton from the iPr group of the bound pyridine dicarboxamide ligand. Theoretical studies suggested cleavage occurred at the methine position, rather than the proposed methyl position followed by rearrangement as suggested in this study.[88] As no complex bearing a benzo-1,3-oxazine ring was found in this study, either by ESI-MS or post-reaction acidified workup, the formation of a Ni^{III}-$O^{\bullet}$ in the absence of a hydroxyl group at the methine position was excluded from considerations in the catalytic cycle.

2.2.9 Conclusions

The aims of this work were to isolate and characterise a variety of metal-superoxide complexes and to examine their reactivities towards different types of substrates. Although this ultimate goal was not achieved, a number of important results were obtained.

The syntheses of two novel Fe^{II} complexes, **3** and **4a** were carried out under anaerobic conditions. **3** was characterised by ^{1}H NMR, IR and UV-vis spectroscopies, ESI-MS and XRD. This complex was identified as both the first dinuclear Fe_2 complex bearing this family of pyridine dicarboxamide ligands, and also the first non-ruthenium complex wherein the ligand was bound as the imidate isomer. **4a** was characterised by ^{1}H NMR, UV-vis and IR spectroscopies as well as mass spectrometry. ESI-MS carried out with a solution of **4a** in DMSO allowed the identification of the DMSO adduct, **4b**. ^{1}H NMR spectroscopy yielded a spectrum with 10 paramagnetic signals, which was as expected, 7 signals corresponding to the ligand and 3 signals from the bound DMF adduct. Unfortunately, structural characterisation was not possible and so the binding mode of the ligand was not determined.

It was observed by UV-vis spectroscopy that dissolution of **2** in DMF led to the loss of the NCMe residue and association of a DMF molecule in its place. **5** was characterised by ^{1}H and ^{13}C NMR, IR and UV-vis spectroscopies as well as by XRD. With the aim to isolate **6**, to a DMF solution of **2** was added KO_2 and 18-C-6 leading to the formation of new features in the UV-vis absorption spectrum at λ_{max} = 310, 375 and 470 nm, which were strikingly similar to the previously reported **8b** with λ_{max} = 306, 369 and 475 nm. ESI-MS identified a short-lived mass peak at m/z = 573.2040 which matched with the mass expected for **6**. Subsequent up-scale replication of the reaction and isolation of the products yielded the complex **7a** under anaerobic conditions which was characterised by ^{1}H NMR and IR spectroscopies as well as ESI-MS and XRD. Interestingly, ESI-MS studies of **7a** suggested the presence of the side-products **9a** and **9b**.

These side products were observed to form over time during time-dependent ESI-MS studies of the post-reaction mixture of **2** and KO_2. Acidified workup of the post-reaction mixture led to an organic solid which was a mixture of two compounds, **1** and **10a**, formed from the demetallation of **7a** and **9a** respectively. These Ni^{II} complexes were proposed to form via **6** by intermolecular reaction with adventitious water and through an electrophilic intramolecular hydrogen atom abstraction of the bound pyridine dicarboxamide ligand respectively.

In this way, the proposed mechanism for the intramolecular oxidation of the ligand iPr group mimics that of the initial steps of the IPNS enzymatic cycle, which leads to cleavage of a C-H bond by a proposed electrophilic Fe^{III}-superoxide intermediate. This is one of only a handful of studies which implicate a Ni^{II}-superoxide as the active oxidant and the results herein highlight the importance of using a robust ligand framework which can withstand the oxidising potential of such reactive intermediates. This is in stark contrast to the reported Cu^{II}-superoxide complex, $[Cu(PyN_2^{iPr2})(O_2)]^-$ which was isolatable at cryogenic temperatures and did not lead to ligand oxidation.[40]

2.2.10 Future Work

In terms of the Fe^{II} syntheses discussed above, further attempts at crystallisation of **4a** should be carried out in order to determine its structure and thus the coordination environment of the metal. Upon structural characterisation, the reactivity of both **3** and **4a** with O_2 should be examined at cryogenic conditions in order to isolate potential Fe^{III}-superoxide adducts. Potential reactive intermediates would be identified initially by changes in the electronic absorption spectrum, with the presence of isosbestic points suggesting full conversion of the starting material. The stability of these species would then be investigated by varying the temperature of formation and identifying the ideal conditions for their yield. Their properties would be probed by kinetic studies using both electron rich and electron poor substrates, and also through a variety of spectroscopic techniques such as Mössbauer, EPR, XAS and rR spectroscopies, as well as cold-injection ESI-MS. The identification of intramolecular oxidation of the ligand would also be investigated based on the final decay products.

In light of the above results for the reactivity of KO_2 and **2**, a number of further studies should be carried out in order to gain a better determination of the reaction mechanism for the formation of the two Ni^{II} products. The addition of KO_2 to a solution of **2** under anaerobic conditions, which is monitored by electronic spectroscopy, should be carried out in order to clarify the prerequisite formation of **7a** prior to its reaction with atmospheric CO_2 to yield **8a**. Addition of a solution of labelled $K^{18}O_2$ should also be carried out in similar conditions and frozen ESI-MS should be carried out in order to determine the source of the hydroxide oxygen, either from KO_2 or adventitious H_2O

within the solvent. Likewise, addition of KO_2 to a DMF solution of **2** in the presence of minor concentrations of H_2O and $H_2{}^{18}O$ should be carried out in conjunction with ESI-MS. Replication of the reaction in DMF-D_7 at low temperatures, comparison of the rates of formation of **7a** and determination of a potential KIE would determine if the solvent was the source of the proton in **7a**.

Upon identification of the source of the hydroxide's oxygen, similar studies should be carried out so as to understand the source of the hydroxide's oxygen atom in **10a**. Addition of KO_2 to a DMF solution of **7a** did not lead to formation of **9a**, thus the incorporated hydroxide source must originate from either an independent source to **7a** or via a different reaction pathway, as suggested.

2.3 X-ray Absorption Spectroscopy

XANES and EXAFS have been used to gain electronic and structural insights into a variety of metastable species synthesised in concentrations of a few millimoles. The compounds described within this section were synthesised by other members of the McDonald lab, however, all XANES and EXAFS experiments were conducted and analysed by this author. Herein, a description of these studies will be discussed. The results of section 2.3.1 are adapted from *Angew. Chem. Int.Ed., 2019, 58, 5718 –5722*, with permission from the authors.

2.3.1 XANES analysis of $[Mn_2(BPMP)(O_2)]^{2+}$

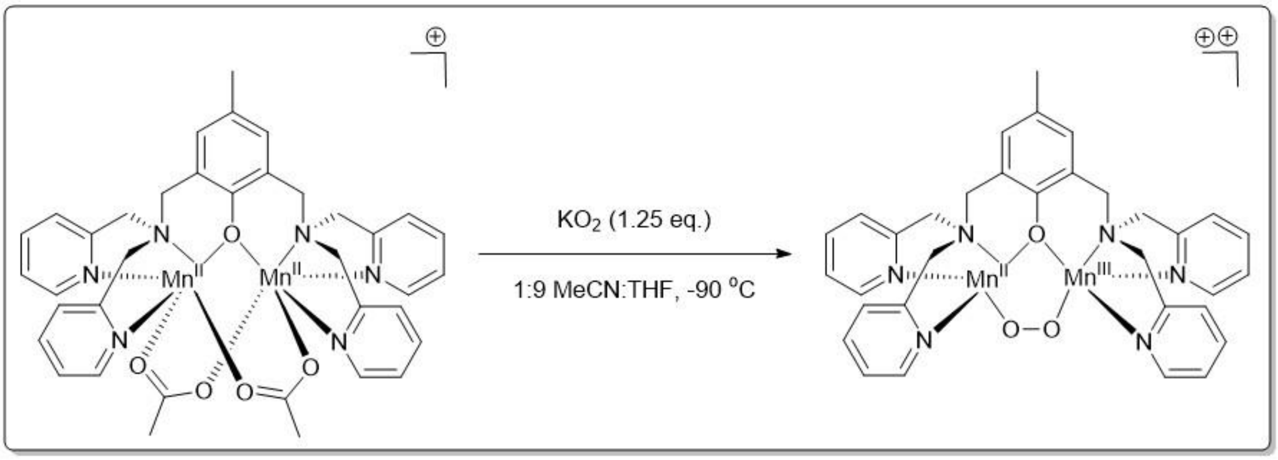

Scheme 13. Formation of **12b** from the reaction of **12a** with KO_2

The reactivity of complex ($[Mn^{II}_2(O_2CCH_3)_2(BPMP)](ClO_4)$ (**12a**, where HBPMP = 2,6-bis[(bis(2-pyridylmethyl)amino)methyl]-4-methylphenol))) towards KO_2 was investigated at -90 °C, generating a metastable species, **12b** (Scheme 13). This was characterised by UV-vis spectroscopy (λ_{max} = 400 - 500 and 550 - 650 nm), cold injection ESI-MS (m/z = 770.2933, the mono-cation $\{[Mn_2(O_2)(BPMP)](ClO_4)\}^+$ and EPR (a 22 line signal corresponding to an S = 1/2 $Mn^{II}Mn^{III}$ species). Taken together, the spectroscopic data suggested the formulation of a mixed valent $Mn^{II}Mn^{III}$-peroxide species.[122]

To gain an insight into the structure of **12b**, Mn K-edge X-ray absorption near edge spectroscopy (XANES) was carried out on frozen samples of **12a** and **12b**. The edge energy of **12a** was found to be 6548.4 eV, while that of **12b** was 6548.9 eV, an increase of 0.5 eV (Table 12, Figures 26, S22). Systematic studies of Mn coordination compounds have shown that each integer change in formal oxidation state elicits a blue-shift of 2-4 eV in K-edge inflection energy.[85,123,124] For a mixed valent Mn_2 species, a shift of 1 eV would therefore be expected upon quantitative oxidation of a $Mn^{II}Mn^{II}$ precursor (**12a**) to a $Mn^{II}Mn^{III}$-peroxide (**12b**) adduct. Here, the yield of 1**2b** was only ~50%, according to EPR analysis, consistent with the observed blue-shift of 0.5 eV. For the previously reported peroxide complex $[Mn_2(N\text{-}Et\text{-}HPTB)(O_2)]^{2+}$ (**13b**, where N-Et-HPTB= N,N,N',N'-tetrakis(2-(1-ethylbenzimidazolyl))-2-hydroxy-1,3-diaminopropane)) an ~1 eV shift was observed upon conversion of the Mn^{II}_2 starting material to the $Mn^{II}Mn^{III}$ species $[Mn_2(N\text{-}Et\text{-}HPTB)(O_2)]^{2+}$ (obtained in 80% yield, Figure S23).[125]

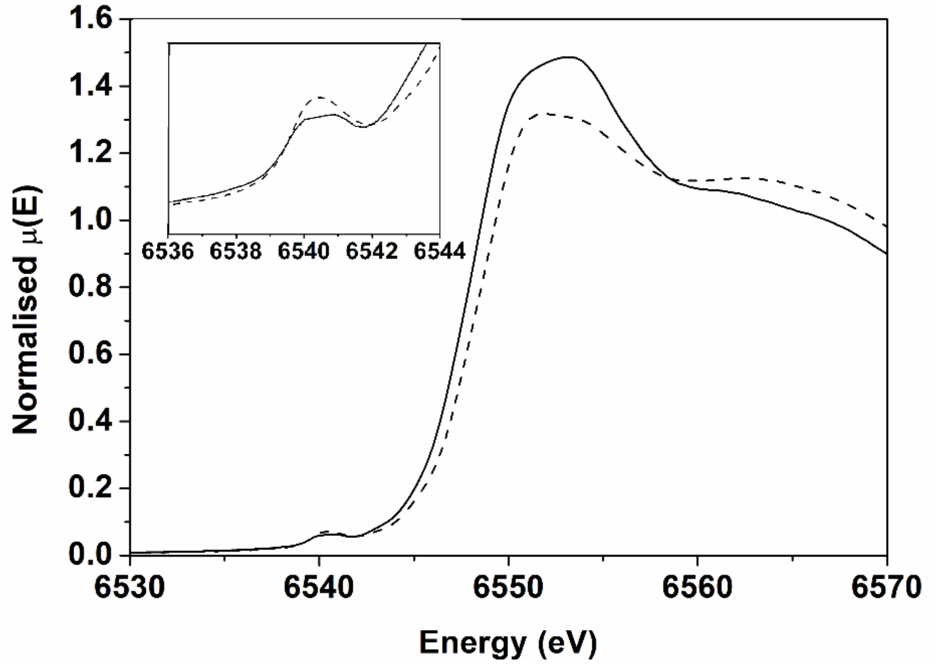

Figure 26. Normalised XANES spectra if **12a** (solid trace) and **12b** (dashed trace). The inset shows an expansion of the pre-edge region

Notably, there was a significant increase in the pre-edge area from 5.8 to 9.4 units upon conversion of **12a** to **12b**, respectively (Fig. 26 (inset), 27, Table 12). The increased pre-edge area was indicative of a decrease in symmetry from octahedral Mn sites in **12a** to a lower degree of symmetry (possibly 5-coordinate Mn site(s)) in **12b**.[124,126] The pre-edge peak of **12a** was constructed of a mixture of two independent peaks at 6540.0 eV and 6540.8 eV respectively (Figs. 27(A), S24, S25). The weighted average of these two transitions gave a pre-edge energy of approximately 6540.3 eV, which was identical to that of **12b** (Table 12). This was not unexpected, as appreciable changes in pre-edge energy are generally not found until the Mn^{IV} state is achieved.[85] It has been shown that octahedral Mn^{II} complexes exhibit two 1s → 3d transitions of similar energy (1s → 3d(e_g) and 1s → 3d(t_{2g})), separated by ~ 0.8 – 1 eV.[124,127] It was assumed that the two features observed derived from the octahedral nature of the Mn sites in **12a**. The observation of a loss of asymmetry in the pre-edge feature, upon conversion of **12a** to **12b**, indicated a change in coordination environment at the metals. The loss of an electron, through Mn oxidation, could lead to an increase in the number of vacant valence *d*-orbitals present, thus affecting the 1s → 3d transitions. This would in turn increase the intensity and area of the pre-edge feature, as was observed.[124,126] A comparable change to this was seen by Kovacs, DeBeer, and co-workers, wherein a 5 coordinate starting Mn^{II} complex was oxidised to a 6 coordinate Mn$^{III}_2$-peroxide complex, leading to a decrease in the pre-edge area, providing support for this analysis.[128]

Upon conversion of **12a** to **12b**, there was a significant decrease in the edge maximum intensity (Fig. 26). The intensity of the edge maximum has been reported to vary as a function of the absorber-scatter distances, an increase in the spread of the absorber scatterer distances, a decrease in the site symmetry, leads to a decrease in the intensity of the edge maximum.[129] A Mn^{II}Mn^{III} species would therefore be expected to have an increased edge absorbance maximum absorbance, due to the loss of symmetry upon formation of the mixed valence species.

The shift of the edge energy by 0.5 eV, changes to pre-edge areas and thus decreased site symmetry supported the assignment of **12b** as a Mn^{II}Mn^{III} species. EXAFS analysis on **12b** was not carried out due to its low yield (~ 50%). Based on the spectroscopic results along with ESI-MS evidence, it was concluded that **12b** was a Mn^{II}Mn^{III}-peroxide complex.

Table 12. Tabulated edge and pre-edge energies and pre-edge peak fitting parameters[a]

Sample	**E_{edge} (eV)**	**$E_{pre\text{-}edge}$ (eV)**	**$E_{pre\text{-}edge}$ (eV)[b]**	**height**	**FWHM**	**area**
12a	6548.4	6540.3	6539.94(1)	0.0226(11)	1.18(12)	3.5(5)
			6540.89(4)	0.0164(3)	1.05(6)	2.3(1)
12b	6548.9	6540.3	6540.39(1)	0.0401(6)	1.77(7)	9.4(5)

[a]The values in parentheses correspond to uncertainty in the final digit for each parameter, taken as the standard deviation determined from the four separate fits conducted on each

sample. Areas are multiplied by 100 for convenience. [b] Based on simulations depicted in Figure 27.

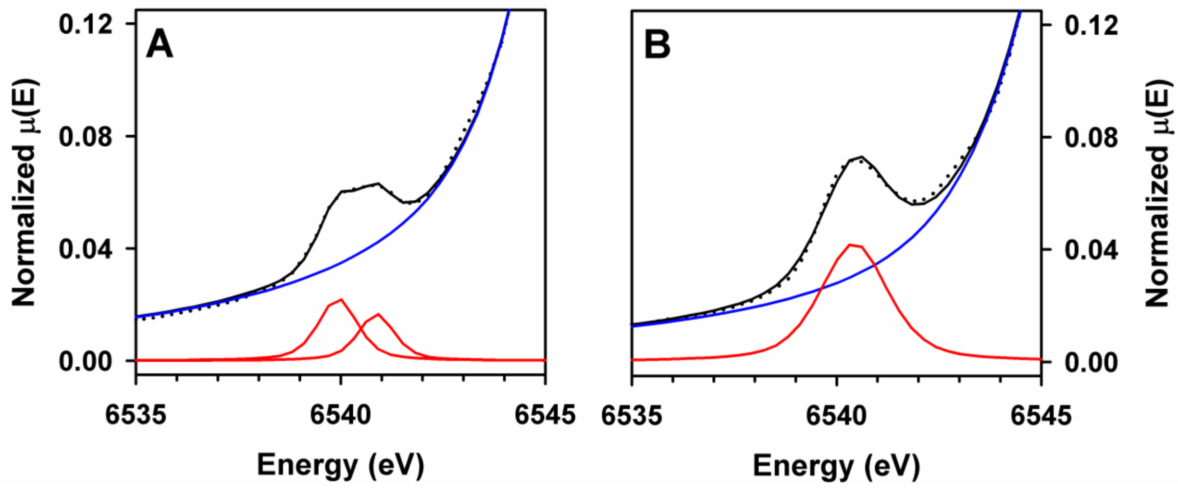

Figure 27. Representative pre-edge peak fits of **12a** (A) and **12b** (B). The experimental data was shown as dots, the background function as a blue line, the component pre-edge functions as red lines, and the sum of the background + component functions as a solid black line

2.3.2 EXAFS analysis of $[Mn_2(N\text{-}Et\text{-}HPTB)(O_2)]^{2+}$

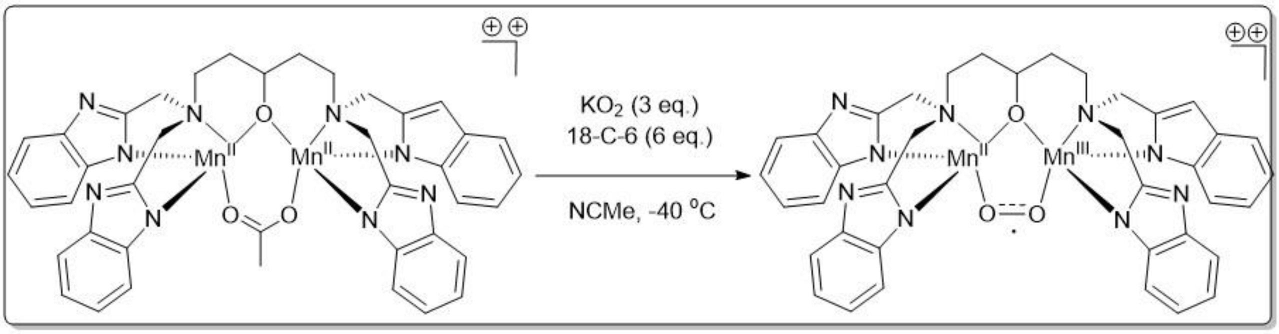

Scheme 14. Oxidation of **13a** to **13b** by reaction with KO_2

The reactivity of $[Mn_2(N\text{-}Et\text{-}HPTB)(OAc)](ClO_4)_2$,**13a**, towards KO_2 was investigated at -40 °C in NCMe (Scheme 14). This generated a metastable species, **13b**, which has been characterised by UV-vis spectroscopy (λ_{max} = 460 and 610 nm), cold injection ESI-MS (m/z = 431.54 (KO_2), the dication: $[Mn_2(N\text{-}Et\text{-}HPTB)(O_2)]^{2+}$, m/z = 433.48 ($K^{18}O_2$), the dication: $[Mn_2(N\text{-}Et\text{-}HPTB)(^{18}O_2)]^{2+}$), EPR (29 line signal at 2K corresponding to an S = ½ $Mn^{II}Mn^{III}$ with hyperfine interactions between the inequivalent Mn ions) and XANES (a blue shift in the edge energy of 1 eV upon conversion of **13a** to **13b** corresponding to a half-integer change in the average Mn oxidation state).[125] Thus, from the above data, it was surmised that the intermediate **13b** was a $Mn^{II}Mn^{III}$ intermediate.

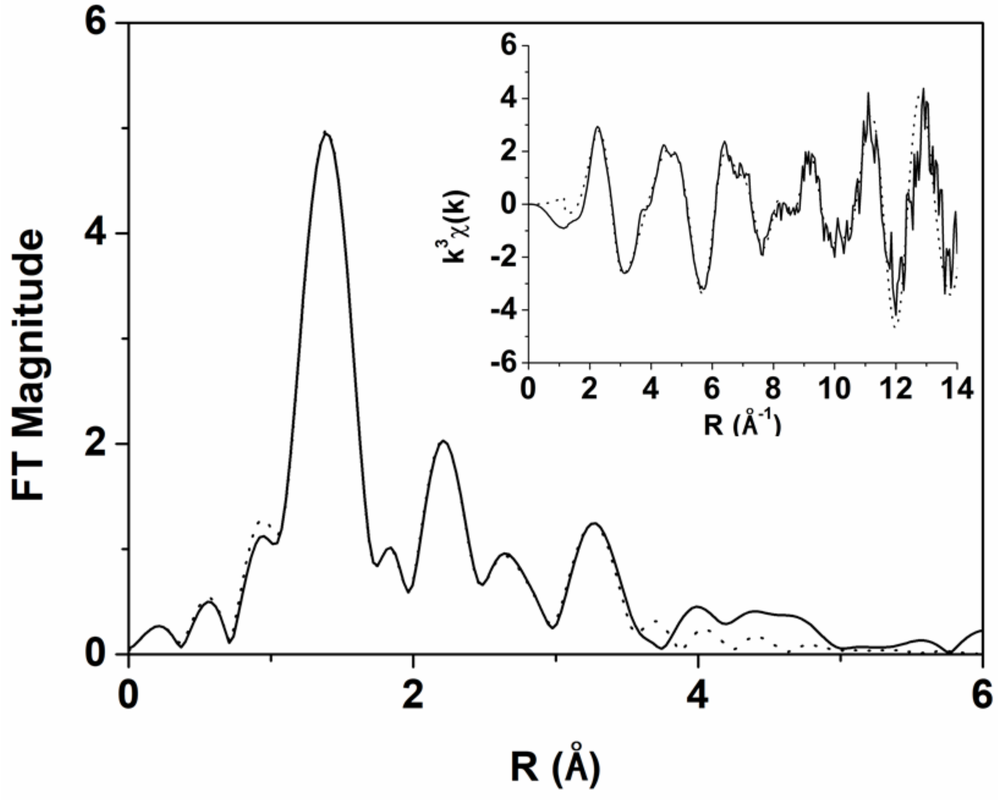

Figure 28. Representative best fits (Fit 15 in Table S3) to k^3-weighted EXAFS data of **13b**. Experimental data shown as a black trace, while the best fit was represented as a dotted trace.

Extended X-ray absorption fine structure (EXAFS) analysis was carried out on both **13a** and **13b** (Fig. 28 and S26) in order to gain structural data on **13b**. The best fit for **13a** was found with 2 N/O scatterers at 2.04 Å, one oxygen of the bound acetate, and one oxygen from the bridging alkoxide of the ligand, 2 N/O scatterers at 2.15 Å, the benzimidazole nitrogens of the ligand, 1 N/O scatterer at 2.42 Å, the amine nitrogen of the ligand, 2 C scatterers at 2.99 Å, 3 C scatterers at 3.18 Å, all from the bound ligand and acetate and 1 Mn scatterer at 3.61 Å. This data matched quite well with that obtained from the single crystal XRD (Table 13). However, there were a total of 9 carbon atoms present at distances of between 2.9 – 3.3 Å found in the single crystal XRD structure, whereas only 5 were modelled in the EXAFS analysis. However, the accuracy of EXAFS analysis decreases with distance from the absorbing nuclei, especially for small nuclei such as carbon, thus this was not assumed to be a problem.

Similarly, the best fit for **13b** was found with 2 N/O scatterers at 1.91 Å, presumably one atom of a bound peroxide and one atom of the bridging alkoxide ligand, 2 N/O scatterers at 2.13 Å, the benzimidazole nitrogens of the ligand, 1 N/O scatterer at 2.40 Å, the amine nitrogen atom of the ligand, 2 C scatterers at 2.98 Å, 3 C scatterers at 3.18 Å, all from the bound ligand and 1 Mn scatterer at 3.59 Å.

Table 13. Comparison of XRD and EXAFS distances of **13a** and **13b**. N_{benz} refers to the benzimidazole nitrogens of the ligand, N_{am} refers to an amine nitrogen, O refers to an alkoxide or acetate/peroxide oxygen.

Metal-scatterer	XRD **13a**	EXAFS **13a**	EXAFS **13b**
Mn-O	2.053(4)	2.04	1.91
Mn-N_{benz}	2.132(8)	2.15	2.13
Mn-N_{am}	2.410(3)	2.42	2.40
Mn-N_{am2}	1.922(3)		
Average Mn-C (< 3 Å)	2.977 (7)	2.99	2.98
Average Mn-C (> 3 Å)	3.190(11)	3.18	3.18
Mn-Mn	3.603(7)	3.61	3.59

When comparing the bond lengths of the **13a** to **13b**, it was observed that there was a drastic decrease in the initial Mn-O bond lengths. This was attributed to the coordination of a peroxide moiety in **13b** in place of the acetate ligand in **13a** as well as an increase in the average oxidation state, and thus positive charge of the Mn ions. Mononuclear side-on bound Mn^{III}-peroxide species have been shown to have Mn-O bond lengths in the region of 1.838 – 1.901 Å.[130–135] No structural studies of bridging Mn_2-peroxide complexes are known. Thus, the Mn-O bond length of 1.91 Å would match well with that expected of a dinuclear $Mn^{II}Mn^{III}$-peroxide complex, as the lower average oxidation state of 2.5 would lead to longer bond lengths of the Mn-O bond, relative to the Mn^{III} state, and also incorporates the alkoxide atom of the ligand, which has also been much reduced relative to **13a**.
The remaining first coordination sphere bonds lengths (Mn-N_{benz} and Mn-N_{am}) were also slightly reduced, which likewise has been attributed to a change on the average oxidation state of the Mn ions and/or coordination of the peroxide moiety. The Mn-C scatterer distances found between 2.9 – 3.2 Å were approximately unaffected by changes in the

oxidation state, while there was a slight reduction in the Mn-Mn separation by 0.02 Å upon oxidation of **13a** to **13b**. Previously structurally characterised $Mn^{II}Mn^{III}$ species have been shown to exhibit Mn-Mn distances of 3.084 – 3.472 Å.[136–140] For both **13a** and **13b**, this distance was significantly larger and was proposed to be due to the bridging acetate and peroxide moieties respectively, as well as the nature of the rigid ligand system, leading to a relative increase in the Mn-Mn separation.

Thus, the significant reduction in bond length of the average Mn-O bond has been suggested to be caused by a combination of an increase in oxidation state as well as a change in the bound ligand (acetate in **13a** to peroxide in **13b**). The results of the EXAFS analysis coincide with that from the previously reported spectroscopic data and provides precedent for a retention of the coordination geometry around the Mn ions upon oxidation of **13a** to **13b**.

2.3.3 XANES and EXAFS analysis of $[Cu^{III}(PyN_2^{iPr2})(OAc)]$

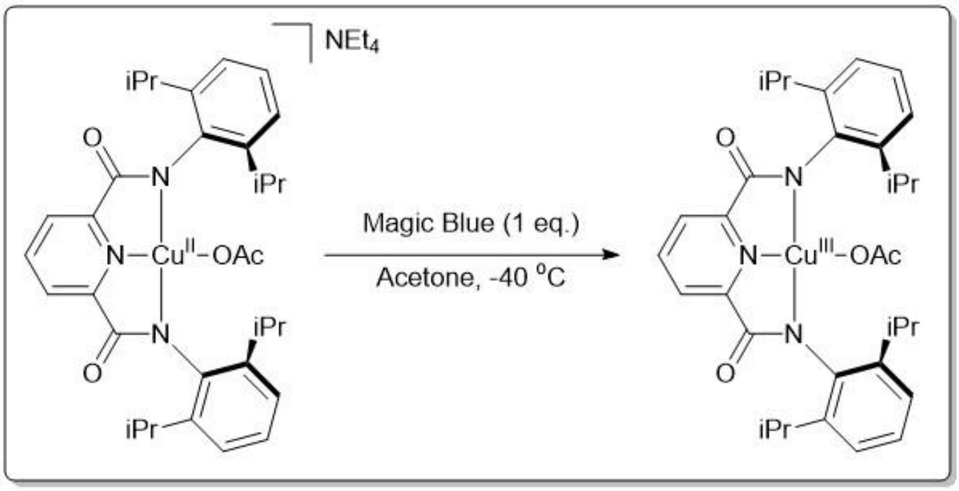

Scheme 15. Oxidation of **14a** to **14b**

The oxidation of $NEt_4[Cu^{II}(PyN_2^{iPr2})(OAc)]$, **14a**, using the one-electron oxidant tris(4-bromophenyl)ammoniumyl hexachloroantimonate, (magic blue) at -40 °C yielded the new intermediate $[Cu^{III}(PyN_2^{iPr2})(OAc)]$ (**14b**, Scheme 15). **14b** was characterised by UV-vis (λ_{max} = 630, 805 nm) and EPR (S = 0 (silent) with residual 9 % S = ½ Cu^{II} remaining) spectroscopies. Thus, K-edge Cu XANES and EXAFS studies were carried out to gain structural and electronic symmetry information insight into **14b**.

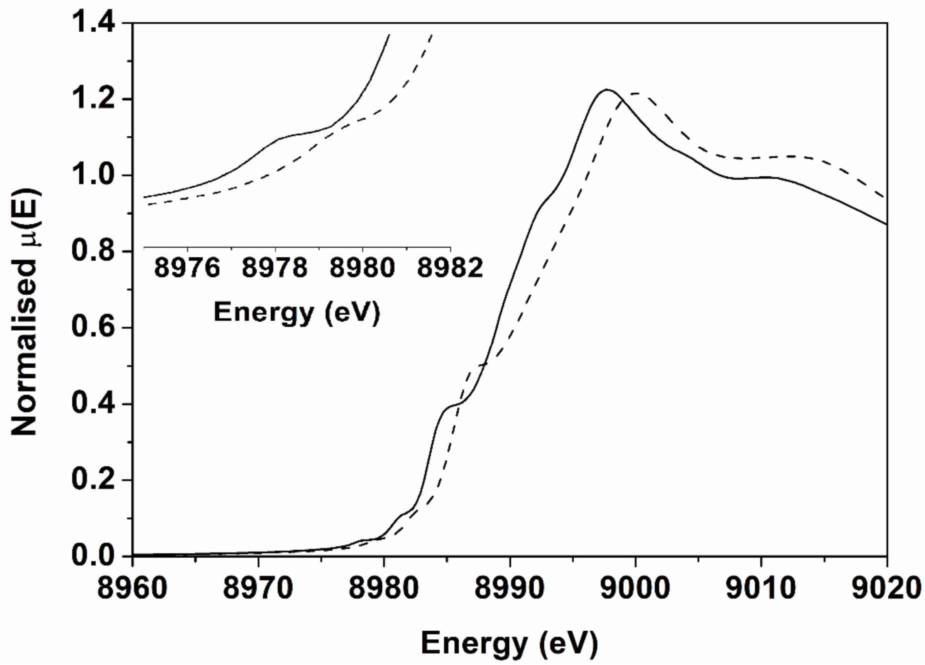

Figure 29. Normalised Cu K-edge spectrum of **14a** (solid trace) and **14b** (dashed trace). Inset: expanded pre-edge region showing ~1.3 eV shift.

14a displayed a pre-edge transition centred at 8978.1 eV, while **14b** had an equivalent peak at 8979.4 eV, approximately 1.3 eV higher in energy (Figures 29, S27, Table 14).[141–144] These pre-edge transition energies fell within the expected range for Cu^{II} and Cu^{III} complexes, respectively, and have been assigned to 1s → 3d transitions.[142,145],[1] The 1.3 eV blue shift suggested an integer change in the oxidation state of the metal (thus Cu^{II} to Cu^{III} oxidation).[141,144,146–148] Along the rising edge, there was a transition visible at 8984.3 eV and 8986.7 eV for **14a** and **14b**, respectively (Figure S28), that has been previously ascribed to a 1s → 4p + LMCT "shakedown" feature. For **14a**, a further 'main' transition was found at 8992.3 eV, which was not seen in **14b** (Figure S29), which was assigned to a 1s → 4p excitation based on previous observations.[142] The ratio of the main/shakedown second derivative peaks were 4.4 and ~ 0 for **14a** and **14b** respectively.[2] It was previously observed that, for a Cu^{II}/Cu^{III} pair, the ratio of the intensities of the

---

[1] As the copper foil reference for these measurements was calibrated to 8979 eV, as opposed to the conventional 8980.3 eV, this causes all of the values to be red-shifted by 1.3 eV. Hence, if the reference foil had been set at 8980.3 eV, as is convention, the values obtained for the pre-edge would be 8979.4 eV for **14a** and 8980.7 eV for **14b**. This is within the average range of 8979 (± 0.4 eV) for Cu^{II} and 8981 (± 0.5 eV) for Cu^{III}.

[2] as **14b** does not have an observable 1s → 4p main peak, the numerator approaches zero in the fraction, leading to an overall value of ~ 0.

second derivative peaks for the 1s → 4p main/1s → 4p plus shakedown transitions were found to be ≥ 1 for a Cu^{II} complex, and then ≤ 1 for the corresponding Cu^{III} complex, as was observed for **14a**/**14b**, supporting the assignment of **14b** as containing a Cu^{III} ion.[144] The pre-edge features had the same normalised intensity for both **14a** and **14b**, suggesting that there had not been a change in geometry or coordination number, as altering the geometry, and hence the degree of 3d/4p mixing, would change the intensity of this feature.[144] Also, the shape of the rising edge maximum has been postulated to be a consequence of multiple scattering effects which are dependent on the local geometry around the scattering atom.[144] The rising edge maximum energy was blue-shifted due to the increase in the oxidation state of **14b** relative to **14a**, however, the shape was unaffected, indicating a retention of geometry within the first coordination sphere.

Table 14. Edge and pre-edge region transitions and energies (eV) for **14a** and **14b**.

	1s → 3d	1s → 4p + shakedown	1s → 4p main	Main/shakedown
14a	8978.1	8984.3	8992.3	4.4
14b	8979.4	8986.7	-	~ 0
change	1.3	2.4	-	-

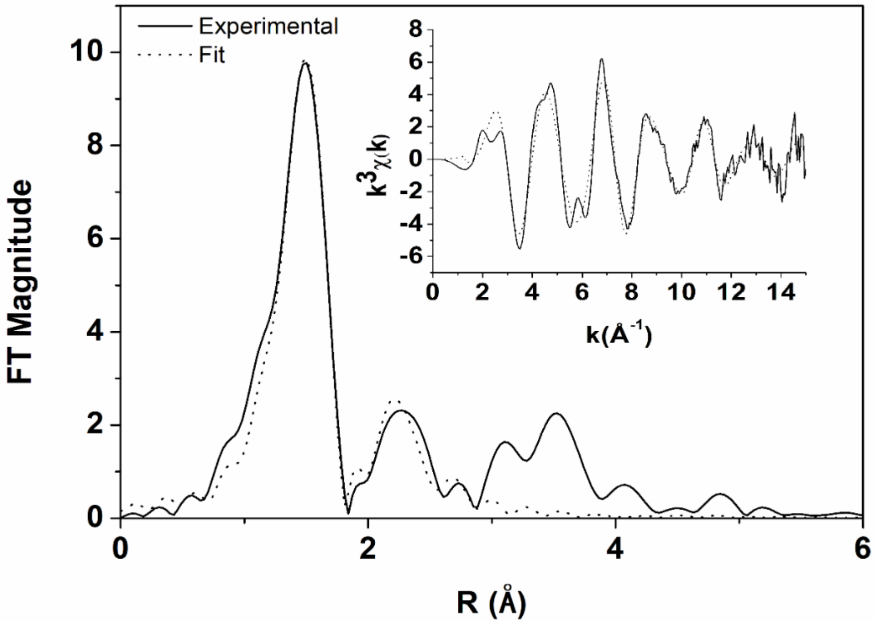

Figure 30. Representative best fits (Fit 7 in Table S5) to k^3-weighted EXAFS data of **14b**. Experimental data shown as a black trace, while the best fit was represented as a dotted trace.

Extended X-ray absorption fine structure (EXAFS) analysis was carried out for both **14a** and **14b** (Figures 30, S30). The best fit for **14a** was found with 4 N/O scatterers at 1.96 Å, 2 amide and one pyridine nitrogen of the pyridine dicarboxamide ligand and one oxygen atom from the monodentate acetate, 1 C scatterer at 2.51 Å, from the bound acetate, and 4 C scatterers from the carboxamide backbone at 2.85 Å (Fig. S30, Fit 8 of Table S4). This data matched well with the single crystal XRD data of the complex (Table 15). Similarly, the best fit of the data for **14b** was obtained with 4 N/O scatterers at 1.88 Å, 2 amide and one pyridine nitrogen of the pyridine dicarboxamide ligand and one oxygen atom from the monodentate acetate, 1 C scatterer at 2.38 Å from the bound acetate (the metal-scatterer distance was too long to be a Cu-O bond by the oxygen of the acetate, Cu-O covalent interaction limit is 1.98(6) Å),[149] and 4 C scatterers at 2.76 Å from the pyridine dicarboxamide backbone (Table 15).

Table 15. Comparison of XRD and EXAFS distances of **14a** and **14b**. N_{py} refers to pyridine nitrogen of the ligand, N_{am} refers to an amide nitrogen, O_{Ac} refers to an acetate oxygen, C_L refers to closest carbons of the pyridine dicarboxamide ligand.

Metal-scatterer	XRD **14a**	EXAFS **14a**	EXAFS **14b**
Cu-O_{Ac1}	1.93(4)		
Cu-N_{am1}	1.97(3)		
Cu-N_{py}	2.002(3)		
Cu-N_{am2}	1.922(3)		
Average Cu-O/N	1.959(3)	1.96	1.88
Cu-C	2.550(9)	2.51	2.38
Cu-O_{Ac2}	2.585(4)		
Average Cu-C_L	2.776(9)	2.85	2.76

When comparing the EXAFS data of **14a** to **14b**, the average bond lengths of the first coordination sphere metal-scatterer distances decreased by 0.08 Å (Table 15). This was attributed to an increase in the oxidation state, and thus positive charge, at the Cu atom. The scatterer at 2.38 Å was assumed to be the carbonyl carbon of the acetate, as the scattering interaction mimics that of **14a**, but with a shorter metal-scatterer distance. Also, the metal-scatterer distance was largely above the limit of a Cu-O covalent interaction, 1.98(6) Å, removing the possibility of a bidentate acetate binding mode in **14b**.[149] From the XANES and EXAFS data, **14b** was assigned as the one-electron oxidised equivalent of **14a**, with retention of the square planar geometry around the absorbing nucleus.

2.3.4 XAS Conclusions

XAS was used for the characterisation of 3 unstable intermediates which were synthesised by another member of the McDonald group, but analysed using XANES and/or EXAFS by this author. The reaction of **12a** with KO_2 at -90 °C yielded **12b** which was determined to be a mixed valent $Mn^{II}Mn^{III}$ species due to the blue shift of the edge energy by 0.5 eV (50% yield of **12b**) in the XANES spectrum. There was a change in the pre-edge area symmetry of compounds **12a** and **12b** which was indicative of a change in geometry also, a change from 6-coordinate Mn to 5-coordinate Mn. Similarly, the reaction of **13a** with KO_2 at cryogenic temperatures yielded **13b** which had previously been characterised as a $Mn^{II}Mn^{III}$ species using XANES. EXAFS showed that **13b** was composed of a coordination sphere mimicking that of **12b** but with a significant decrease in the Mn-O bond lengths due to oxidation, as well as other first coordination sphere Mn-ligand bonds and the Mn-Mn distance. This analysis matched well with previous spectroscopic characterisation of **13b**. The oxidation of **14a** with magic blue at cryogenic temperatures yielded **14b**, a Cu^{III} complex as determined by the 1.3 eV blue shift of the pre-edge absorption band in the XANES spectrum and the change in relative intensities of the 1s → 4p transition peaks along the rising edge. Furthermore, EXAFS analysis showed the average Cu-N/O ligand bond distances to decrease from **14a** to **14b** by 0.13Å due to the higher oxidation state of the metal centre.

Thus, the use of XANES and EXAFS spectroscopies allowed the oxidation state and electronic symmetry of compounds **12a**, **13a** and **14a** to be determined.

3. Experimental

3.1 General

Physical Methods. ^1H and ^{13}C NMR and correlation spectroscopy was performed on a Bruker Avance III 400 MHz instrument (400.13 MHz for 1H NMR and 100.61 MHz for 13C NMR) or a Bruker Avance III 600 MHz. ESI-MS were obtained using a micromass time of flight spectrometer (TOF), interfaced to a Waters 2690 HPLC, or by direct injection in the mass spectrometry instrument. ATR-FTIR were recorded using a Perkin-Elmer Spectrum 100 Fourier Transform infrared spectrometer. Electronic absorption spectra were recorded in quartz cuvettes on a Hewlett Packard (Agilent) 8453 diode array spectrophotometer (190-1100 nm range) coupled to a liquid nitrogen cooled cryostat from Unisoku Scientific Instruments (Osaka, Japan~~)~~.

Materials. All reactions with air sensitive materials were conducted in a glove box under an N_2 atmosphere or under an inert atmosphere using standard Schlenk techniques. All reagents and solvents were purchased from commercial sources. Anhydrous DMF was purchased and used without further purification. Anhydrous THF, MeCN, and Et_2O were dispensed through an Innovative Technology PureSolvEN solvent purification system and deoxygenated by purging with Ar.

X-ray absorption spectroscopy methods: The Mn-K-edge X-ray absorption data were collected on beamline 7-3 of the Stanford Synchrotron Radiation Lightsource (SLAC National Accelerator Lab, Menlo Park, CA, USA). Data were collected with the storage ring operating at 3.0 GeV and 500 mA, using a LN_2 cooled Si(220), $\phi = 90^\circ$ for Mn and $\phi = 0^\circ$ for Cu, double-crystal monochromator, calibrated by using the first inflection point of the metal of interest's foil (Mn = 6539.0 eV, Cu = 8979 eV). The monochromator was detuned by ~50% for higher harmonic rejection. A Canberra 32-element solid state germanium detector was used for fluorescence detection. All the measurements were performed at ambient pressure at ~17 K using an Oxford helium cryostat that was cooled by closed cycle He gas loop. The parameters used for the scans were the following:

- Mn XANES: 10 eV steps/1 second integration time in the pre-edge region, 0.3 eV steps /2 second integration time in the edge, and 0.05k steps in the EXAFS, with integration time increasing in a k^2-weighted fashion from 2 to 4 seconds over the energy range (k_{max} = 12.1k). The total detector counts were typically 3-7k, well within the linear range of the detector electronics

- Mn EXAFS: 10 eV steps/1 second integration time in the pre-edge region, 0.3 eV steps /2 second integration time in the edge, and 0.05*k* steps in the EXAFS, with integration time increasing in a k^2-weighted fashion from 2 to 9 seconds over the energy range (k_{max} = 15.1k).
- Cu EXAFS: 10 eV steps/1 second integration time in the pre-edge region, 0.3 eV steps /2 second integration time in the edge, and 0.05 k steps in the EXAFS, with integration time increasing in a k^2-weighted fashion from 2 to 9 seconds over the energy range ($\mathrm{k}_{\mathrm{max}}$ = 15.1k). The total detector counts were in the range between 10 k – 20 k, well within the linear range of the detector electronics.

Each sample was monitored for photoreduction. Complexes **12b** and **14b** were found to be photoreduced by the X-rays and thus only one scan per spot was performed on each sample to limit the effects on the data. The samples were measured using Delrin ® Mossbauer/XAS cups with sample windows of 4 mm x 10 mm.

Elaboration of the XAS data, including averaging, background removal and normalization, was performed using Athena[150]. Edge energies were unable to be obtained for the copper samples, as is expected for copper samples which have an overlapping 1s to 4p transition in the edge region, preventing the accurate determination of the edge. EXAFS analysis was carried out using Artemis[150], which incorporates the IFEFFIT fitting engine and FEFF6 for *ab initio* EXAFS phase and amplitude parameters. Molecular coordinates from crystal structures were used for FEFF6 input to identify significant paths.

3.2 Synthesis

3.2.1 $H_2PyN_2^{iPr2}$ (1)

The synthesis of **1** was carried out via the reported procedure.[86] 2,6-Pyridinedicarboxylic acid (5g, 30 mmol) was refluxed overnight in $SOCl_2$ (50 mL) to yield 2,6-pyridinedicarboxylic acid chloride which was used without purification. The solvent was removed by distillation using an oil bath at 120 °C for 1 h and then at 170 °C for 2 h to yield a brown oil. This was cooled to room temperature and DCM (100 mL) was added and was then cooled in ice. 2,6-diisopropylaniline (11.2 mL, 60 mmol, 2 eq.) and NEt_3 (8.2 mL, 63 mmol, 2.1 eq.) were stirred together for 1 h and then added to the 2,6-

pyridinedicarboxylic acid chloride solution dropwise on ice and stirred overnight to yield a brown-red solution. The solvent was removed *in vacuo* and the formed solid washed with boiling hexane (3 * 75 mL), Et_2O (3 *75 mL) and was then dissolved in DCM (100 mL) and washed with 1 M HCl (3 * 100 mL). The combined organic layer was dried over magnesium sulphate for 30 min and the solvent removed in vacuo, after filtration, and dried under vacuum to yield a white solid. Its identity was confirmed by ^1H NMR (6.88 g, 47 %).

δ_{1H} = ^1H NMR (400 MHz, $CDCl_3$): 1.23 (t, *J* = 4.9 Hz, 24H), 1H), 3.19 (m, 4H), 7.24 (t, *J* = 4.9 Hz, 7.38 – 7.32 (m, 6H), 8.18 (t, *J* = 7.7 Hz 1H), 8.56 (d, *J* = 7.7 Hz, 2H), 8.99 (s, 2H)

δ_{1H} = ^1H NMR (400 MHz, [D_6]DMSO): 1.13 (dd, *J* = 22.6, 6.6 Hz, 24H), 3.08 (m, *J* = 6.9 Hz, 4H), 7.23 (d, *J* = 7.7 Hz, 4H), 7.32 (t, J = 7.3 Hz, 2H), 8.27 (t, *J* = 6.7 Hz, 1H), 8.31 (d, J = 7.2 2H), 10.64 (s, 2H).

3.2.2 [$Ni^{II}(PyN_2^{iPr2})(NCMe)$], (2)

Method A

2 was prepared according to the literature.[88] $NiCl_2$ (267 mg, 2.06 mmol) was refluxed in MeOH (30 mL) for 2 h until fully dissolved. **1** (1g, 2.06 mmol, 1 eq.) was added followed by a prepared solution of NaOMe (4.35 mmol, 2.1 eq., 10 mL MeOH) and the mixture was refluxed for 2 h to give a red solution. The solvent was removed *in vacuo* and the resulting solid dissolved in NCMe (50 mL) and refluxed overnight. The solvent was removed *in vacuo* and recrystallized from DCM and toluene to yield a red crystalline product after placing the solution in a freezer at -25 °C overnight. The product was isolated by filtration and dried under vacuum. Its identity was confirmed by ^1H NMR (637 mg, 53 %).

Method B

2 could also be prepared according to a different literature procedure.[87]. **1** (700 mg, 1.44 mmol) was dissolved in THF followed by the addition of KH (120 mg, 3.024 mmol, 2.1 eq.). The solution was stirred until bubbling had ceased. $Ni^{II}(OTf)_2$ (516 mg, 1.44 mmol, 1 eq.) was added followed by NCMe (2 mL). The mixture was stirred overnight to yield a red solution. The solvent was removed *in vacuo* and the resulting solid dissolved in DCM (50 mL), dried with Magnesium sulfate, filtered and the solvent was removed *in* *vacuo*. The product was recrystallised from DCM and toluene to yield a red crystalline product after placing the solution in a freezer at -25 °C overnight. The product was isolated by filtration and dried under vacuum. Its identity was confirmed by ^{1}H NMR (299 mg, 36 %).

δ_{1H} = (400 MHz, [D$_6$]DMSO): 1.07 (t, J = 8 Hz, 3H), 1.11(d, J = 6.8 Hz, 12H), 1.43 (d, *J* = 6.9 Hz, 12H),. 3.91 (m, 4H), 7.03 (d, J = 7.2 Hz, 4H), 7.10 (t, J = 6.7 Hz, 2H), 7.59 (d, *J* = 7.7 Hz, 2H), 8.16 (s, 1H).

3.2.3 $K_2[Fe^{II}_2(PyN_2^{iPr2})_2(bis\text{-}\mu\text{-}OH)_2]$ (3)

1 (200 mg, 0.42 mmol) was dissolved in DMF (8 mL). KH (35.4 mg, 0.86 mmol, 2.1 eq.) was added causing the solution to bubble and turn a light-yellow colour. Once bubbling had ceased, $Fe^{II}(OAc)_2$ (73 mg, 0.42 mmol, 1 eq.) was added to form a dark blue solution, and a white precipitate, which turned dark purple after 2 - 3 minutes. The solution was stirred for 1 h, filtered and excess toluene (15 mL) was added to the purple solution causing it to turn red. This was left in a freezer overnight to give a red solution with a dark red crystalline solid which was suitable for X-ray diffraction. Some of the red crystalline solid was placed in paraffin oil for XRD analysis, while the remainder was filtered and dried under vacuum (86 mg, 36.7%).

δ_{1H} = (400 MHz, [D$_6$]DMSO): -30.52, -25.06, -18.44, -16.22, -13.52, -7.55, -1.13, 1.06, 1.48, 7.92, 11.97, 13.50, 15.62, 31.09, 54.03, 71.34, 72.36, 82.12, 83.60, 95.96

ν_{max} (ATR-FTIR)/cm^{-1}: 3596 (O-H), 2959 (C-H), 2866 (C-H), 1671, 1602, 1440, 1379, 1360, 1253, 1099, 1057, 987, 933, 836, 804, 749, 683, 597

ESI-MS (direct injection, m/z): Found: 629.2790 ($Fe^{II}(PyN_2^{iPr2})(OH)] + DMF]^-$. $C_{34}H_{45}FeN_4O_4^-$ requires 629.2791)

3.2.4 $[Fe^{II}(PyN_2^{iPr2})(DMF)]$ (4a)

1 (200 mg, 0.42 mmol) was dissolved in DMF (8 mL). KH (35.4 mg, 0.86 mM, 2.1 eq.) was added causing the solution to bubble and turn a light-yellow colour. Once bubbling had ceased, $FeCl_2$ (26.7 mg, 0.21 mM, 1 eq.) was added to form a dark purple solution, which turned wine-red after 2-3 minutes. The solution was stirred for 1 h, filtered and layered with ether (15 mL). A dark purple solid was obtained after 2 - 3 days. The solid was filtered and dried under vacuum (140 mg, 22.1%).

δ_{1H} = (400 MHz, [D$_6$]DMSO): -25.25, -16.84, -6.57, 16.78, 20.29, 22.36, 46.22, 75.44, 91.62

ν_{max} (ATR-FTIR)/cm^{-1}: 3060 (CH), 2960 (CH), 2927 (CH), 2866 (CH), 1686, 1608, 1578, 1541, 1505, 1457, 1439, 1380, 1362, 1342, 1292, 1253, 1211, 1180, 1138, 1103, 949, 934, 864, 836, 795, 757, 742, 725, 682.

ESI-MS (direct injection, m/z) Found: 656.2167 ([Fe^{II}(PyN$_2$^{iPr2})(DMSO)] + K)$^+$. $C_{33}H_{43}FeKN_3O_3S^-$ requires 656.2012

λ_{max} = (DMSO)/nm: 520 (ε = 650 M^{-1}cm^{-1})

3.2.5 [Ni^{II}(PyN$_2$^{iPr2})(DMF)] (5)

1 (100 mg, 0.17 mmol) was dissolved in DMF (3 mL), stirred overnight and was layered with ether to yield a red crystalline solid suitable for X-ray diffraction. The solid was filtered and dried under vacuum (60 mg, 57.4%).

δ_{1H} = (600 MHz, $CDCl_3$): 1.27 (d, J = 6.9 Hz, 12H), 1.38 (d, J = 6.9 Hz, 12H), 1.65 (s, 3H), 2.32 (s, 3H), 3.93 (m, J = 6.9 Hz, 4H), 5.28 (s, 1H), 7.02 (d, J = 7.6 Hz, 4H), 7.09 (t, J = 7.7 Hz, 2H), 7.75 (d, J = 7.7 Hz, 2H), 8.03 (t, J = 7.7 Hz, 1H)

δ_{13C} = (150 MHz, $CDCl_3$): 23.4 (iPrCH$_3$), 24.3 (iPrCH$_3$), 28.9 (iPrCH), 31.5 (CH$_3$), 38.4 (CH$_3$), 122.9 (*m*-CH), 123.2 (*m*-pyCH), 125.6 (*p*-CH), 140.2 (*p*-pyCH), 140.5 (py-qC), 145.0 (*o*-qC), 151.7 (py-qC), 164.1 (COH), 166.7 (C=O)

ν_{max} (ATR-FTIR)/cm^{-1}: 3067 (C-H), 3026 (C-H), 2927, 2864 (C-H), 1660, 1626 (C=O), 1461, 1439, 1368, 1324, 1297, 1256, 1149, 1110, 1056, 1039, 986, 933, 890, 849, 800, 773, 746, 736, 720, 677, 592

λ_{max} = (DMF)/nm: 325 (sh, ε = 10,000 M^{-1}cm^{-1}), 355 (ε = 10800 M^{-1}cm^{-1}), 470 (ε = 1400 M^{-1}cm^{-1})

3.2.6 K[Ni^{II}(PyN$_2$^{iPr2})(OH)] (7a)

1 (100 mg, 0.17 mmol) was dissolved in a mixture of THF and DMF (4:1) (5 mL), yielding a dark red solution. KO_2 (20.1 mg, 0.28 mM, 2 eq.) and 18-C-6 (74 mg, 0.28 mmol, 2 eq.) were dissolved in DMF (2 mL) as best as possible. The two solutions were combined and were stirred for 1 – 2 h. The solution was filtered and layered with ether to yield a red crystalline product suitable for single crystal XRD after one week which was filtered and dried under vacuum (50 mg, 49.4%).

δ_{1H} = (400 MHz, [D$_6$]DMSO): -5.38 (s, 1H), 1.06 (d, *J* = 6.9 Hz, 12H), 1.28 (d, *J* = 6.9 Hz, 12H), 3.76 (m, *J* = 7.2 Hz, 4H), 6.87 (d, J = 7.2 Hz, 4H), 6.93 (t, J = 6.5 Hz, 2H), 7.47 (d, *J* = 7.7 Hz, 2H), 7.99 (t, *J* = 7.7 Hz, 1H)

ν_{max} (ATR-FTIR)/cm^{-1}: 3595 (O-H), 3058 (C-H), 2961 (C-H), 2866, 1674 (C=O), 1602, 1578, 1464, 1440, 1377, 1359, 1327, 1300, 1251, 1224, 1178, 1158, 1140, 1096, 1058, 1042, 987, 924, 891, 876, 836, 804, 776, 748, 733, 680, 661, 623, 595

ESI-TOF (m/z): Found: 588.2321 [Ni^{II}(PyN$_2$^{iPr2})(OH)]$^-$. $C_{31}H_{38}N_3NiO_3$ requires 558.2267

3.2.7 H$_2$PyN$_2$$^{iPr, iPrOH}$ (10a)

1 (500 mg, 0.7 mmol) was dissolved in DMF (10 mL). KO$_2$ (20 mg, 0.28 mM, 2 eq.) and 18-C-6 (147 mg, 0.56 mM, 4 eq.) were dissolved in DMF (40 mL). The two solutions were combined and allowed to stir overnight. 1 M HCl (50 mL) was added until the red colour had faded to a clear solution with a white precipitate which was filtered and dried under vacuum (300 mg, 87 % based of 1:1 mixture of **1**: **10a**). **10a** was separated from **1** by preparative TLC using 20% EtOAc in hexane as the mobile phase (~1mg, < 1%).

δ_{1H} = (600 MHz, [D$_6$]DMSO): 1.14 (d, J = 5.2 Hz, XH), 1.17 (d, J = 6.9 Hz, XH), 3.04 (m, J = 6.8 Hz, 1H), 3.09 (m, J = 6.5 Hz, 2H), 5.25 (s, 1H), 7.25 (d, J = 7.7 Hz, 2H), 7.29 – 7.36 (m, 3H), 7.58 (dd, J = 6.9, 2.4 Hz, 1H), 8.30 (t, J = 7.7 Hz, 1H), 8.38 (t, J = 7.7 Hz, 2H), 10.52 (s, 1H), 10.86 (s, 1H).

δ_{13C} = (150 MHz, [D$_6$]DMSO): 23.8, 24.2, 28.8, 31.0, 71.9, 123.6, 124.3, 125.1, 125.3, 125.5, 127.6, 128.5, 132.2, 140.8, 146.6, 146.6, 146.8, 147.2, 148.8, 149.1, 162.9, 163.2

ESI-TOF (m/z): Found: 500.2972 [H$_2$PyN$_2$^{iPr2OH} - H]$^-$. $C_{31}H_{38}N_3O_3^-$ requires 500.2913

3.2.8 Na[Ni^{II}(PyN$_2$^{iPr2})(N$_3$)] (11)

11 (60 mg, 0.1 mmol) and NaN$_3$ (9.9 mg, 0.15 mmol, 1.5 eq.) were dissolved in MeOH (2 mL) and stirred overnight. The solution was then layered with Et$_2$O to yield an orange powder. This orange powder was recrystallized from DMF and Et$_2$O to yield a red crystalline product after placing in at -20 °C for 3 days which was suitable for X-ray diffraction. The solid was filtered and dried under a stream of nitrogen for 8 hours (32 mg, 52.7%).

δ_{1H} = (600 MHz, [D$_6$]DMSO): 1.04 (d, J = 6.9 Hz, 12H), 1.33 (d, J = 6.9 Hz, 12H), 3.72 (d, J = 6.8 Hz, 4H), 6.85 (d, J = 6.8 Hz, 4H), 6.90 (t, J = 6.3 Hz, 2H), 7.54 (d, 7.7Hz, 2H), 8.08 (t, J = 7.8 Hz, 1H).

δ_{13C} = (150 MHz, [D$_6$]DMSO): 23.5, 24.5, 28.8, 122.2, 122.5, 124.6, 141.0, 142.6, 144.2, 151.1, 166.6

ν_{max} (ATR-FTIR)/cm^{-1}: 2958 (CH), 2868 (CH), 2090 (CN azide), 1615, 1600, 1575, 1468, 1450, 1389, 1360, 1328, 1301, 1256, 1098, 1057, 949, 937, 890, 829, 801, 774, 748, 735, 683, 639, 597, 584, 564, 555.

ESI-TOF (m/z): Found: 583.2305 [Ni^{II}(PyN$_2$^{iPr2})(N$_3$)]$^-$. $C_{31}H_{37}N_6NiO_2$ requires 583.2331

λ_{max} = (NCMe)/nm: 300 (ε = 7500 M^{-1}cm^{-1}), 390 (ε = 4300 M^{-1}cm^{-1})

3.3 General procedure for UV-scale addition of KO_2 to 2

A 20 mL solution of **2** was prepared at the desired concentration. The UV-vis studies were carried out using 2 mL of solution in a quartz cuvette. A solution of KO_2 (10 or 20 mM, 2 eq.) and 18-C-6 (20 or 40 mM, 4 eq.) were added to the **2** solution and the changes in the UV-vis spectrum were monitored. 10m mM KO_2 solutions were prepared fresh each day while 20 mM KO_2 solutions were prepared fresh every 3 – 4 hours.

3.4 General procedure for the control reactions of 2 with H_2O_2 (Scheme 8)

2 (100 mg, 01.7 mmol) was dissolved in THF (3 mL scheme 8 A/B) or 3:1 THF:acetone (Scheme 8 C). To this solution was added: (A) H_2O_2 (30 μL, 0.34 mmol, 2 eq.), (B) H_2O_2 (30 μL, 0.34 mmol, 2 eq.) and NEt_3 (50 μL, 0.36 mmol, 2.1 eq.), (C) H_2O_2 (30 μL, 0.34 mmol, 2 eq.), NEt_3 (50 μL, 0.36 mmol, 2.1 eq) and KPF_6 (62.6 mg, 0.34 mmol, 2 eq.). The solutions were stirred overnight, the solvent removed *in vacuo*, to give a red solid.

3.5 Cold injection ESI-MS sample preparation and analysis

Upon formation of a sample by, as observed by UV-vis spectrophotometry, a pipette was used to transfer some of the solution into a small vial which was frozen using liquid nitrogen. Upon thawing, the samples were immediately injected directly into the spectrometer (no HPLC loop) ensuring the minimum amount of thermal decay prior to injection.

4. References

[1] A. A. Yaroshevsky, *Geochemistry Int.* **2006**, *44*, 48–55.

[2] M. Costas, M. P. Mehn, M. P. Jensen, L. Que, *Chem. Rev.* **2004**, *104*, 939–986.

[3] Y. Sheng, I. A. Abreu, D. E. Cabelli, M. J. Maroney, A. F. Miller, M. Teixeira, J. S. Valentine, *Chem. Rev.* **2014**, *114*, 3854–3918.

[4] D. T. Sawyer, J. S. Valentine, *Acc. Chem. Res.* **1981**, *14*, 393–400.

[5] E. E. Nelson, A. E. Guyer, *Inorg. Chem.* **2010**, *49*, 3618–3628.

[6] J. M. Bollinger, C. Krebs, *Curr. Opin. Chem. Biol.* **2007**, *11*, 151–158.

[7] T. Wilcox, A. Hirshkowitz, *Curr. Opin. Chem. Biol.* **2010**, *20*, 673–683.

[8] L. Que, W. B. Tolman, *Nature* **2008**, *455*, 333–340.

[9] A. Mukherjee, M. A. Cranswick, M. Chakrabarti, T. K. Paine, K. Fujisawa, E. Münck, L. Que, *Inorg. Chem.* **2010**, *49*, 3618–3628.

[10] J. E. Baldwin, M. Bradley, *Chem. Rev.* **1990**, *90*, 1079–1088.

[11] J. P. Klinman, *J. Biol. Chem.* **2006**, *281*, 3013–3016.

[12] J. S. Boswell, B. J. Reedy, R. Kulathila, D. Merkler, N. J. Blackburn, *Biochemistry* **1996**, *35*, 12241–12250.

[13] P. L. Roach, J. Cllftont, V. Fiilipt, K. Harlost, G. J. Bartont, J. Hajdut, I. Anderssontt, C. J. Schofield, J. E. Baldwin, *Nature* **1995**, *375*, 700–704.

[14] P. L. Roach, I. J. Clifton, C. M. H. Hensgens, N. Shibata, A. J. Long, R. W. Strange, S. S. Hasnain, C. J. Schofield, J. E. Baldwin, J. Hajdu, *Eur. J. Biochem.* **1996**, *242*, 736–740.

[15] C. R. Randall, Y. Zang, A. E. True, L. Que, J. M. Charnock, C. D. Garner, Y. Fujishima, C. J. Schofield, J. E. Baldwin, *Biochemistry* **1993**, *32*, 6664–6673.

[16] P. L. Roach, C. M. H. Hensgens, N. Shibata, C. J. Schofield, J. Hajdu, J. E. Baldwin, *Nature* **1997**, *387*, 827–830.

[17] M. Lundberg, P. E. M. Siegbahn, K. Morokuma, *Biochemistry* **2008**, *47*, 1031–1042.

[18] W. C. W. Chen, J. E. Baily, M. Corselli, M. Diaz, B. Sun, G. Xiang, G. A. Gray, J. Huard, B. Péault, *J. Am. Chem. Soc.* **2016**, *138*, 8862–8874.

[19] J. P. Klinman, *Chem. Rev.* **1996**, *96*, 2541–2562.

[20] S. T. Prigge, R. E. Mains, B. A. Eipper, L. M. Amzel, *Cell. Mol. Life Sci.* **2000**, *57*, 1236–1259.

[21] W. A. Francisco, D. J. Merkler, N. J. Blackburn, J. P. Klinman, *Biochemistry* **1998**, *37*, 8244–8252.

[22] P. Chen, E. I. Solomon, *J. Am. Chem. Soc.* **2004**, *126*, 4991–5000.

[23] S. Kim, J. W. Ginsbach, J. Y. Lee, R. L. Peterson, J. J. Liu, M. A. Siegler, A. A.

Sarjeant, E. I. Solomon, K. D. Karlin, *J. Am. Chem. Soc.* **2015**, *137*, 2867–2874.

[24] C. J. Cramer, *Proc. Natl. Acad. Sci.* **2003**, *100*, 3635–3640.

[25] W. Nam, *Acc. Chem. Res.* **2015**, *48*, 2415–2423.

[26] C. Krebs, D. Galonic Fujimori, J. M. Bollinger, C. W. Walsh, *Acc. Chem. Res.* **2007**, *40*, 484–492.

[27] J. C. Price, E. W. Barr, L. M. Hoffart, C. Krebs, J. M. Bollinger, *Biochemistry* **2005**, *44*, 8138–8147.

[28] K. P. McCusker, J. P. Klinman, *Proc. Natl. Acad. Sci.* **2009**, *106*, 19791–19795.

[29] M. D. Lloyd, H. J. Lee, K. Harlos, Z. H. Zhang, J. E. Baldwin, C. J. Schofield, J. M. Charnock, C. D. Garner, T. Hara, A. C. Terwisscha Van Scheltinga, et al., *J. Mol. Biol.* **1999**, *287*, 943–960.

[30] N. J. Cosper, C. M. V. Stålhandske, R. E. Saari, R. P. Hausinger, R. A. Scott, *J. Biol. Inorg. Chem.* **1999**, *4*, 122–129.

[31] E. G. Pavel, N. Kitajima, E. I. Solomon, *J. Am. Chem. Soc.* **1998**, *120*, 3949–3962.

[32] Z. Zhang, J. shan Ren, K. Harlos, C. H. McKinnon, I. J. Clifton, C. J. Schofield, *FEBS Lett.* **2002**, *517*, 7–12.

[33] J. C. Price, E. W. Barr, B. Tirupati, J. M. Bollinger, C. Krebs, *Biochemistry* **2003**, *42*, 7497–7508.

[34] L. F. Wu, S. Meng, G. L. Tang, *Biochim. Biophys. Acta - Proteins Proteomics* **2016**, *1864*, 453–470.

[35] C. Würtele, E. Gaoutchenova, K. Harms, M. C. Holthausen, J. Sundermeyer, S. Schindler, *Angew. Chemie - Int. Ed.* **2006**, *45*, 3867–3869.

[36] N. W. Aboelella, S. V. Kryatov, B. F. Gherman, W. W. Brennessel, V. G. Young, R. Sarangi, E. V. Rybak-Akimova, K. O. Hodgson, B. Hedman, E. I. Solomon, et al., *J. Am. Chem. Soc.* **2004**, *126*, 16896–16911.

[37] J. Cho, R. Sarangi, H. Y. Kang, J. Y. Lee, M. Kubo, T. Ogura, E. I. Solomon, W. Nam, *J. Am. Chem. Soc.* **2010**, *132*, 16977–16986.

[38] S. Yao, E. Bill, C. Milsmann, K. Wieghardt, M. Driess, *Angew. Chemie - Int. Ed.* **2008**, *47*, 7110–7113.

[39] S. Hong, K. D. Sutherlin, J. Park, E. Kwon, M. A. Siegler, E. I. Solomon, W. Nam, *Nat. Commun.* **2014**, *5*, 1–7.

[40] P. Pirovano, A. M. Magherusan, C. McGlynn, A. Ure, A. Lynes, A. R. McDonald, *Angew. Chemie - Int. Ed.* **2014**, *53*, 5946–5950.

[41] C. Panda, A. Chandra, T. Corona, E. Andris, B. Pandey, S. Garai, N. Lindenmaier, S. Künstner, E. R. Farquhar, J. Roithová, et al., *Angew. Chemie - Int. Ed.* **2018**, *57*, 14883–14887.

[42] M. Nappa, J. S. Valentine, A. R. Miksztal, H. J. Schugar, S. S. Isied, *J. Am. Chem. Soc.* **1979**, *101*, 7744–7746.

[43] K. Fujisawa, M. Tanaka, Y. Moro-oka, N. Kitajima, *J. Am. Chem. Soc.* **1994**, *116*, 12079–12080.

[44] J. W. Egan, B. S. Haggerty, A. L. Rheingold, S. C. Sendlinger, K. H. Theopold, *J. Am. Chem. Soc.* **1990**, *112*, 2445–2446.

[45] A. M. Reynolds, B. F. Gherman, C. J. Cramer, W. B. Tolman, *Inorg. Chem.* **2005**, *44*, 6989–6997.

[46] D. J. E. Spencer, N. W. Aboelella, A. M. Reynolds, P. L. Holland, W. B. Tolman, *J. Am. Chem. Soc.* **2002**, *124*, 2108–2109.

[47] P. Chen, D. E. Root, C. Campochiaro, K. Fujisawa, E. I. Solomon, *J. Am. Chem. Soc.* **2003**, *125*, 466–474.

[48] M. Schatz, V. Raab, S. P. Foxon, G. Brehm, S. Schneider, M. Reiher, M. C. Holthausen, J. Sundermeyer, S. Schindler, *Angew. Chemie - Int. Ed.* **2004**, *43*, 4360–4363.

[49] K. D. Karlin, N. Wei, B. Jung, S. Kaderli, P. Niklaus, A. D. Zuberbühler, *J. Am. Chem. Soc.* **1993**, *115*, 9506–9514.

[50] R. L. Peterson, R. A. Himes, H. Kotani, T. Suenobu, L. Tian, M. A. Siegler, E. I. Solomon, S. Fukuzumi, K. D. Karlin, *J. Am. Chem. Soc.* **2011**, *133*, 1702–1705.

[51] D. Maiti, H. C. Fry, J. S. Woertink, M. A. Vance, E. I. Solomon, K. D. Karlin, *J. Am. Chem. Soc.* **2007**, *129*, 264–265.

[52] M. Bhadra, J. Y. C. Lee, R. E. Cowley, S. Kim, M. A. Siegler, E. I. Solomon, K. D. Karlin, *J. Am. Chem. Soc.* **2018**, *140*, 9042–9045.

[53] S. Kim, J. Y. Lee, R. E. Cowley, J. W. Ginsbach, M. A. Siegler, E. I. Solomon, K. D. Karlin, *J. Am. Chem. Soc.* **2015**, *137*, 2796–2799.

[54] J. Y. Lee, R. L. Peterson, K. Ohkubo, I. Garcia-Bosch, R. A. Himes, J. Woertink, C. D. Moore, E. I. Solomon, S. Fukuzumi, K. D. Karlin, *J. Am. Chem. Soc.* **2014**, *136*, 9925–9937.

[55] J. E. Pate, R. W. Cruse, K. D. Karlin, E. I. Solomon, *J. Am. Chem. Soc.* **1987**, *109*, 2624–2630.

[56] L. Q. Hatcher, D. H. Lee, M. A. Vance, A. E. Milligan, R. Sarangi, K. O. Hodgson, B. Hedman, E. I. Solomon, K. D. Karlin, *Inorg. Chem.* **2006**, *45*, 10055–10057.

[57] S. Kim, J. W. Ginsbach, A. I. Billah, M. A. Siegler, C. D. Moore, E. I. Solomon, K. D. Karlin, *J. Am. Chem. Soc.* **2014**, *136*, 8063–8071.

[58] Y. Lee, D. H. Lee, G. Y. Park, H. R. Lucas, A. A. Narducci Sarjeant, M. T. Kieber-Emmons, M. A. Vance, A. E. Milligan, E. I. Solomon, K. D. Karlin, *Inorg. Chem.* **2010**, *49*, 8873–8885.

[59] G. Y. Park, Y. Lee, D. H. Lee, J. S. Woertink, A. A. Narducci Sarjeant, E. I. Solomon, K. D. Karlin, *Chem. Commun.* **2010**, *46*, 91–93.

[60] S. O. Kim, C. V. Sastri, M. S. Seo, J. Kim, W. Nam, *J. Am. Chem. Soc.* **2005**, *127*, 4178–4179.

[61] Y. Lee, S. Hong, Y. Morimoto, W. Shin, S. Fukuzumi, W. Nam, *J. Am. Chem. Soc.* **2010**, *132*, 10668–10670.

[62] X. Shan, L. Que Jr., *Proc. Natl. Acad. Sci.* **2005**, *12*, 5340–5345.

[63] C. W. Chiang, S. T. Kleespies, H. D. Stout, K. K. Meier, P. Y. Li, E. L. Bominaar, L. Que, E. Münck, W. Z. Lee, *J. Am. Chem. Soc.* **2014**, *136*, 10846–10849.

[64] A. Chanda, X. Shan, M. Chakrabarti, W. C. Ellis, D. L. Popescu, F. T. De Oliveira, D. Wang, L. Que, T. J. Collins, E. Münck, et al., *Inorg. Chem.* **2008**, *47*, 3669–3678.

[65] A. R. Tao, A. Schwartz, D. H. Gracias, G. M. Whitesides, J. R. Abelson, M. K. Erhardt, R. G. Nuzzo, R. G. Nuzzo, J. A. Rogers, O. O. Park, et al., **2006**, *311*, 212–216.

[66] C. A. Rettenmeier, H. Wadepohl, L. H. Gade, *Angew. Chemie - Int. Ed.* **2015**, *54*, 4880–4884.

[67] K. Fujita, R. Schenker, W. Gu, T. C. Brunold, S. P. Cramer, C. G. Riordan, *Inorg. Chem.* **2004**, *43*, 3324–3326.

[68] M. T. Kieber-Emmons, J. Annaraj, M. S. Seo, K. M. Van Heuvelen, T. Tosha, T. Kitagawa, T. C. Brunold, W. Nam, C. G. Riordan, *J. Am. Chem. Soc.* **2006**, *128*, 14230–14231.

[69] K. Shiren, S. Ogo, S. Fujinami, H. Hayashi, M. Suzuki, A. Uehara, Y. Watanabe, Y. Moro-oka, *J. Am. Chem. Soc.* **2000**, *122*, 254–262.

[70] J. Cho, H. Y. Kang, L. V. Liu, R. Sarangi, E. I. Solomon, W. Nam, *Chem. Sci.* **2013**, *4*, 1502–1508.

[71] A. Company, S. Yao, K. Ray, M. Driess, *Chem. - A Eur. J.* **2010**, *16*, 9669–9675.

[72] P. J. Donoghue, A. K. Gupta, D. W. Boyce, C. J. Cramer, W. B. Tolman, *J. Am. Chem. Soc.* **2010**, 1–20.

[73] J. Annaraj, J. Cho, Y. M. Lee, S. Y. Kim, R. Latifi, S. P. De Visser, W. Nam, *Angew. Chemie - Int. Ed.* **2009**, *48*, 4150–4153.

[74] J. Cho, R. Sarangi, J. Annaraj, S. Y. Kim, T. Ogura, E. I. Solomon, W. Nam, *Nat. Chem.* **2009**, *1*, 568–572.

[75] Y. Jo, J. Annaraj, M. S. Seo, Y. M. Lee, S. Y. Kim, J. Cho, W. Nam, *J. Inorg. Biochem.* **2008**, *102*, 2155–2159.

[76] G. Strukul, *Angew. Chemie - Int. Ed.* **1998**, *37*, 1198–1209.

[77] S. Calvin, *XAFS for Everyone*, CRC Press, **2013**.

[78] G. Bunker, *Introduction to XAFS: A Practical Guide to x-Ray Absorption Fine Structure Spectroscopy*, Cambridge University Press, **2010**.

[79] L. A Que, *Physical Methods in Bioinorganic Chemistry: Spectroscopy and Magnetism*, University Science Books, **2000**.

[80] J. A. van Bokhoven, C. Lamberti, *X-Ray Absorption and X-Ray Emission*

Spectroscopy: Theory and Applications, **2015**.

[81] B. Ravel, D. Hesterberg, L. Richard Drees, S. D. Kelly, A. L. Ulery, *Methods of Soil Analysis Part 5 - Mineralogical Methods*, Soil Society Of America, **2008**.

[82] K. O. Cramer, S. P., Hodgson, *X-Ray Absorption Spectroscopy: A New Structural Method and Its Applications to Bioinorganic Chemistry*, John Wiley & Sons Inc., **1979**.

[83] L. shan Kau, D. J. Spira-Solomon, J. E. Penner-Hahn, K. O. Hodgson, E. I. Solomon, *J. Am. Chem. Soc.* **1987**, *109*, 6433–6442.

[84] J. L. DuBois, P. Mukherjee, T. D. P. Stack, B. Hedman, E. I. Solomon, K. O. Hodgson, *J. Am. Chem. Soc.* **2000**, *122*, 5775–5787.

[85] R. E. Schreiber, H. Cohen, G. Leitus, S. G. Wolf, A. Zhou, L. Que, R. Neumann, *J. Am. Chem. Soc.* **2015**, *137*, 8738–8748.

[86] J. C. Wasilke, G. Wu, X. Bu, G. Kehr, G. Erker, *Organometallics* **2005**, *24*, 4289–4297.

[87] P. Pirovano, E. R. Farquhar, M. Swart, A. R. McDonald, *J. Am. Chem. Soc.* **2016**, *138*, 14362–14370.

[88] P. Pirovano, A. R. Berry, M. Swart, A. R. McDonald, *Dalt. Trans.* **2018**, *47*, 246–250.

[89] P. J. Donoghue, J. Tehranchi, C. J. Cramer, R. Sarangi, E. I. Solomon, W. B. Tolman, *J. Am. Chem. Soc.* **2011**, *133*, 17602–17605.

[90] D. Huang, O. V. Makhlynets, L. L. Tan, S. C. Lee, E. V. Rybak-Akimova, R. H. Holm, *Inorg. Chem.* **2011**, *50*, 10070–10081.

[91] D. Dhar, W. B. Tolman, *J. Am. Chem. Soc.* **2015**, *137*, 1322–1329.

[92] A. D. Spaeth, N. L. Gagnon, D. Dhar, G. M. Yee, W. B. Tolman, *J. Am. Chem. Soc.* **2017**, *139*, 4477–4485.

[93] B. D. Neisen, N. L. Gagnon, D. Dhar, A. D. Spaeth, W. B. Tolman, *J. Am. Chem. Soc.* **2017**, *139*, 10220–10223.

[94] D. Dhar, G. M. Yee, A. D. Spaeth, D. W. Boyce, H. Zhang, B. Dereli, C. J. Cramer, W. B. Tolman, *J. Am. Chem. Soc.* **2016**, *138*, 356–368.

[95] J. C. Wasilke, G. Wu, X. Bu, G. Kehr, G. Erker, *Organometallics* **2005**, *24*, 4289–4297.

[96] F. Czerny, P. Döhlert, M. Weidauer, E. Irran, S. Enthaler, *Inorganica Chim. Acta* **2015**, *425*, 118–123.

[97] D. Dhar, G. M. Yee, T. F. Markle, J. M. Mayer, W. B. Tolman, *Chem. Sci.* **2017**, *8*, 1075–1085.

[98] J. C. Noveron, M. M. Olmstead, P. K. Mascharak, *J. Am. Chem. Soc.* **2001**, *123*, 3247–3259.

[99] M. Ray, D. Ghosh, Z. Shirin, R. Mukherjee, *Inorg. Chem.* **2002**, *36*, 3568–3572.

[100] T. C. Harrop, L. A. Tyler, M. M. Olmstead, P. K. Mascharak, *Eur. J. Inorg. Chem.* **2003**, 475–481.

[101] K. Ghosh, S. Kumar, R. Kumar, U. P. Singh, *J. Organomet. Chem.* **2014**, *750*, 169–175.

[102] M. Ghiladi, F. B. Larsen, C. J. Mckenzie, I. Sotofte, J.-P. Tuchagues, *Dalt. Trans.* **2005**, 1687–1692.

[103] O. Y. Lyakin, A. M. Zima, D. G. Samsonenko, K. P. Bryliakov, E. P. Talsi, *ACS Catal.* **2015**, *5*, 2702–2707.

[104] V. L. MacMurdo, H. Zheng, L. Que, *Inorg. Chem.* **2000**, *39*, 2254–2255.

[105] P. C. A. Bruijnincx, I. L. C. Buurmans, Y. Huang, G. Juhász, M. Viciano-Chumillas, M. Quesada, J. Reedijk, M. Lutz, A. L. Spek, E. Münck, et al., *Inorg. Chem.* **2011**, *50*, 9243–9255.

[106] A. Stubna, D. H. Jo, M. Costas, W. W. Brenessel, H. Andres, E. L. Bominaar, E. Münck, L. Que, *Inorg. Chem.* **2004**, *43*, 3067–3079.

[107] O. V. Makhlynets, W. N. Oloo, Y. S. Moroz, I. G. Belaya, T. D. Palluccio, A. S. Filatov, P. Müller, M. A. Cranswick, L. Que, E. V. Rybak-Akimova, *Chem. Commun.* **2014**, *50*, 645–648.

[108] A. W. Addison, T. N. Rao, J. Reedijk, J. van Rijn, G. C. Verschoor, *Dalt. Trans.* **1984**, 1349–1356.

[109] L. Yang, D. R. Powell, R. P. Houser, *Dalt. Trans.* **2007**, 955–964.

[110] A. Okuniewski, D. Rosiak, J. Chojnacki, B. Becker, *Polyhedron* **2015**, *90*, 47–57.

[111] P. Pirovano, B. Twamley, A. R. McDonald, *Chem. - A Eur. J.* **2018**, *24*, 5238–5245.

[112] H. E. Gottlieb, V. Kotlyar, A. Nudelman, *J. Org. Chem.* **1997**, *62*, 7512–7515.

[113] A. Shastri, A. K. Das, S. Krishnakumar, P. J. Singh, B. N. Raja Sekhar, *J. Chem. Phys.* **2017**, *147*, 224305.

[114] P. A. Mosier-Boss, A. I. Popov, *J. Am. Chem. Soc.* **1985**, *107*, 6168–6174.

[115] Y. Wei, X. Dang, S. Hu, *Russ. J. Electrochem.* **2004**, *40*, 400–403.

[116] E. J. Nanni, D. T. Sawyer, *J. Am. Chem. Soc.* **1980**, *102*, 7591–7593.

[117] J. Wenz, A. Kochan, H. Wadepohl, L. H. Gade, *Inorg. Chem.* **2017**, *56*, 3631–3643.

[118] S. Wiese, M. J. B. Aguila, E. Kogut, T. H. Warren, *Organometallics* **2013**, *32*, 2300–2308.

[119] H. V. Huynh, C. H. M. Koh, V. H. Nguyen, *Dalt. Trans.* **2017**, *46*, 11318–11326.

[120] M. Abubekerov, T. L. Gianetti, A. Kunishita, J. Arnold, *Dalt. Trans.* **2013**, *42*, 10525–10532.

[121] S. Mandal, S. Mondal, C. Rajnák, J. Titiš, R. Boča, S. Mohanta, *Dalt. Trans.*

2017, *46*, 13135–13144.

[122] A. M. Magherusan, S. Kal, D. N. Nelis, L. M. Doyle, E. R. Farquhar, L. Que, A. R. McDonald, *Angew. Chemie - Int. Ed.* **2019**, *58*, 5718–5722.

[123] T. C. Weng, W. Y. Hsieh, E. S. Uffelman, S. W. Gordon-Wylie, T. J. Collins, V. L. Pecoraro, J. E. Penner-Hahn, *J. Am. Chem. Soc.* **2004**, *126*, 8070–8071.

[124] F. Farges, *Phys. Rev. B - Condens. Matter Mater. Phys.* **2005**, *71*, 1–14.

[125] A. Magherusan, A. Zhou, E. Farquhar, M. Garcia Melchor, B. Twamley, L. Que Jr., A. R. McDonald, *Angew. Chemie Int. Ed.* **2017**, 918–922.

[126] M. Roemelt, M. a Beckwith, C. Duboc, M.-N. Collomb, F. Neese, S. DeBeer, *Inorg. Chem.* **2012**, *51*, 680–7.

[127] G. Dräger, T. Kirchner, S. Bocharov, C. C. Kao, *J. Synchrotron Radiat.* **2001**, *8*, 398–400.

[128] J. A. Rees, V. Martin-Diaconescu, K. A. Kovacs, S. DeBeer, *Inorg. Chem.* **2015**, *54*, 6410–6422.

[129] T. L. Stemmler, T. M. Sossong, J. I. Goldstein, D. E. Ash, T. E. Elgren, D. M. Kurtz, J. E. Penner-Hahn, *Biochemistry* **1997**, *36*, 9847–9858.

[130] R. B. Vanatta, C. E. Strouse, L. K. Hanson, J. S. Valentine, *J. Am. Chem. Soc.* **1987**, *109*, 1425–1434.

[131] N. Kitajima, H. Komatsiizaki, S. Hikichi, M. Osawa, Y. Moro-oka, *J. Am. Chem. Soc.* **1994**, *116*, 11596–11597.

[132] U. P. Singh, A. K. Sharma, S. Hikichi, H. Komatsuzaki, Y. Moro-oka, M. Akita, *Inorganica Chim. Acta* **2006**, *359*, 4407–4411.

[133] M. S. Seo, J. Y. Kim, J. Annaraj, Y. Kim, Y. M. Lee, S. J. Kim, J. Kim, W. Nam, *Angew. Chemie - Int. Ed.* **2007**, *46*, 377–380.

[134] J. Annaraj, J. Cho, Y. M. Lee, S. Y. Kim, R. Latifi, S. P. De Visser, W. Nam, *Angew. Chemie - Int. Ed.* **2009**, *48*, 4150–4153.

[135] H. Kang, J. Cho, K. Bin Cho, T. Nomura, T. Ogura, W. Nam, *Chem. - A Eur. J.* **2013**, *19*, 14119–14125.

[136] C. Teutloff, K. O. Schäfer, S. Sinnecker, V. Barynin, R. Bittl, K. Wieghardt, F. Lendzian, W. Lubitz, *Magn. Reson. Chem.* **2005**, *43*, 51–64.

[137] L. Dubois, D. F. Xiang, X. S. Tan, J. Pécaut, P. Jones, S. Baudron, L. Le Pape, J. M. Latour, C. Baffert, S. Chardon-Noblat, et al., *Inorg. Chem.* **2003**, *42*, 750–760.

[138] H. Diril, X. Zhang, J. A. Potenza, H. J. Schugar, S. S. Isied, H. R. Chang, M. J. Nilges, D. N. Hendrickson, *J. Am. Chem. Soc.* **1989**, *111*, 5102–5114.

[139] S. Characterization, *J. Chem. Soc. Chem. Commun.* **1985**, 347–349.

[140] R. Singh, M. Haukka, C. J. McKenzie, E. Nordlander, *Eur. J. Inorg. Chem.* **2015**, *2015*, 3485–3492.

[141] J. L. DuBois, P. Mukherjee, A. M. Colier, J. M. Mayer, E. I. Solomon, B. Hedman, T. D. P. Stack, K. O. Hodgson, *J. Am. Chem. Soc.* **1997**, *119*, 8578–8579.

[142] L. shan Kau, D. J. Spira-solomon, J. E. Penner-Hahn, K. O. Hodgson, E. I. Solomon, *J. Am. Chem. Soc.* **1987**, *109*, 6433–6442.

[143] R. Sarangi, N. Aboelella, K. Fujisawa, W. B. Tolman, B. Hedman, K. O. Hodgson, E. I. Solomon, *J. Am. Chem. Soc.* **2006**, *128*, 8286–8296.

[144] H. C. Chang, F. C. Lo, W. C. Liu, T. H. Lin, W. F. Liaw, T. S. Kuo, W. Z. Lee, *Inorg. Chem.* **2015**, *54*, 5527–5533.

[145] J. L. DuBois, P. Mukherjee, T. D. P. Stack, B. Hedman, E. I. Solomon, K. O. Hodgson, *J. Am. Chem. Soc.* **2000**, *122*, 5775–5787.

[146] R. Sarangi, S. D. B. George, D. J. Rudd, R. K. Szilagyi, X. Ribas, C. Rovira, M. Almeida, K. O. Hodgson, B. Hedman, E. I. Solomon, *J. Am. Chem. Soc.* **2007**, *129*, 2316–2326.

[147] R. Sarangi, N. Aboelella, K. Fujisawa, W. B. Tolman, B. Hedman, K. O. Hodgson, E. I. Solomon, *J. Am. Chem. Soc.* **2006**, *128*, 8286–8296.

[148] L. shan Kau, D. J. Spira-solomon, J. E. Spira-solomon-penner-hahn, K. O. Hodgson, E. I. Solomon, *J. Am. Chem. Soc.* **1987**, *109*, 6433–6442.

[149] B. Cordero, A. E. Platero-prats, M. Rev, J. Echeverr, E. Cremades, F. Barrag, **2008**, 2832–2838.

[150] B. Ravel, M. Newville, *J. Synchrotron Radiat.* **2005**, *12*, 537–541.

5. Appendix

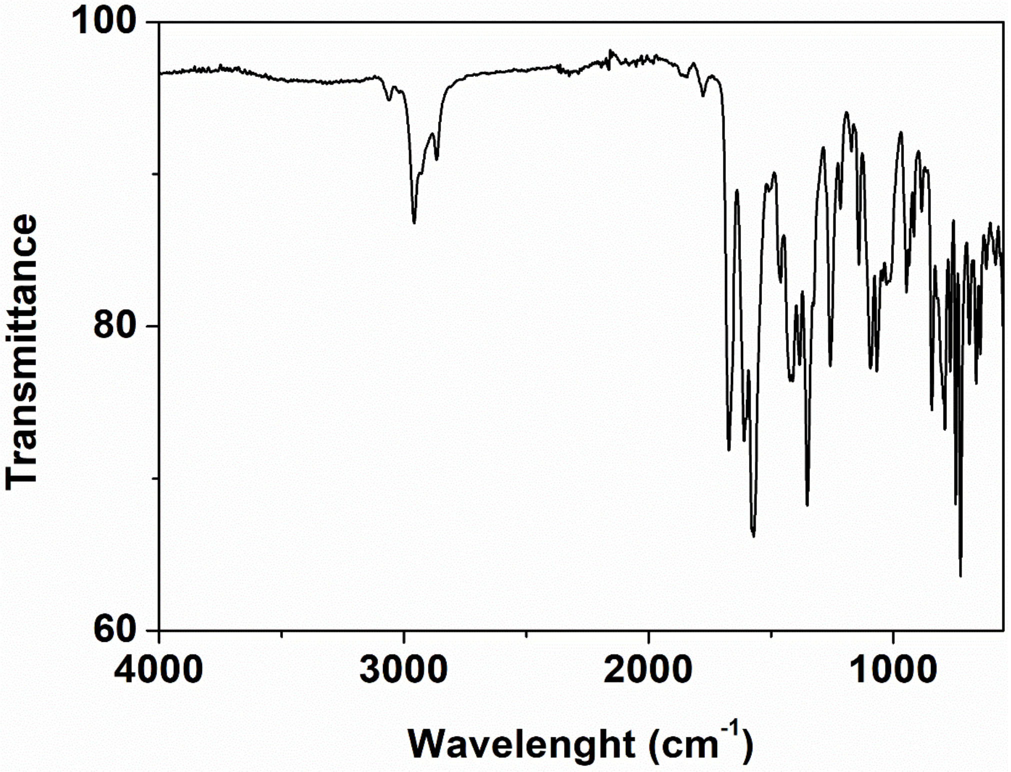

Figure S1. ATR-FTIR spectrum of **3**

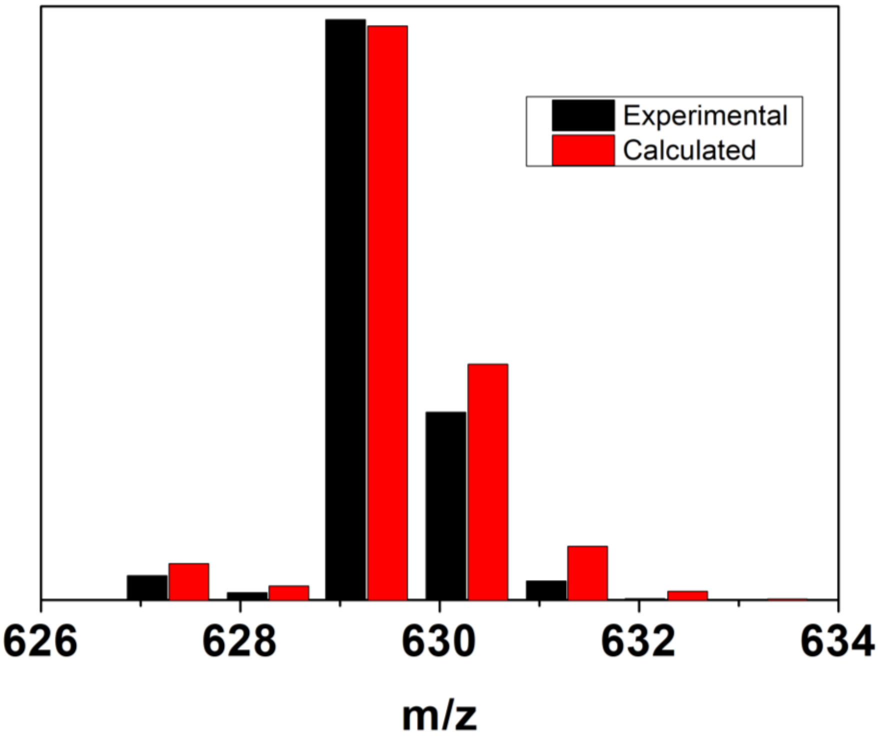

Figure S2. Negative mode ESI-MS of **3**. Observed: 629.2648, calculated: 629.2790 $[[Fe^{II}(PyN_2^{iPr2})(OH)] + DMF)]^-$

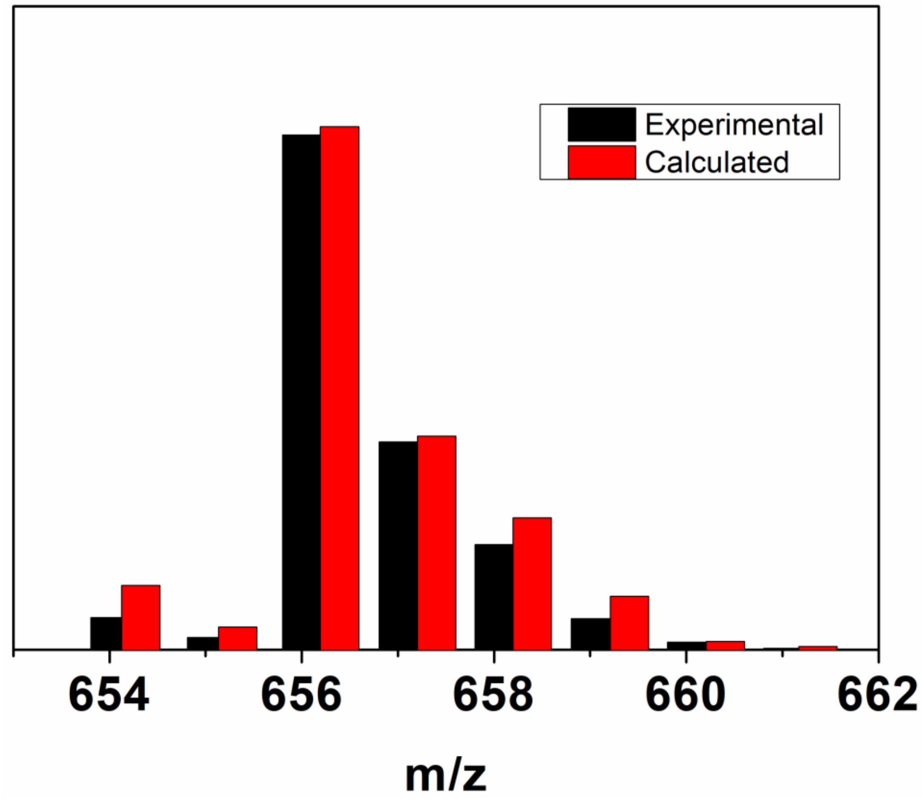

Figure S3. Positive mode ESI-MS of **4a**. Observed: 656.2011, calculated m/z = 656.2012 [[$Fe^{II}(PyN_2^{iPr2})(DMF)$] + K]$^+$

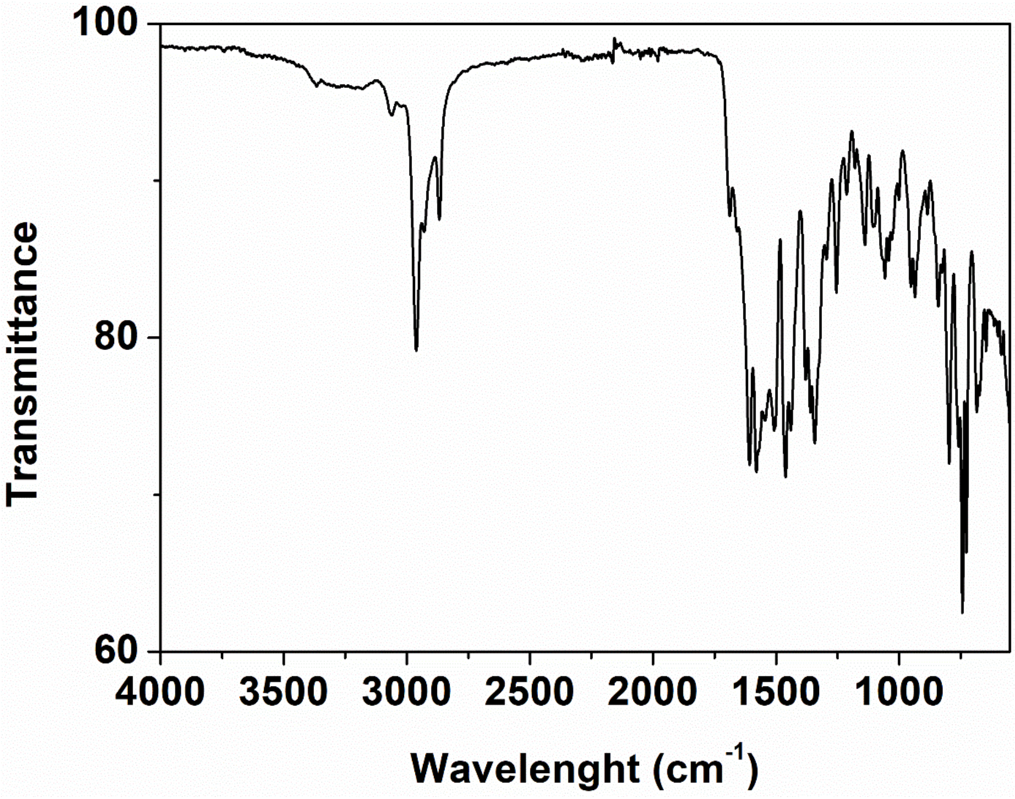

Figure S4. ATR-FTIR spectrum of **4a**

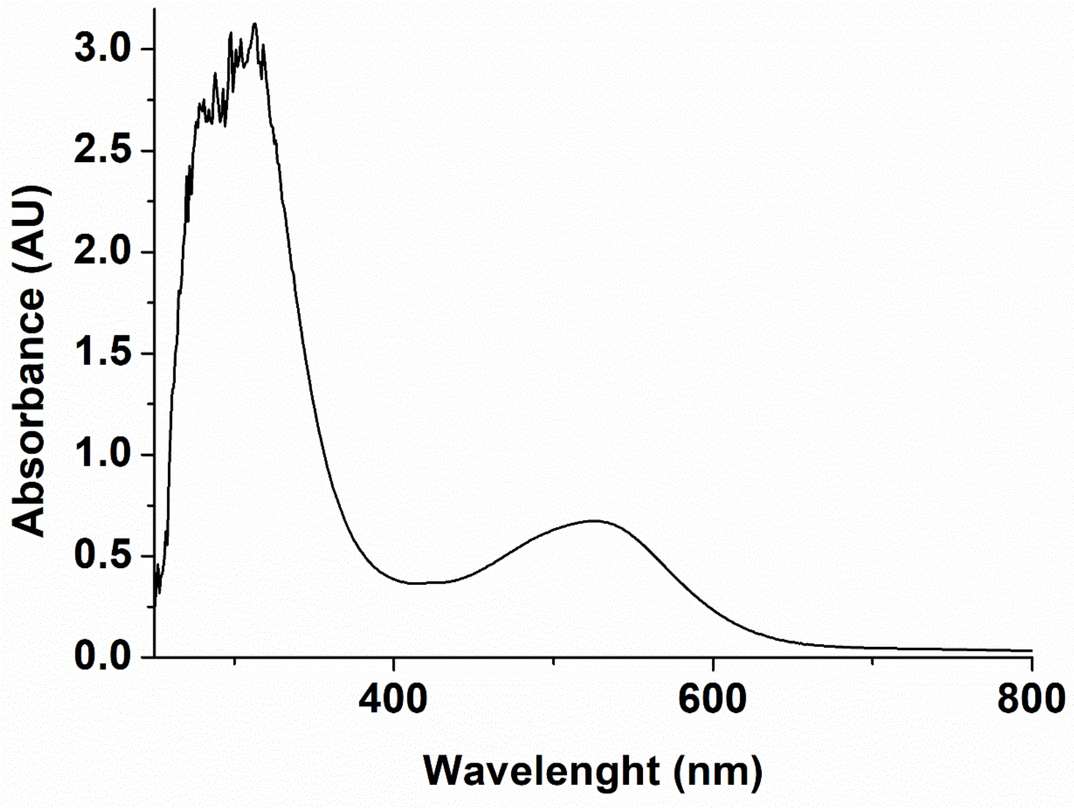

Figure S5. 1 mM UV-vis spectrum of **4a** (λ_{max} = 525 nm (ε = 650 $cm^{-1}L^{-1}$, DMSO)

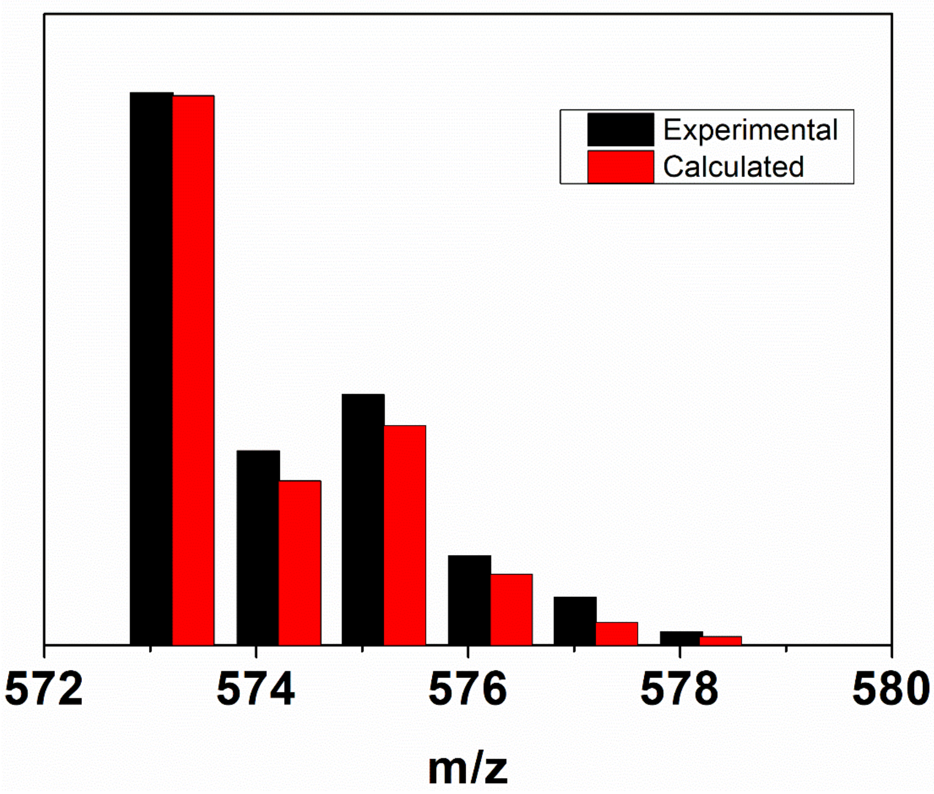

Figure S6. Cold-injection ESI-MS of the reaction mixture of **2** + 2 eq. KO_2 + 4 eq. 18-C-6 . Observed: 573.2158. Calculated: 573.2138 $[Ni^{II}(PyN_2^{iPr2})(O_2)]^-$.

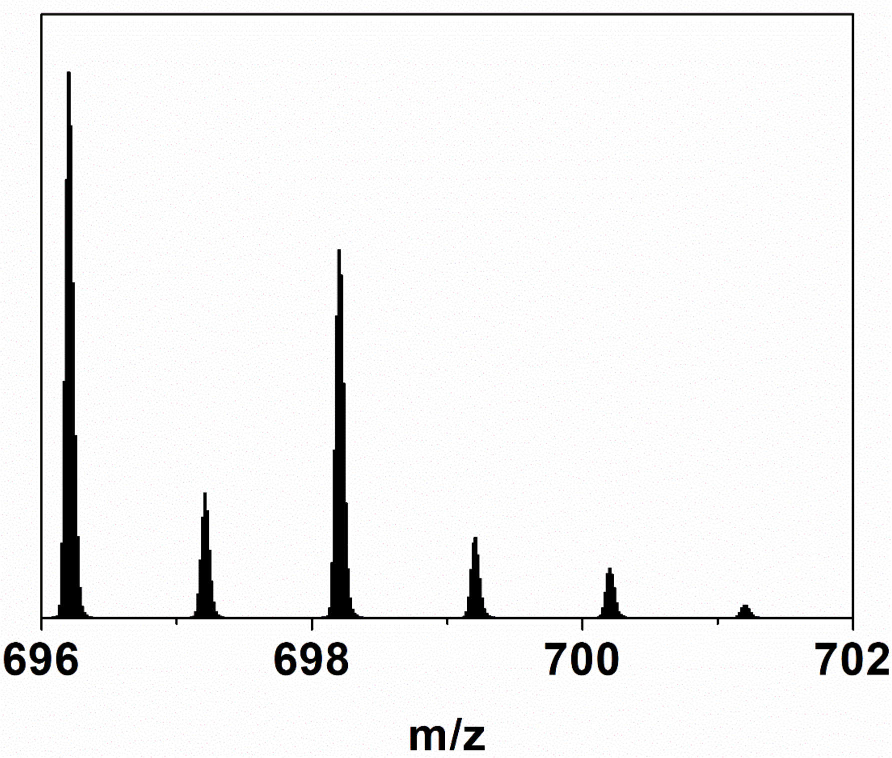

Figure S7. Cold injection ESI-MS of a frozen solution of **2** + 2 eq. KO_2 + 4 eq. 18-C-6. Observed: 696.2003

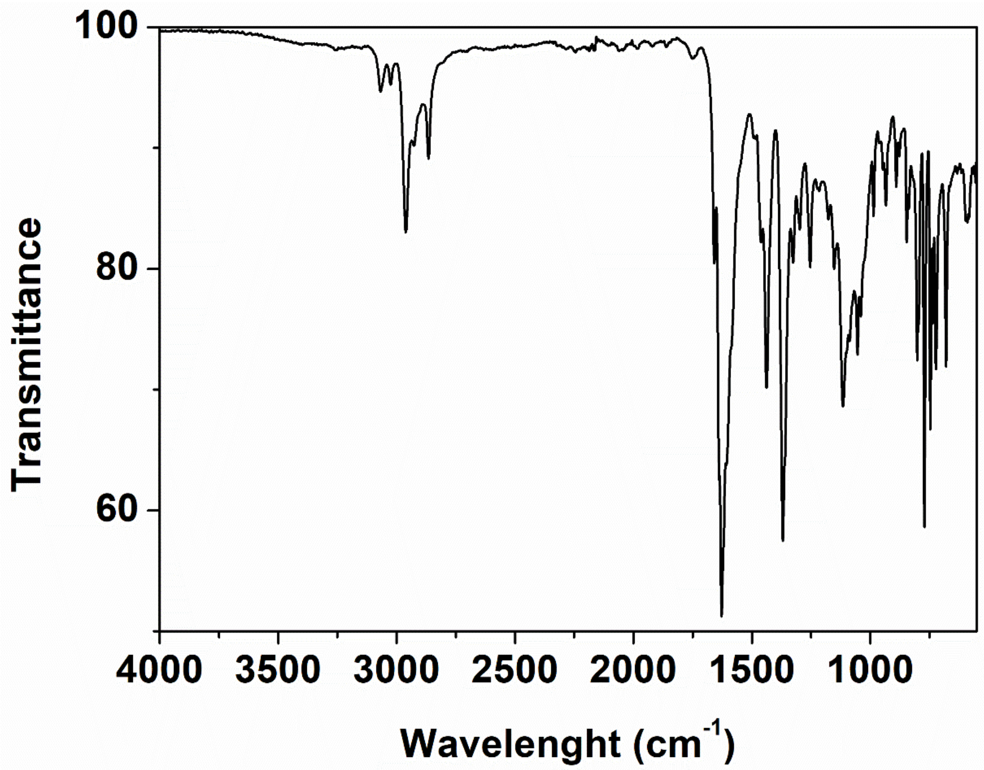

Figure S8. ATR-FTIR spectrum of **5**

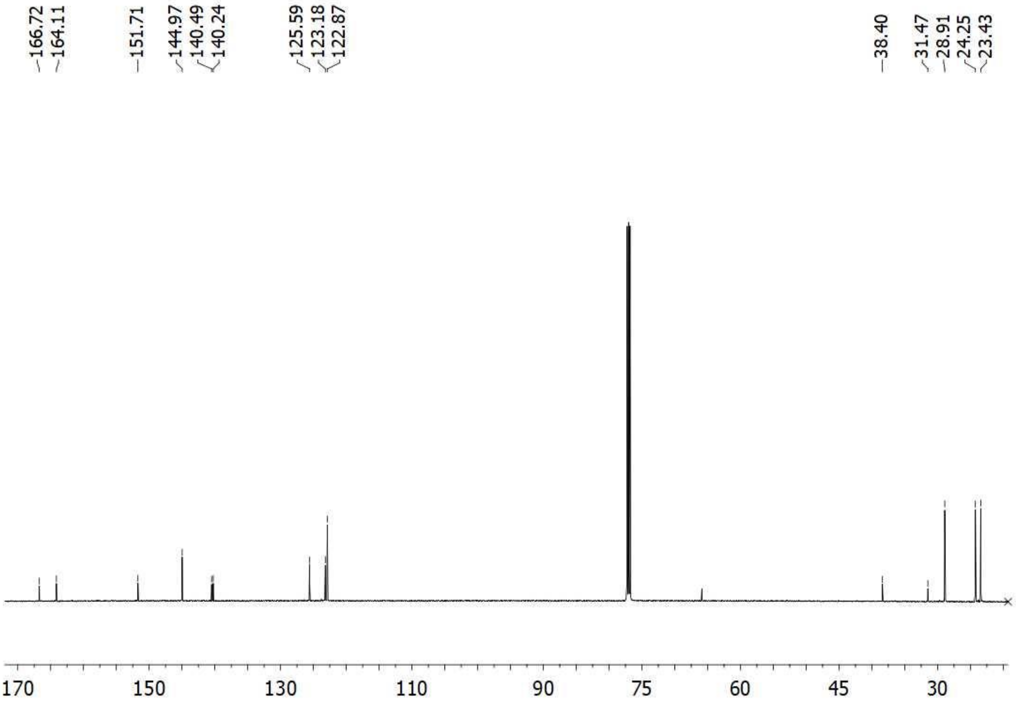

Figure S9. ^{13}C NMR spectrum of **5**. Unlabelled peaks correspond to residual solvent ($CHCl_3$ and Et_2O)

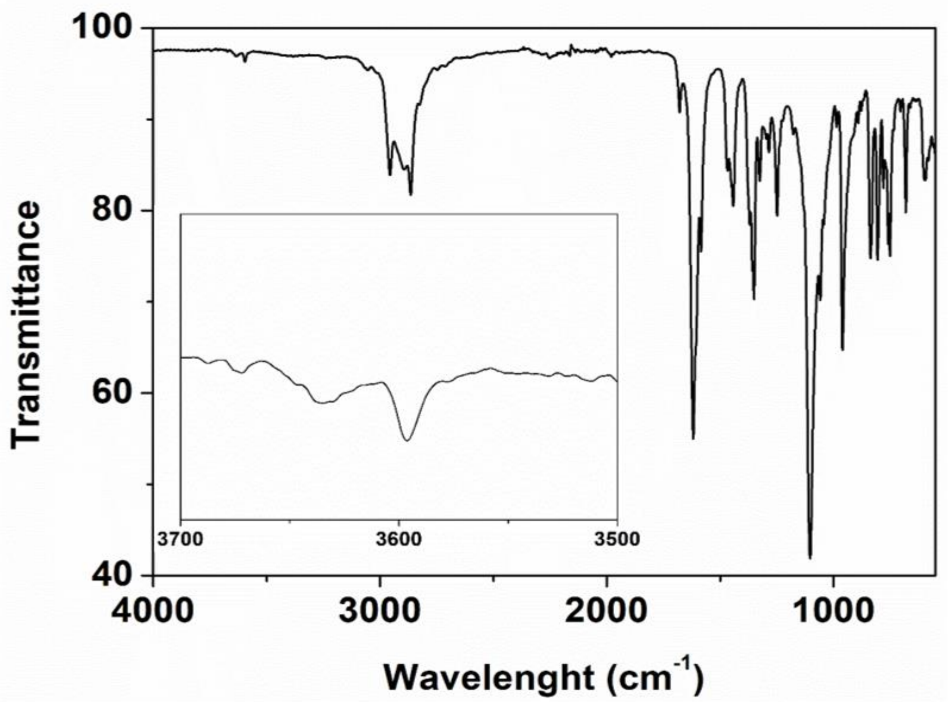

Figure S10. ATR-FTIR spectrum of **7a**

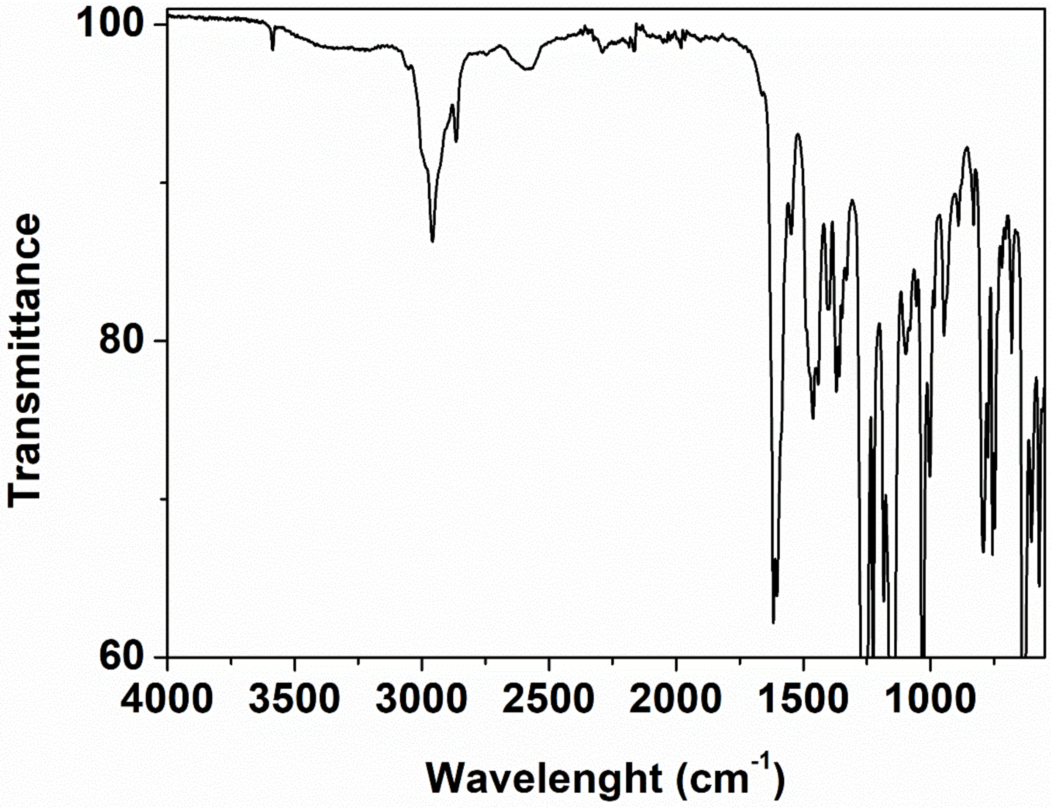

Figure S11. ATR-FTIR spectrum of **7b**

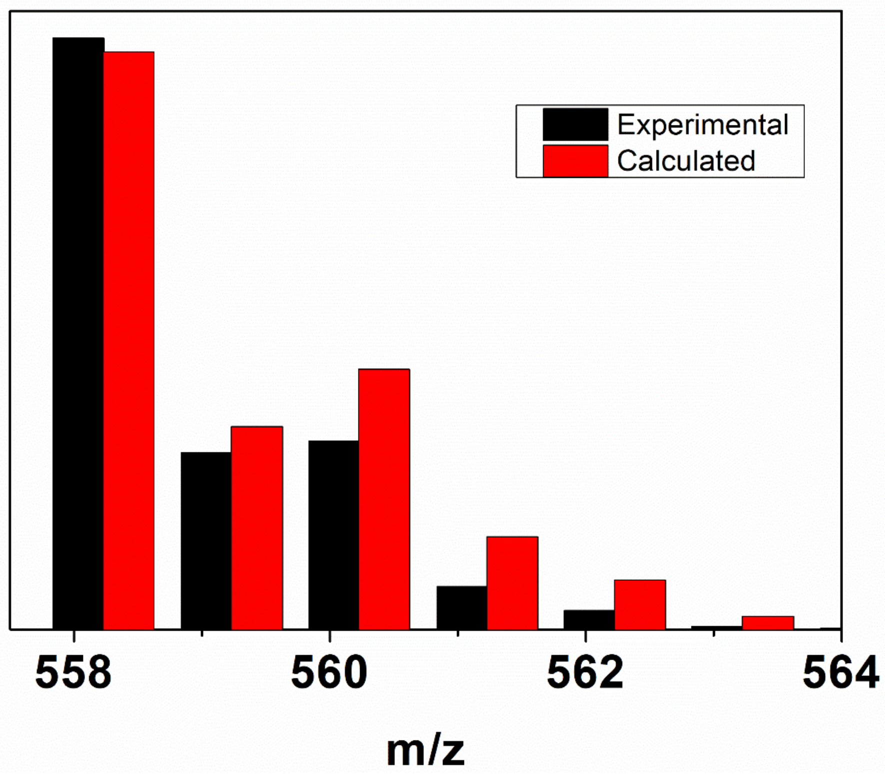

Figure S12. ESI-MS spectrum of **7a**. Observed: 558.2356. Calculated: 558.2267 $[Ni^{II}(PyN_2^{iPr2})(OH)]^-$.

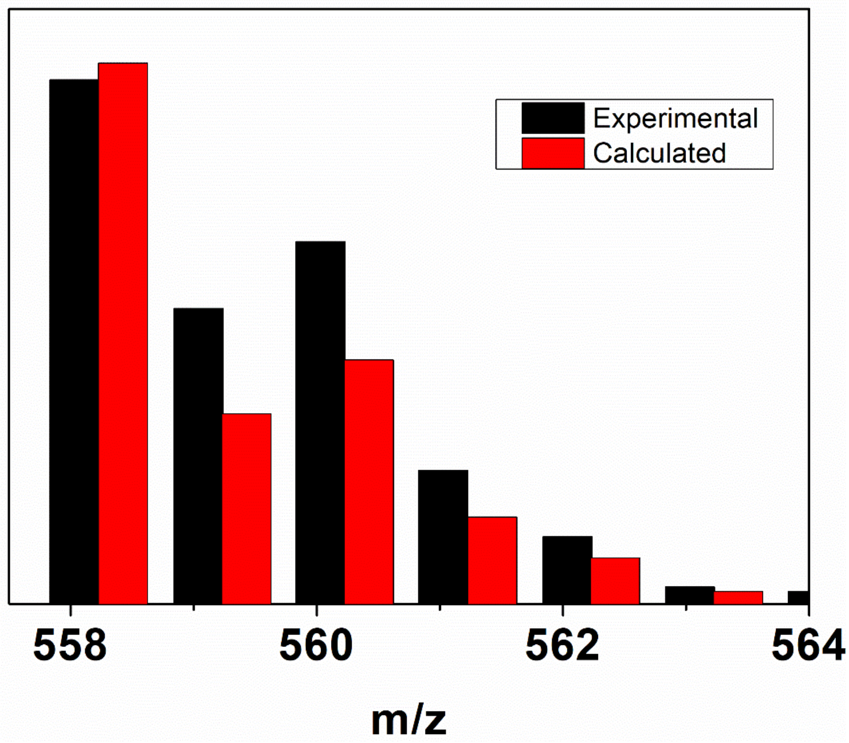

Figure S13. ESI-MS spectrum of **7b**. Observed: 558.2326. Calculated: 558.2267 $[Ni^{II}(PyN_2^{iPr2})(OH)]^-$.

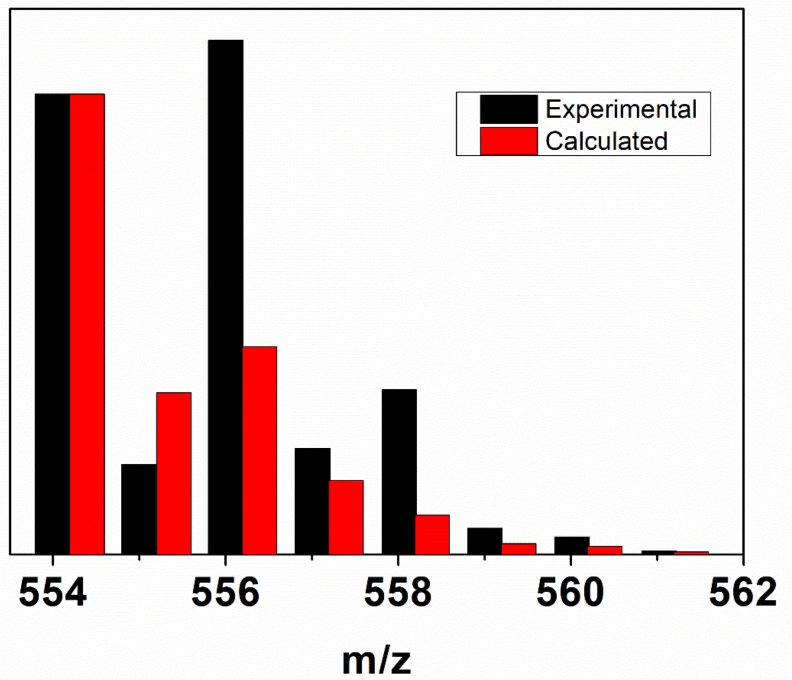

Figure S14. Negative mode cold injection ESI-MS of the reaction mixture **2** + KO_2. Observed: 554.1970. Calculated: 554.1954 $[H_2PyN_2^{iPr, EtCHO} – H]^-$. Overlapping mass peak at 556 distorts the isotopic pattern.

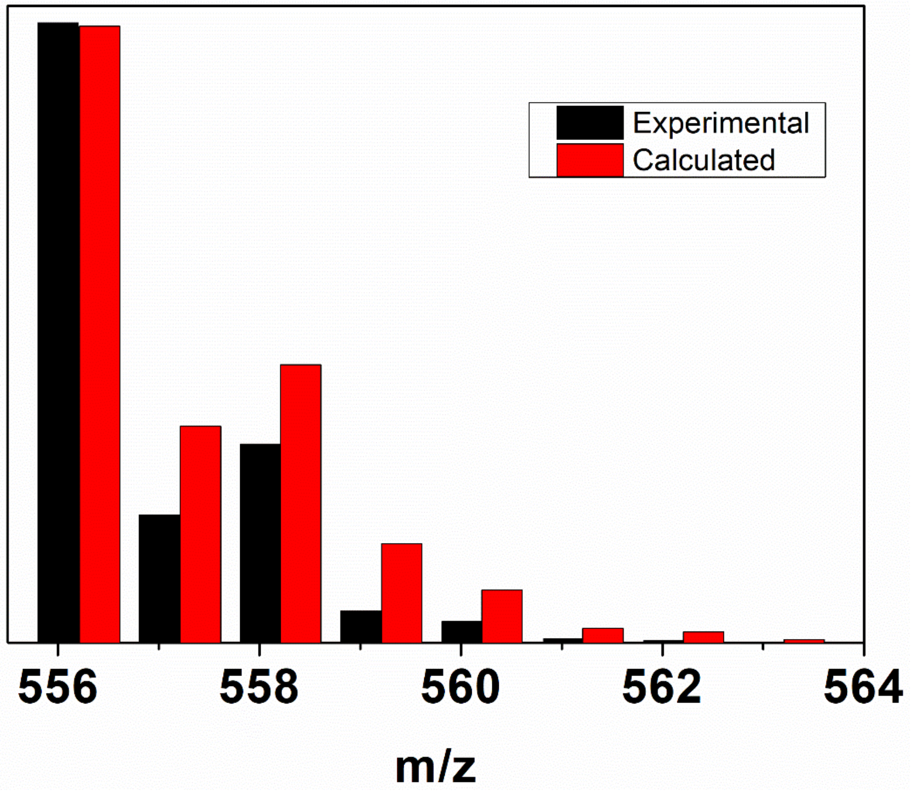

Figure S15. Negative mode cold injection ESI-MS of the reaction mixture **2** + KO_2. Observed: 556.1976. Calculated: 556.2110 $[Ni^{II}(PyN_2^{iPr,iPrO})]^-$

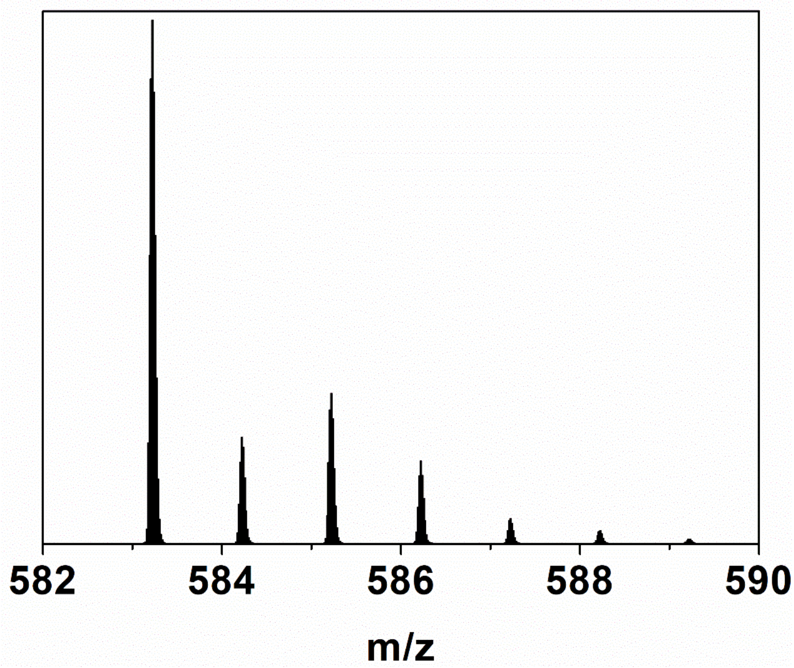

Figure S16. Cold-injection ESI-MS of the post-reaction mixture of **2** + 2 eq. KO_2 + 4 eq. 18-C-6 after 5 minutes showing the mass peak at m/z = 583.2172

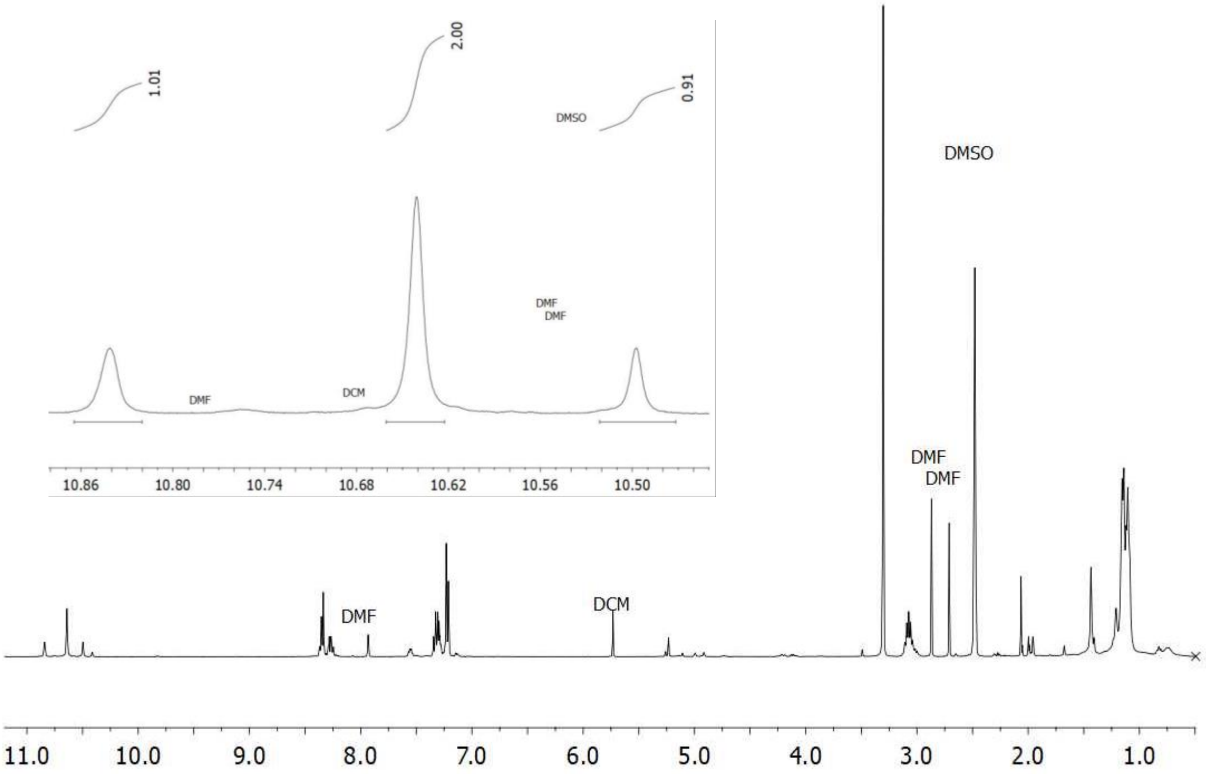

Figure S17. ^{1}H NMR spectrum of the acidified post-reaction mixture for the reaction of **2** + 2 eq. KO_2 + 4 eq. 18-C-6. Inset: the approximate 2:1 ratio of NH peaks of **1** to those of **10a** in DMSO-D_6.

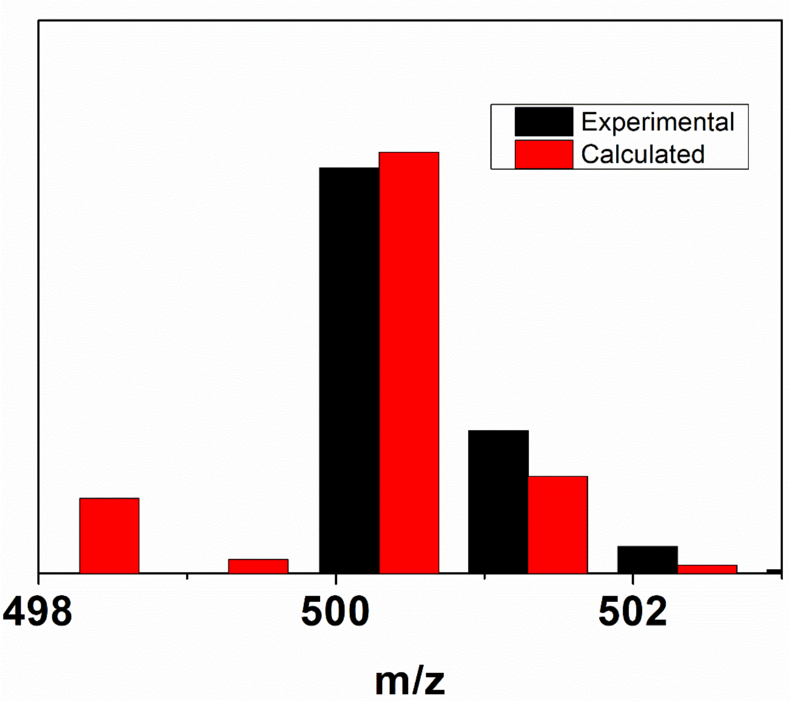

Figure S18. Negative mode ESI-MS of **10a**. Observed: 500.2865. Calculated: 500.2913 $[H_2PyN_2^{iPr,\ iPrOH} - H]^-$

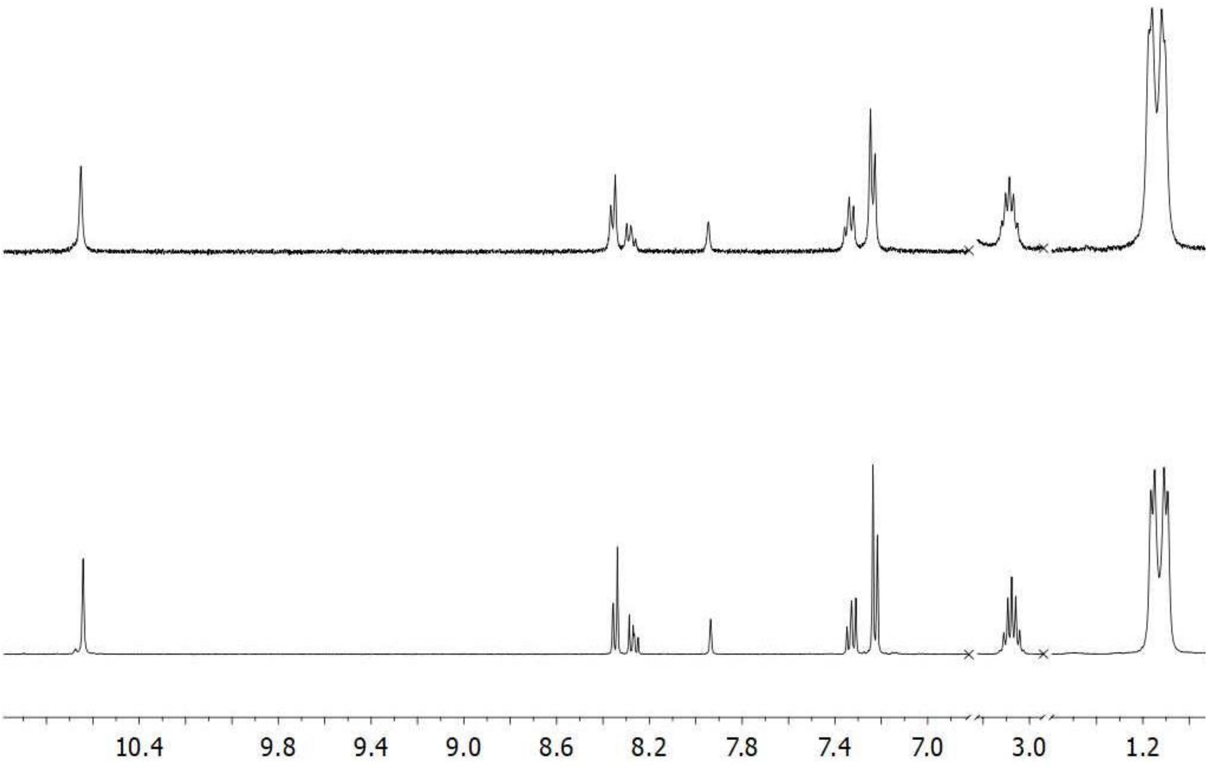

Figure S19. Post reaction acidified workup of the reaction of **1** (top) and **7b** (bottom) + 2 eq. KO_2 + 4 eq. 18-C-6 showing the presence of only **1**. Peak present at 7.89 ppm is DMF.

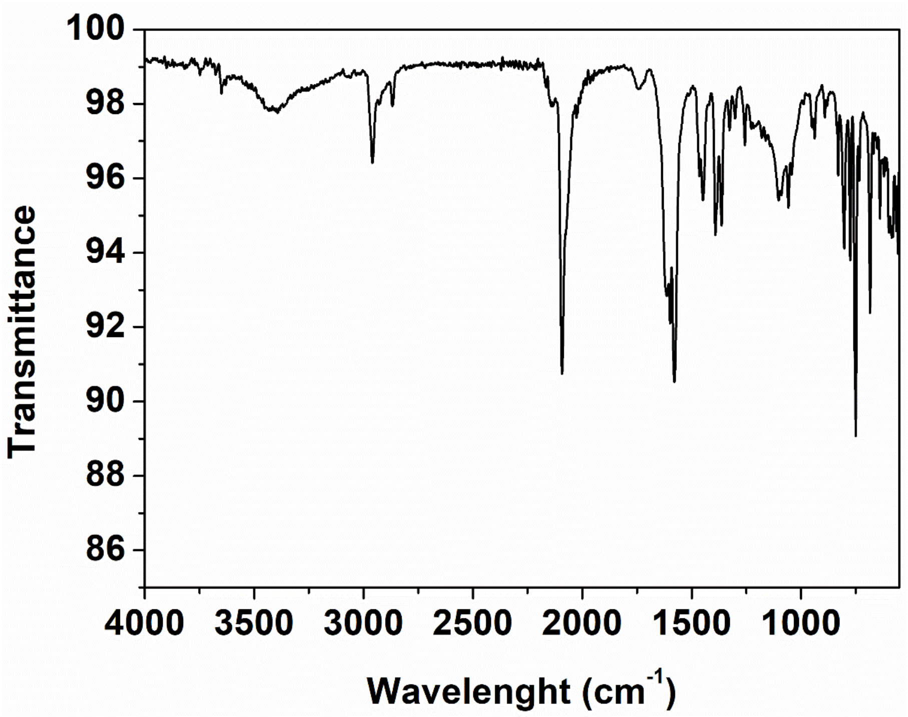

Figure S20. ATR-FTIR spectrum of **11**

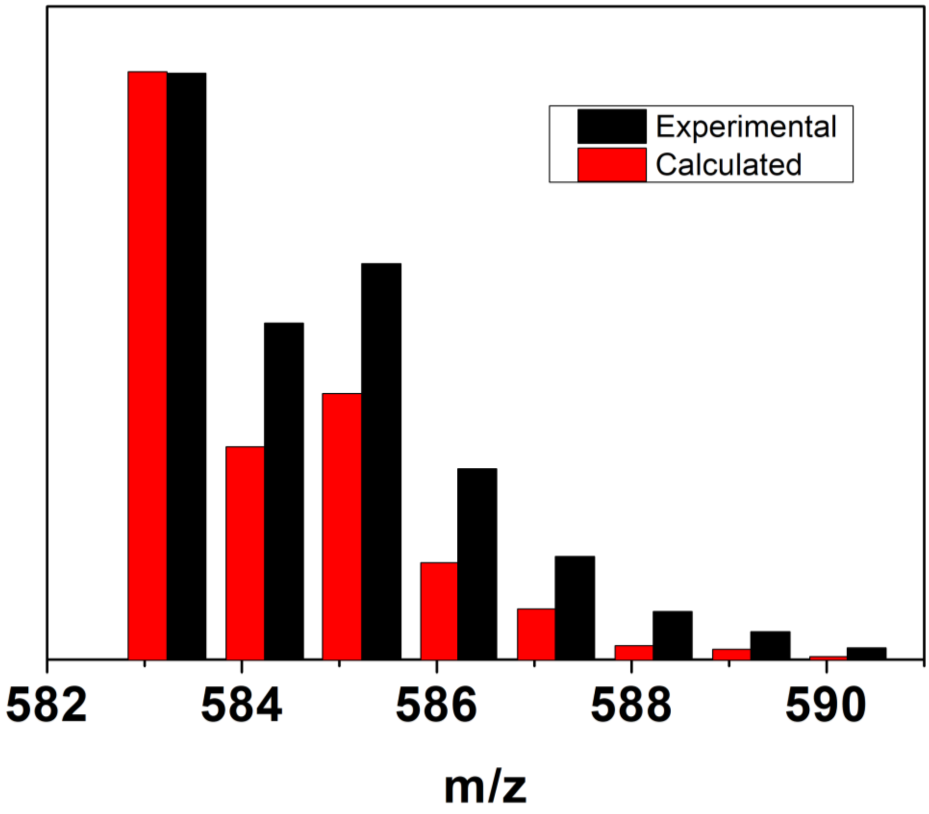

Figure S21. Negative mode ESI-MS of **11**. Observed: 583.2305. Calculated: 583.2331 [Ni^{II}(PyN$_2$^{iP2})(N$_3$)]$^-$.

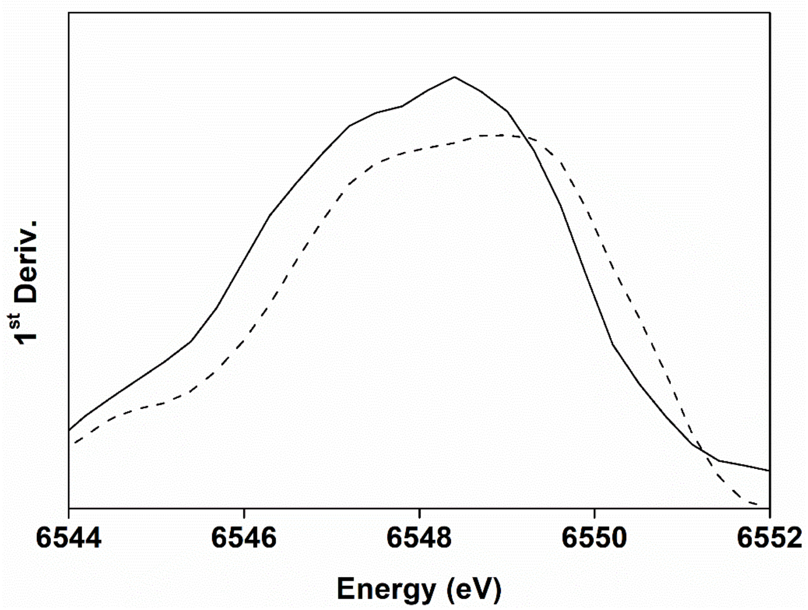

Figure S22. 1st derivative spectrum of the edge region for **12a** (solid trace) and **12b** (dashed trace) showing the change in the energy of the first inflection point (edge energy).

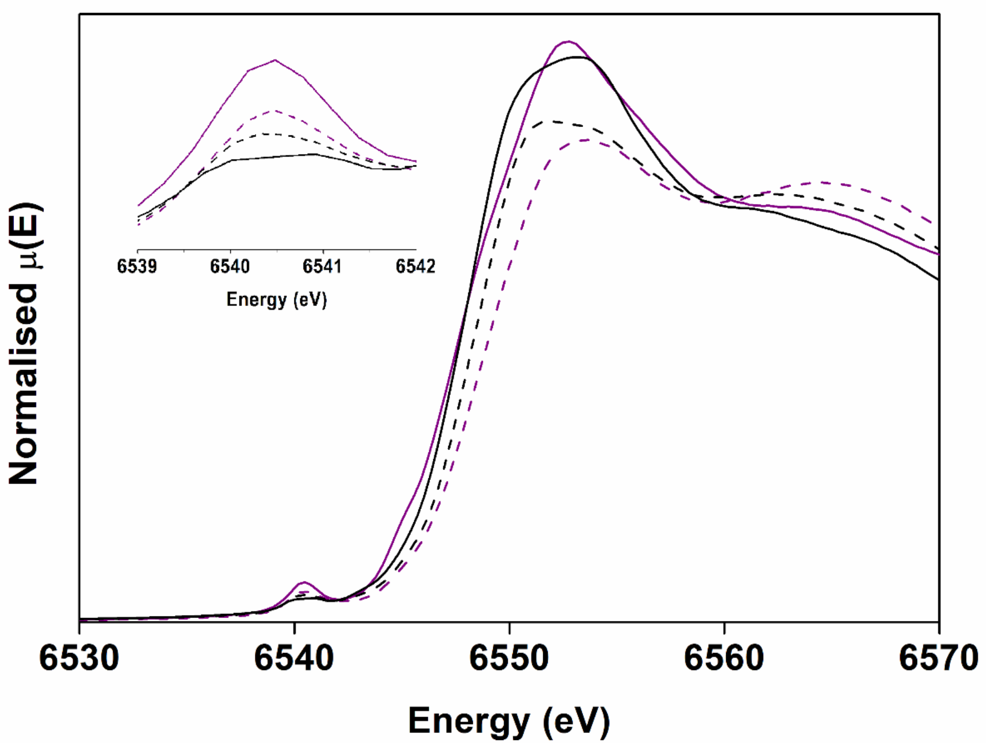

Figure S23. Normalised XANES spectra of **12a** (solid black trace), **12b** (dashed black trace), **13a** (solid purple trace)[125] and **13b** (dashed purple trace).[125] The inset shows an expansion of the pre-edge region.

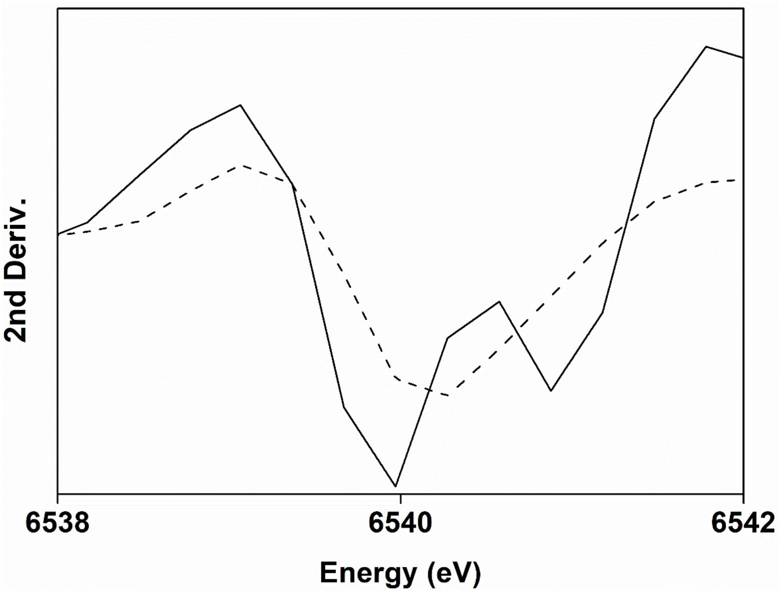

Figure S24. 2nd derivative spectrum of **12a** (solid trace) and **12b** (dashed trace) showing the asymmetry present in the 1s → 3d transitions of **12a**.

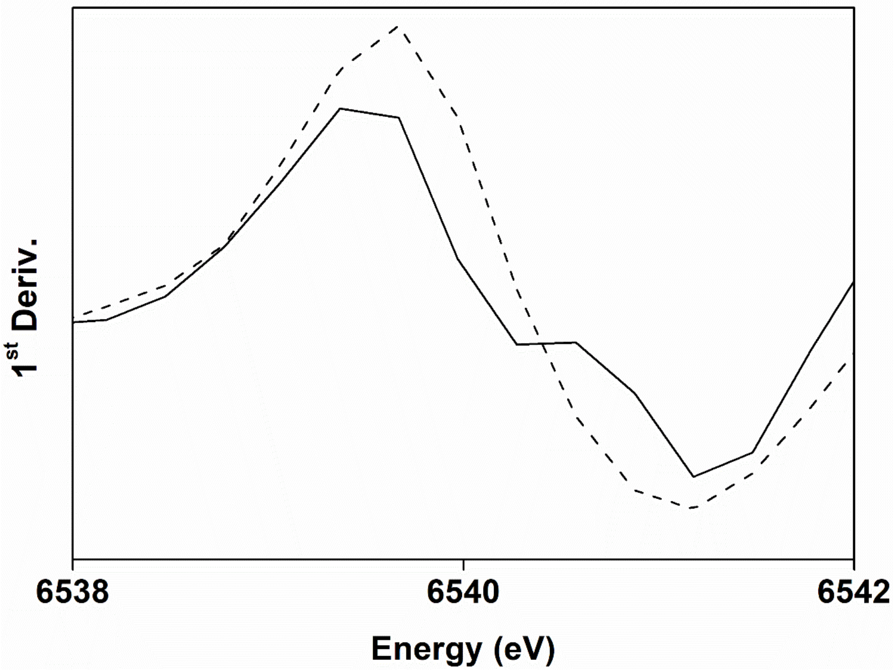

Figure S25. 1st derivative spectrum of the pre-edge of **12a** (solid trace) and **12b** (dashed trace).

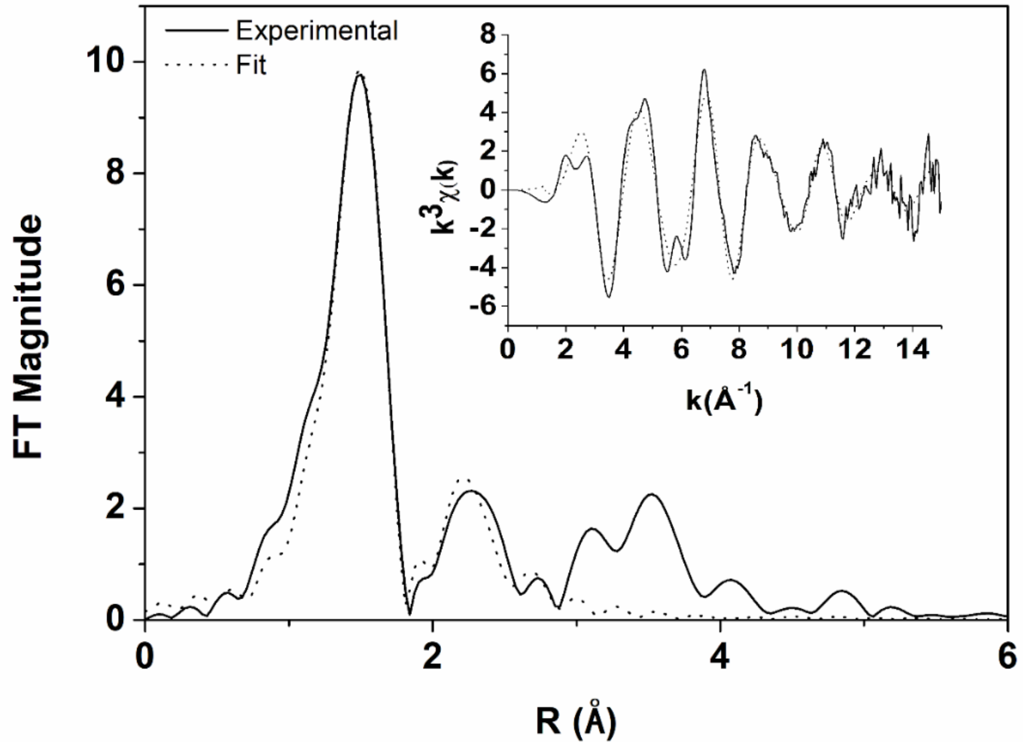

Figure S26. Representative best fits (Fit 15 in Table S2) to k^3-weighted EXAFS data of **13a**. Experimental data is shown as a black trace, while the best fit is represented as a dotted trace.

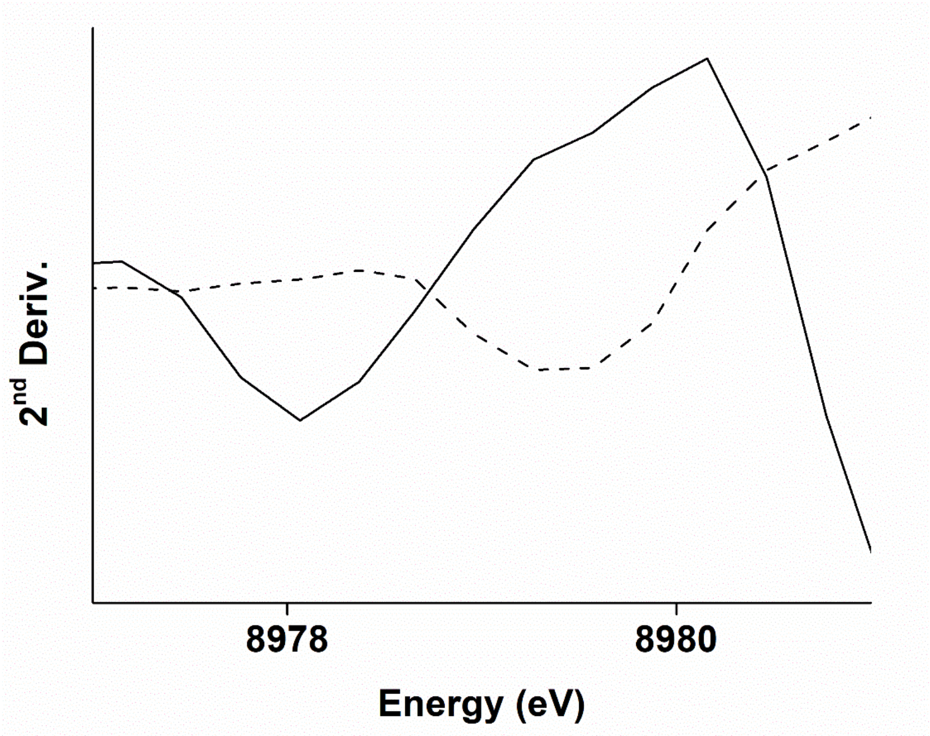

Figure 27. 2nd derivative spectrum of the pre-edge (1s → 3d transition) of **14a** (black trace) and **14b** (dashed trace) showing the shift in the pre-edge energy.

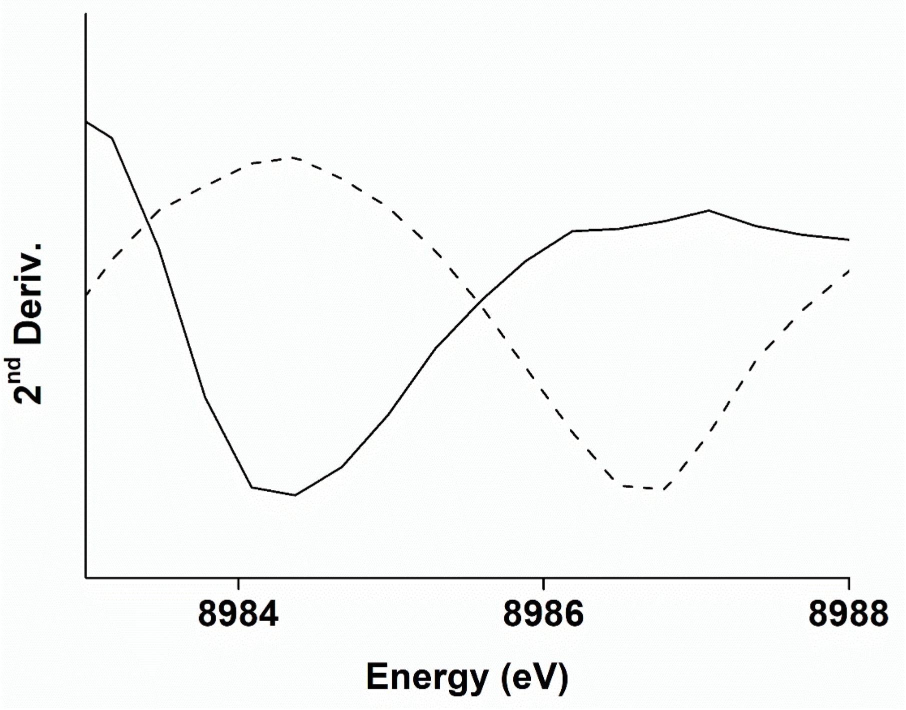

Figure S28. 2nd derivative spectrum of the 1s → 4p + shakedown transition of **14a** (black trace) and **14b** (dashed trace).

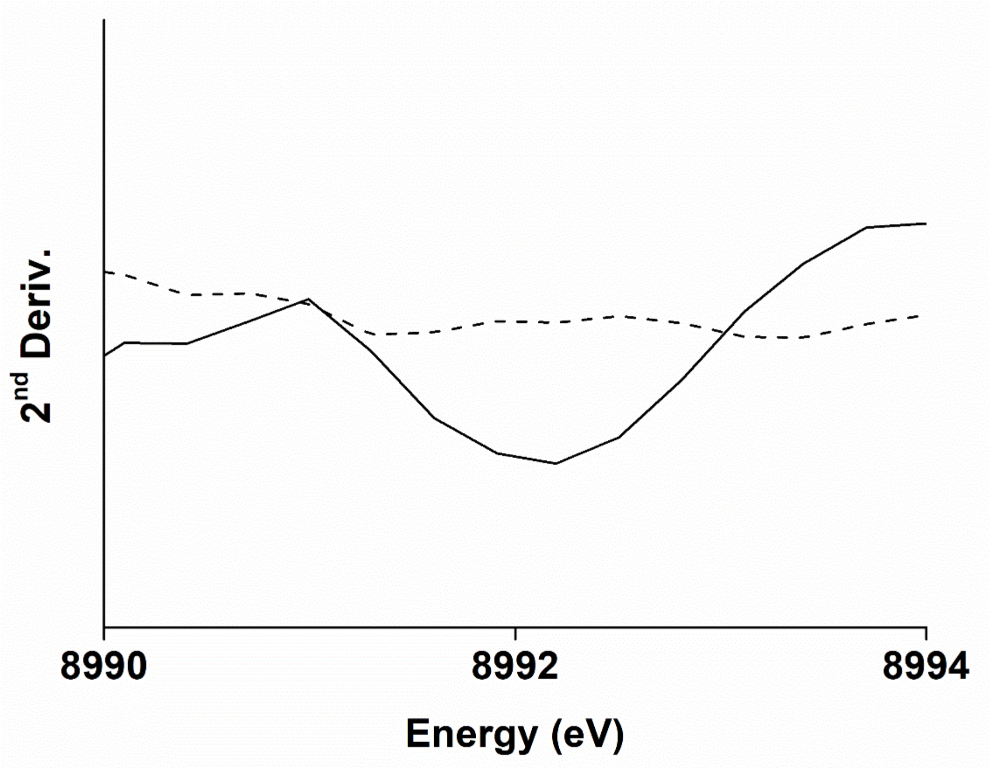

Figure S29. 2^{nd} derivative spectrum of the 1s→ 4p main transition of **14a** (black trace) and the absence of this transition in **14b** (dashed trace).

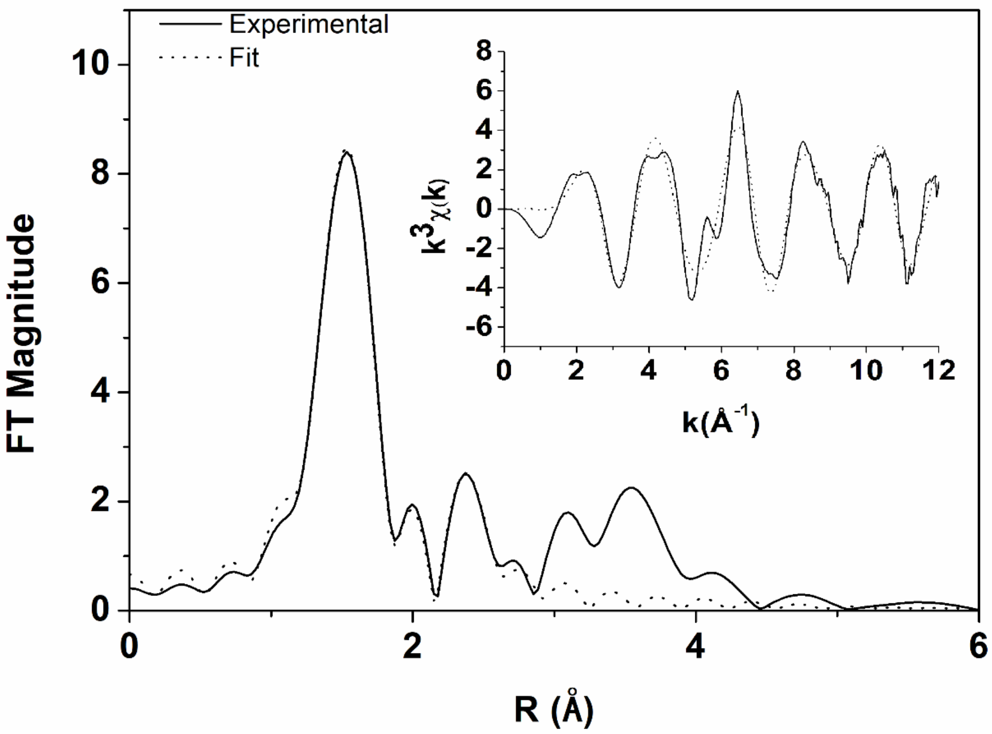

Figure S30. Representative best fits (Fit 8 in Table S4) to k^3-weighted EXAFS data of **14a**. Experimental data is shown as a black trace, while the best fit is represented as a dotted trace.

Table S1. Major bond angles and parameters in **5**

	Unit 1	Unit 2
Atoms	Angle (°)	Angle (°)
O-Ni-N_{am}	100.81(5)	101.36(5)
N_{am}-Ni-N_{py}	82.83(6)	83.08(5)
N_{py}-Ni-N_{am}	83.25(6)	83.48(6)
N_{am}-Ni-O	93.11(5)	92.15(5)
O-Ni-N_{py}	175.46(5)	171.85(6)
N_{am}-Ni-N_{am}	166.07(6)	166.49(6)
Plane	Angle (°)	Angle (°)
DMF vs PyN_2^{iPr2}	36.52	32.79
Phenyl (1) vs PyN_2^{iPr2}	89.02	83.09
Phenyl (2) vs PyN_2^{iPr2}	75.54	74.70

Table S2. Selected EXAFS fits if **13a**[a]

	Mn-N/O			Mn-N/O			Mn-N/O			Mn-C			Mn-C			Mn-Mn					
fit	N	r	σ^2	N	r	σ^2	N	r	σ^2	N	r	σ^2	N	r	σ^2	N	r	σ^2	ΔE_0	χ^2	R
1	4	2.09	2.94																0.26	45.89	0.060
2	5	2.10	4.34																-0.67	55.17	0.072
3	6	2.09	5.69																-1.53	79.70	0.104
4	4	2.07	4.76				1	2.43	-1.27										0.08	12.28	0.010
5	4	2.09	4.64				2	2.44	3.05										1.86	8.34	0.007
6	**2**	**2.03**	**2.75**	**2**	**2.13**	**1.35**	**1**	**2.43**	**0.04**										**-0.66**	**13.66**	**0.005**
7	4	2.08	4.44				2	2.44	3.67	2	3.00	1.86							1.55	51.06	0.113
8	4	2.09	4.27				2	2.44	4.88	2	3.01	0.57	3	3.22	5.28				3.33	50.90	0.092
9	4	2.09	4.38				2	2.45	4.92	2	2.99	-1.47	3	3.16	3.61	1	3.62	1.87	2.78	18.94	0.027
10	4	2.09	4.39				2	2.44	4.80	3	3.00	0.68	3	3.19	2.60	1	3.62	2.11	2.75	21.77	0.030
11	2	2.02	2.53	2	2.13	0.02	1	2.42	2.22	2	3.01	0.88							-0.88	12.53	0.005
12	2	2.04	2.88	2	2.14	1.20	1	2.43	1.99	2	2.99	-0.02	3	3.19	5.64				0.94	13.84	0.009
13	2	2.04	2.66	2	2.14	0.89	1	2.43	2.05	3	3.01	1.98	3	3.21	3.79				0.97	14.46	0.010
14	2	2.04	1.68	2	2.15	0.35	1	2.42	1.33	3	3.01	2.92	3	3.21	5.57	1	3.61	2.83	1.60	28.47	0.028
15	**2**	**2.04**	**2.05**	**2**	**2.15**	**0.95**	**1**	**2.43**	**1.35**	**2**	**2.99**	**0.15**	**3**	**3.18**	**5.98**	**1**	**3.61**	**2.41**	**1.56**	**26.93**	**0.027**

[a]Fitting range was *k* = 2 - 14.0 Å^{-1} with back transform ranges of 1 - 1.2.25 Å for fits 1 - 4 and 1 - 3.60 Å for fits 7 - 15. r is in units of Å; σ² is in units of 10^{-3} Å

Table S3. Selected EXAFS fits of **13b**[a]

	Mn-N/O			Mn-N/O			Mn-N/O			Mn-C			Mn-C			Mn-Mn					
fit	N	r	σ^2	N	r	σ^2	N	r	σ^2	N	r	σ^2	N	r	σ^2	N	r	σ^2	ΔE_0	χ^2	R
1	4	1.89	11.80																-5.414	167.8	0.063
2	5	1.89	14.60																-5.862	214.3	0.081
3	6	1.89	17.15																-6.380	274.6	0.104
4	3	1.91	6.18	1	2.13	0.12													0.485	327.5	0.014
5	2	1.87	1.48	3	2.05	7.23													-0.512	315.4	0.149
6	2	1.87	3.31	4	2.04	13.13													-1.375	368.9	0.175
7	3	1.85	8.18				2	2.43	4.51										-11.27	239.6	0.114
8	**2**	**1.90**	**1.43**	**2**	**2.12**	**1.36**	**1**	**2.40**	**4.02**										**3.752**	**310.1**	**0.056**
9	2	1.90	1.60	2	2.13	1.64	1	2.41	3.92	2	3.05	9.87							4.349	121.2	0.038
10	2	1.90	1.65	2	2.13	1.77	1	2.42	4.19	3	3.06	12.82							4.400	87.38	0.027
11	2	1.91	0.66	2	2.14	-0.05	1	2.40	0.03	2	3.01	-0.19	2	3.21	-0.36				5.86	39.24	0.022
12	2	1.91	0.07	2	2.13	-0.04	1	2.39	0.09	2	2.99	-1.55	3	3.19	0.03				5.62	43.97	0.025
13	2	1.90	1.52	2	2.12	1.67	1	2.41	4.03	2	3.04	9.20				1	3.58	5.51	4.04	50.75	0.029
14	2	1.91	0.93	2	2.13	0.16	1	2.40	1.82	2	3.00	-0.07	2	3.19	-0.77	1	3.60	9.07	5.317	6.40	0.002
15	**2**	**1.91**	**1.05**	**2**	**2.13**	**0.41**	**1**	**2.40**	**3.02**	**2**	**2.98**	**1.10**	**3**	**3.18**	**3.97**	**1**	**3.59**	**8.42**	**5.15**	**4.17**	**0.001**

[a]Fitting range was *k* = 2 – 11.0 Å^{-1} with back transform ranges of 1 - 1.96 Å for fits 1 – 6, 1-2.48 Å for fits 7 – 8 and 1 – 3.70 Å for fits 9 - 15. r is in units of Å; σ² is in units of 10^{-3} Å.

Table S4. Selected EXAFS fits of **14a**[a]

	Cu-N/O			Cu-N/O			Cu···C/O					
fit	n	r	σ^2	n	r	σ^2	n	r	σ^2	ΔE_0	χ^2	R
1	3	1.94	2.03							2.10	140.35	0.0200
2	4	1.96	2.46							1.56	62.35	0.0089
3	*5*	*1.96*	*3.97*							*1.09*	*45.83*	*0.0065*
4	4	1.96	3.82							0.88	108.8	0.0399
5	4	1.96	2.30	2	2.52	6.78				-0.14	152.3	0.0397
6	4	1.96	2.44	2	2.52	11.25	4	2.85	4.8	1.132	47.18	0.00728
7	4	1.96	2.36	1	2.52	0.41				0.847	120.20	0.0313
8	**4**	**1.96**	**2.44**	**1**	**2.51**	**4.56**	**4**	**2.85**	**6.16**	**1.63**	**49.53**	**0.0076**
9	5	1.96	3.82							0.88	108.8	0.0399
10	5	1.96	3.79	2						-0.47	159.1	0.0414
11	5	1.96	3.94	2	2.56	5.78	4	2.84	5.50	0.69	78.66	0.0121
12	5	1.98	3.38	1	2.53	-.56				0.40	117.72	0.0306
13	5	1.96	3.99	1	2,55	-.32	4	2.84	7.84	1.14	65.33	0.0101

[a]Fitting range was k = 2-12.0 Å^{-1} with back transform ranges of 1 - 1.872 Å for fits 1 - 3 and 1 - 2.884 Å for 4 - 13, r is in units of Å; σ^2 is in units of 10^{-3} Å; ΔE_0 is in units of eV; R represents the fractional mis-fit of the data, while χ^2 is the χ^2 fitting metric normalized by the number of independent data points in a given fit.

Table S5. Selected EXAFS fits of **14b**[a]

	Cu-N/O			Cu···C			Cu···C					
fit	N	r	σ^2	n	r	σ^2	n	r	σ^2	ΔE_0	χ^2	R
1	4	1.88	5.01							6.091	20.03	0.0048
2	5	1.90	5.12							5.659	23.40	0.0057
3	6	1.89	6.40							5.117	44.19	0.0107
4	3	1.86	2.57	2	1.96	1.92				5.911	45.47	0.0043
5	4	1.88	5.13							5.846	107.29	0.0665
6	4	1.88	5.07				4	2.76	4.91	6.671	36.51	0.0177
7	**4**	**1.88**	**5.08**	**1**	**2.38**	**5.63**	**4**	**2.76**	**5.19**	**6.370**	**25.79**	**0.0089**
8	4	1.88	5.07	2	2.40	12.05	4	2.75	5.11	5.93	24.95	0.0087
9	5	1.90	5.20							5.67	73.00	0.0453
10	5	1.90	3.92				4	2.77	6.15	6.989	85.55	0.0041
11	5	1.90	5.27	1	2.40	5.37	4	2.76	7.41	5.902	48.35	0.0169
12	5	1.89	5.25	2	2.41	9.17	4	2.75	7.24	5.384	33.95	0.0118

[a] Fitting range was $k = 2 - 14.0$ Å^{-1} with back transform ranges of 1 - 1.867 Å for fits 1 - 4 and 1 - 2.616 Å for fits 5 - 12. r is in units of Å; σ^2 is in units of 10^{-3} Å; ΔE_0 is in units of eV; R represents the fractional mis-fit of the data, while χ^2 is the χ^2 fitting metric normalized by the number of independent data points in a given fit.

Table **S6**. Crystal data and structure refinement for compounds

Empirical formula	**3**	**5**	**7a**	**11**
Formula weight	1483.57	1305.00	3288.99	826.65
Temperature	100(2) K	100(2) K	100(2) K	100(2) K
Wavelength	1.54178 Å	0.71073 Å	0.71073 Å	0.71073 Å
Crystal system	Triclinic	Monoclinic	Triclinic	Monoclinic
Space group	P 1	P 21/c	P 1	P 21/c
Unit cell	$\bar{1}$ a = 10.8440(5) Å	a = 20.9080(6) Å	a = 16.7581(5) Å	a = 15.2551(9) Å
	b = 13.6846(6) Å	b = 22.0164(7) Å	b = 16.9104(5) Å	b = 13.9905(8) Å
	c = 14.2990(6) Å	c = 16.2181(5) Å	c = 19.5538(6) Å	c = 21.0147(12) Å
	α = 109.102(3)°	α = 90°	α = 66.7710(12)°	α = 90°
	β = 102.778(3)°	β = 109.2353(9) °	β = 88.0402(13)°	β = 103.9860(10)°
	γ = 95.046(3)°	γ = 90°	γ = 68.5890(13)°	γ = 90°
Volume	1925.59(15) Å3	7048.7(4) Å3	4701.5(3) Å3	4352.1(4) Å3
Z	1	4	1	4
Density (calculated)	1.279 Mg/m3	1.230 Mg/m3	1.162 Mg/m3	1.262 Mg/m3
Absorption coefficient	4.481 mm^{-1}	0.591 mm^{-1}	0.548 mm^{-1}	0.507 mm^{-1}
F(000)	788	2792	1758	1760
Crystal size	0.12 x 0.11 x 0.05 mm3	0.261 x 0.240 x 0.107 mm3	0.309 x 0.192 x 0.122 mm3	0.484 x 0.228 x 0.106 mm3
Theta range for data collection	3.393 to 68.526°.	1.385 to 28.592°.	2.487 to 26.499°.	1.765 to 27.517°.
Index ranges	-13≤h≤13, -16≤k≤16, -17≤l≤17	-27<=h<=28, -29<=k<=29, -21<=l<=21	-20≤h≤21, -21≤k≤21, -24≤l≤24	-19<=h<=19, -18<=k<=13, -27<=l<=27
Reflections collected	26459	149554	210643	41602

Independent reflections	7053 [R(int) = 0.0500]	17915 [R(int) = 0.0511]	19407 [R(int) = 0.0466]	9988 [R(int) = 0.0364]
Completeness to theta	theta = 67.679° 99.90%	theta = 25.242° 100.0 %	theta = 67.679° 99.80%	theta = 25.242° 99.9 %
Absorption correction	Semi-empirical from equivalents	Semi-empirical from equivalents	Semi-empirical from equivalents	
Max. and min. transmission	0.7531 and 0.6511	0.7458 and 0.6871	0.7454 and 0.7093	
Refinement method	Full-matrix least-squares on F2	Full-matrix least-squares on F2	Full-matrix least-squares on F2	Full-matrix least-squares on F2
Data / restraints / parameters	7053 / 362 / 574	17915 / 12 / 872	19407 / 1074 / 1497	9988 / 61 / 610
Goodness-of-fit on F2	1.073	1.024	1.021	1.037
Final R indices [I>2σ(I)]	R1 = 0.0628, wR2 = 0.1756	R1 = 0.0385, wR2 = 0.0824	R1 = 0.0740, wR2 = 0.2121	R1 = 0.0386, wR2 = 0.0925
R indices (all data)	R1 = 0.0729, wR2 = 0.1856	R1 = 0.0617, wR2 = 0.0884	R1 = 0.0938, wR2 = 0.2424	R1 = 0.0632, wR2 = 0.0994
Largest diff. peak and hole	1.654 and -0.424 e.Å-3	0.416 and -0.376 e.Å-3	1.221 and -0.862 e.Å-3	0.421 and -0.430 e.Å-3